



# Politecnico di Bari

Repository Istituzionale dei Prodotti della Ricerca del Politecnico di Bari

Mechanics of functional materials for soft robotics

This is a PhD Thesis

*Original Citation:*

Mechanics of functional materials for soft robotics / Caruso, Fabio. - ELETTRONICO. - (2024).  
[10.60576/poliba/iris/caruso-fabio\_phd2024]

*Availability:*

This version is available at <http://hdl.handle.net/11589/267801> since: 2024-03-28

*Published version*

DOI:10.60576/poliba/iris/caruso-fabio\_phd2024

Publisher: Politecnico di Bari

*Terms of use:*

(Article begins on next page)

10 May 2024



Politecnico  
di Bari

DEPARTMENT OF MECHANICS, MATHEMATICS AND  
MANAGEMENT

MECHANICAL AND MANAGEMENT ENGINEERING  
PH.D. PROGRAM

SSD: ING-IND/13 - APPLIED MECHANICS

Final dissertation

---

# Mechanics of functional materials for soft robotics

---

by  
FABIO CARUSO

Supervisors:

Prof. Giacomo MANTRIOTA

Prof. Giulio REINA

Prof. Vito CACUCCIOLO

Coordinator of the Ph.D. Program:  
Prof. Giuseppe P. DEMELIO

---

*Course XXXVI, 01/11/2020 - 31/01/2024*

## Abstract

Soft robotics is an emerging field that explores the development of robotic structures made of flexible and stretchable materials. The need to build robots with soft materials derives from the limitations of traditional robots in applications in which safety, compliance, and adaptation to unstructured environments are crucial requirements.

Although softness allows for dexterity and safety, stiffening is required to exert high forces when necessary. Therefore, developing a robotic system in which the stiffness can be controlled and varied on demand is essential in several applications and represents a significant challenge for the field. Among the various strategies explored by researchers, layer jamming systems represent a promising solution. These systems are composed of flexible layers that transition from a rigid to a soft state when external forces such as shear or compression act on them.

Despite the increasing interest, the underlying mechanics that govern the behavior of these systems is not fully understood. The existing analytical models are not able to describe their behavior beyond the initial deformation phase.

The first part of the thesis aimed to fill this gap by describing the intrinsic mechanics that govern the behavior of layer jamming structures. To achieve this, an analytical model is presented for the first time to predict how the change in bending stiffness is related to the slip between layers. The model is able to capture the non-linear behavior, beyond the initial elastic deformation phase, with a piecewise linear approximation between subsequent slips. In particular, the model predicts that slip starts at the innermost interface and then progressively propagates toward the outer interfaces resulting in a gradual decrease in stiffness. The predictions of the model were then validated with experiments and finite element simulations, showing that the model is able to predict with great accuracy the effect of the main design parameters, including the number of layers, vacuum pressure and coefficient of friction as well as the energy dissipated by friction during a load-unload cycle. The outcomes of the model not only represent a significant step forward in understanding the complex intrinsic mechanics of these structures but could help researchers to design more advanced variable stiffness applications in soft robotics.

With the aim of integrating these systems into a useful real-world application, the second part of the thesis investigates the role of stiffness in zipping performance of electroadhesion-based soft grippers. Zipping refers to the physical phenomenon in which gripper's soft fingers spontaneously conform to the shape of the objects when a sufficiently high voltage is applied. An analytical model has been developed to describe this behavior. The model describes how the ability to conform to the objects

is influenced by the interplay between electrical and mechanical aspects. A set of experiments on objects with different materials and geometries have been performed to validate the model outcomes. It has been discovered that the phenomenon is governed by two voltage thresholds: a first one below which no zipping occurs and a second one above which the soft fingers fully collapse on the objects. Between the two values, the wrapping angle increases with the applied voltage. Model results are in good agreement with experiments, even if some observed phenomena related to charge accumulation, that are neglected in the model, seem to have a great influence on the experiments.





# Contents

<b>Abstract</b>	<b>ii</b>
<b>List of Figures</b>	<b>vii</b>
<b>List of Tables</b>	<b>ix</b>
<b>1 Introduction</b>	<b>1</b>
1.1 Background and motivation . . . . .	2
1.2 Thesis outline . . . . .	4
<b>2 Variable stiffness structures</b>	<b>7</b>
2.1 Variable stiffness structures in nature . . . . .	7
2.2 Variable stiffness structures in hard robotics . . . . .	10
2.3 Variable stiffness structures in soft robotics . . . . .	12
2.3.1 Jamming systems . . . . .	16
<b>3 Electroadhesion soft gripper</b>	<b>21</b>
3.1 Electroadhesion working principle . . . . .	22
3.2 Active wrapping . . . . .	23
3.3 Passive wrapping . . . . .	27
3.4 Peeling in electroadhesion soft grippers . . . . .	28
3.5 Layer jamming in electroadhesion soft grippers . . . . .	31
<b>4 Layer jamming: Modeling and experimental validation</b>	<b>33</b>
4.1 Introduction . . . . .	34
4.2 Analytical formulation . . . . .	36
4.2.1 Four Layers . . . . .	38
4.2.2 Arbitrary number of layers . . . . .	41
4.2.3 Model refinement including the effect of the overhangs . . . . .	44
4.2.4 Cantilever configuration . . . . .	46
4.3 Materials and methods . . . . .	48

## CONTENTS

4.3.1	Finite element model for small deflections . . . . .	48
4.3.2	Effect of the number of layers . . . . .	49
4.3.3	Effect of the vacuum pressure . . . . .	50
4.3.4	Effect of the coefficient of friction . . . . .	52
4.3.5	Finite element model for large deflection . . . . .	53
4.3.6	Experimental set-up . . . . .	54
4.3.7	Fabrication process . . . . .	55
4.4	Results . . . . .	56
4.4.1	Influence of the main design parameters . . . . .	56
4.4.2	Influence of the overhangs on the bending stiffness of the structure	58
4.4.3	Design optimization . . . . .	61
4.5	Conclusions . . . . .	63
<b>5</b>	<b>Electroadhesion zipping with soft grippers on curved objects</b>	<b>65</b>
5.1	Introduction . . . . .	65
5.2	Analytical formulation . . . . .	69
5.2.1	Gravitational energy . . . . .	71
5.2.2	Bending strain energy . . . . .	72
5.2.3	Electroadhesion energy . . . . .	72
5.2.4	Wrapping angle as a function of the applied voltage . . . . .	74
5.2.5	Alternative approach . . . . .	76
5.3	Materials and methods . . . . .	80
5.4	Results and discussion . . . . .	82
5.4.1	Quasi-static zipping tests . . . . .	82
5.4.2	Cycling zipping and unzipping tests . . . . .	84
5.4.3	Influence of coating materials . . . . .	84
5.4.4	Dynamic zipping and unzipping tests . . . . .	85
5.4.5	Influence of finger's mass . . . . .	86
5.4.6	Improving zipping performance . . . . .	86
5.4.7	Stiffening the electroadhesive fingers with layer jamming . . .	90
5.5	Conclusions . . . . .	96
<b>6</b>	<b>Conclusions</b>	<b>99</b>
6.1	Contributions . . . . .	101
6.2	Future work . . . . .	101
	<b>References</b>	<b>105</b>

# List of Figures

1.1	Examples of soft robotics applications in different fields . . . . .	3
2.1	Variable stiffness structures in animals and plants . . . . .	9
2.2	Examples of variable stiffness structures in hard robotics . . . . .	11
2.3	Examples of the four main variable stiffness strategies used in soft robotics . . . . .	15
2.4	Qualitative behavior of the three main jamming systems . . . . .	17
2.5	Jamming systems applications in soft robotics . . . . .	19
3.1	Electroadhesion working principle . . . . .	23
3.2	Electroadhesive gripper developed by Grabit Inc. . . . .	24
3.3	Electroadhesive gripper developed by NASA Jet Propulsion Laboratory	25
3.4	Electroadhesive soft gripper developed by Shintake et al. (Reproduced from [105]) . . . . .	26
3.5	Electroadhesive soft gripper with passive wrapping capabilities . . .	28
3.6	Force vs displacement test of the soft gripper developed in [105] . . .	29
3.7	Pick and place of fruit and vegetables with an electroadhesive soft gripper (Reproduced from [26]) . . . . .	30
4.1	Stiffness change and slip propagation in layer jamming systems (reported from [29]) . . . . .	37
4.2	Analytical model of four-layer jamming structures. . . . .	40
4.3	a) Longitudinal shear stress along the cross-section of the upper half of a multi-layer jamming structure at $x = 0$ , for three different values of $\sigma_1/\sigma_0$ . b) Plot of equation (4.12) . . . . .	42
4.4	Schematic representation of the transverse loads, axial and longitudinal shear stresses in the partial-slip phase of a multi-layer jamming structure.	42
4.5	Representation of the axial and shear stress experienced by a cantilever structure with four layers (reproduced from [30]) . . . . .	47
4.6	Qualitative representation of slip propagation experienced by a cantilever jammed structure with four layers. (reproduced from [30]) . .	48

## LIST OF FIGURES

4.7	The force vs. deflection relation for a multi-layer jamming structure with a different number of layers (reproduced from [28]). Analytical predictions (red) are compared with FEM results (blue) . . . . .	51
4.8	The force vs. deflection relation for a 20-layer jamming structure with different values of the vacuum pressure (reproduced from [28]). Analytical predictions (red) are compared with FEM results (blue). . . .	51
4.9	The force vs. deflection relation for a 20-layer jamming structure with different values of the coefficient of friction. (reproduced from [28]). Analytical predictions (red) are compared with FEM results (blue). .	52
4.10	Deformation phases in a 8-layer structure from FEM simulations . . .	53
4.11	a) Experimental set-up for the three-point bending tests. b) Fabrication process of the layer jamming structures. . . . .	55
4.12	Comparison between theoretical predictions, finite element simulations and experiments. . . . .	59
4.13	Influence of the length of the overhangs on the bending stiffness of layer jamming structures . . . . .	62
4.14	Comparison between the predictions of the basic model [28] that of the refined model [29] and finite element simulations . . . . .	62
5.1	a) Zipping of an electroadhesion (EA) finger ( $L = 48$ mm) on a cylindrical object ( $R = 30$ mm), measured by the wrapping angle $\alpha$ . . . .	66
5.2	Snapshots taken from Supplementary video 4 [81] . . . . .	68
5.3	Energy components of the system involved in the zipping process . .	70
5.4	Schematic representation of the infinitesimal increase in the wrapping angle during the zipping process . . . . .	71
5.5	Electrostatic energy and capacitance of the entire tape computed with COMSOL . . . . .	73
5.6	Visualization of the trends of the potential energy derivatives of Eq. 5.7	74
5.7	Schematic representation of reference systems and total potential energy contributions . . . . .	78
5.8	a) EA finger starting position for the experiments: the finger is vertical, tangent to the object . . . . .	81
5.9	Quasi-static zipping tests. Validation of the zipping model for two object's radii (30 and 45 mm), by applying increasing AC (a) and DC	83
5.10	Zipping and unzipping cycle for both AC and DC voltage ( $R = 30$ mm)	83
5.11	Comparison between model outcomes and experimental results of the wrapping of the EA finger around a curved object ( $R = 30$ mm) coated with different substrates. . . . .	85
5.12	Dynamic zipping and unzipping tests . . . . .	86
5.13	Influence of finger's mass . . . . .	87

5.14	Influence of dielectric layers thickness and spacing between the electrodes on the zipping performance of an EA finger . . . . .	89
5.15	Visualization of the simulated scenario. Rotation of a lime (200 g) with small deflection of the fingers (less than 1 mm). . . . .	90
5.16	Description of the layer jamming structures used in the simulations .	91
5.17	Analytical predictions of the Force vs deflection curves of the cantilever jamming structures with material properties and thickness equal to the ones used for the electrostatic clutches developed in [55] different number of layers . . . . .	92
5.18	Plot of equations 5.14 and 5.15 showing the voltages to initiate (V no zip) and complete (V full zip) the zipping process as a function of the object's radius, highlighting feasible and unfeasible (breakdown) design regions. . . . .	94



# List of Tables

4.1	Relationships between the applied load $F$ , the second moment of area $I$ and the deflection at the center of the structure $w$ . . . . .	40
4.2	Relationships between the applied load $F$ , the second moment of area $I$ and the deflection at the center of the structure $w$ , during the three deformation phases of a multi-layer jamming structure . . . . .	44





# Chapter 1

## Introduction

Inspired by the remarkable adaptability of biological systems, researchers started to harness the power of soft functional materials to create robots with unprecedented versatility and compliance. This new way of designing robots has given rise to a new field called Soft Robotics.

Functional materials refer to materials that possess specific properties or functionalities that allow them to enhance the capabilities of robotic structures. Materials that can convert electrical stimuli in mechanical work, structures capable of changing their mechanical impedance when subjected to external stimuli are some examples of the unique potential of these structures. Despite their widespread use in soft robotics, there are many aspects of their behavior that are still not fully understood, which limits the further development of these technologies.

This thesis seeks to address this issue, by exploring questions related to the mechanics of functional materials, leading to a wider understanding of their working principles and to the design of more advanced soft robotics applications.

In the first part of the thesis, I deeply explored the intrinsic mechanics of layer-jamming structures, which are a class of structures that exhibit unique mechanical properties, such as tunable stiffness and damping, when subjected to a pressure gradient. In the second part, I investigated the interplay between mechanical and electrical aspects in electroadhesion soft grippers, showing how this interplay influences the capability of these systems to self-adapt to curved and irregular objects.

### 1.1 Background and motivation

Hard robots are made, by definition, from rigid materials that deform only minimally when subjected to external loads. Although they can be very precise and powerful, they are usually designed for highly specialized tasks in contrast to the rich multifunctionality of biological systems. While hard robots excel in many industrial applications, their rigid structures represent a strong limitation in other circumstances. Due to their rigid structures, they can be potentially dangerous when they work in close contact with people or delicate items and they are not able to adapt autonomously to different shapes and tasks. To overcome these limitations, researchers started to explore a new generation of robots made of soft and functional materials capable of safely interacting with humans, unstructured environments and delicate objects.

The essential difference between traditional and soft robotics lies in the stiffness of the materials with which robots are made. Whereas rigid robots have few degrees of freedom and can be controlled very rapidly and precisely with well defined kinematics and dynamics, soft robots consist of deformable bodies with infinite degrees-of-freedom, which makes dynamic modeling and control a very challenging task. However, thanks to the deformability of their bodies soft robots are much better suited than hard robots for specific tasks in which the ability to conform autonomously without applying high forces is useful. For example, hard robotic grippers require accurate position and control of finger motion, while in soft grippers the control is minimal since they can exploit their mechanical compliance to self-adapt to the shape of the objects.

In the last decade, soft robots have already shown their potential to enter in our daily lives. For example, as shown in Figure 1.1a, soft pneumatically activated fingers have already entered the food market thanks to their unprecedented adaptability and ultra-gentle grasping force, showing the ability to successfully grasp a wide variety of delicate items, such as fruit, vegetables, cookies, and raw meat (Soft Robotics, Inc. [6]). Small-scale soft robots that can autonomously navigate in narrow and unstructured spaces [56] have shown potential in the construction of tissue scaffolds, biosensing, and targeted drug delivery (Figure 1.1b). Functional fabrics embedded with soft fiber-format pumps [110] and actuators [66] have paved the way to a new era in which wearable technologies could become less bulky and more comfortable (Figure 1.1d-e).

Despite there are examples of soft robotic applications that have already shown their clear advantages in solving problems in the real world, these represent just a

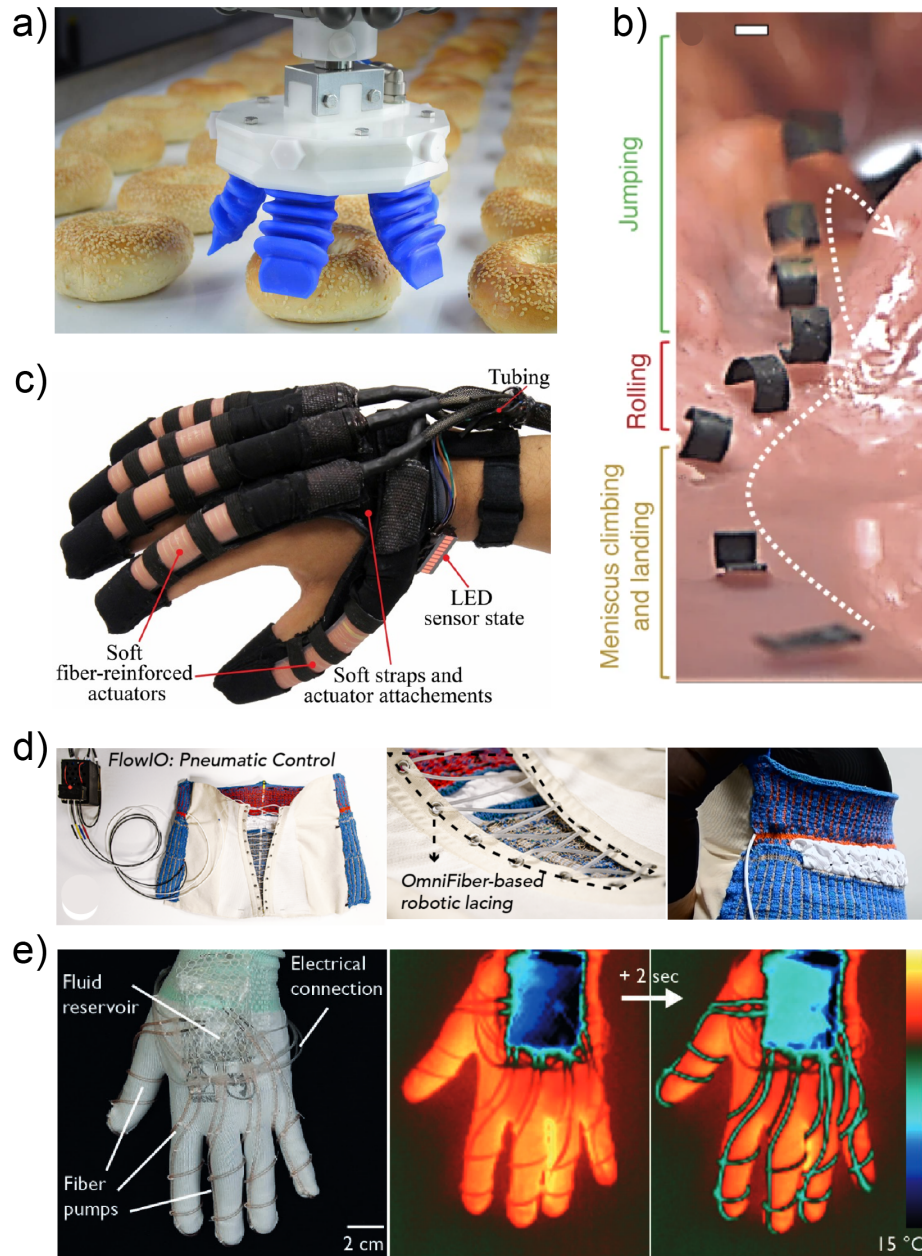


**Figure 1.1:** Examples of soft robotics applications in different fields. a) Soft elastomeric fingers that can grasp delicate items without damaging them (Soft Robotics, Inc.). b) Magnetically activated small-scale robot navigating a synthetic stomach phantom. (reproduced from [56]). c) Soft glove embedded with soft pneumatic bending actuators for rehabilitation exercises (reproduced from [92]). d) Functional fabric embedded with soft fiber-format actuators for breathing guidance during singing (reproduced from [66]). e) A thermal haptic glove with individually controlled fiber pumps for thermal regulation. (reproduced from [110])

small percentage of all the works that have been published in the field in the last decades. The majority of the technologies proposed are still in their early stage of development [53]. In addition to the common problems such as durability, controllability, and reliability there is still a vast amount of knowledge that has not yet been explored. In this effort, as I will explain in detail in the following chapters, this thesis seeks to shed light on the underlying mechanics of two promising soft robotics applications based on two different functional materials: i) variable stiffness devices based on layer jamming and ii) electroadhesion robotic grippers based on electroactive polymers.

In this paragraph, I just wanted to give a general overview on functional materials in soft robotics, highlighting their importance, limitations and the broad spectrum of applications in which they can be impactful. In Chapter 2 and Chapter 3, a more detailed overview of functional materials used in soft robotics will be provided, with a more comprehensive focus on variable stiffness structures and electroadhesion-based soft gripper, which represent the core of this thesis.

## 1.2 Thesis outline

- Chapter 2 introduces the concept of variable stiffness structures, highlighting their importance in biological systems and describing different ways in which variable stiffness can be achieved both in hard and soft robotics. Among the various techniques, jamming systems are highlighted, providing a general background on how these systems work, what are their advantages and disadvantages and what makes them useful for soft robotics applications.
- Chapter 3 provides an overview of electroadhesion-based soft grippers, describing their working principle, different grasping strategies, and main limitations.
- Chapter 4 thoroughly investigates the intrinsic mechanics of layer jamming systems. It presents a novel analytical model to capture their nonlinear response beyond the initial (elastic) deformation phase. The model predicts that the gradual change in the partial-slip phase is related to the subsequent slip between adjacent layers. In particular, it shows that slip starts at the innermost interface and propagates outward. Analytical predictions are compared with experiments and finite element simulations, showing an excellent agreement, especially considering that no fitting parameters have been used.

- Chapter 5 investigates the interplay between mechanical and electrical aspects of the electrostatic zipping in electroadhesion-based soft gripper. It presents an analytical model based on the energy balance between bending stiffness, finger mass, and electrical energy stored in the finger. The relation between applied voltage, wrapping angle, and bending stiffness of the finger is investigated, showing that the zipping phenomenon is governed by two voltage thresholds. It presents also the results of the experiments conducted on curved objects with different geometries and materials and the comparison with analytical predictions. Finally, it provides design tools for the fabrication of improved passively wrapping EA soft grippers, highlighting the mutual relationship among electrical and mechanical parameters of the systems and how it practically influences zipping in EA grippers.



# Chapter 2

## Variable stiffness structures

### 2.1 Variable stiffness structures in nature

Billions of years of evolution have created extraordinarily complex structures capable of performing amazingly complex tasks [43]. Understanding how these natural structures work and how they can achieve these outstanding performances represents a very interesting challenge that has already inspired solutions to practical engineering problems [18]. This paragraph briefly summarizes examples of biological structures that have developed variable stiffness techniques to perform complex tasks, generate motion, and efficiently interact with the environment.

Octopuses, for example, are invertebrate aquatic animals that can change their length, squeeze into very tiny holes, and bend their tentacles in all directions. To achieve these unique features, octopuses have developed a peculiar muscular structure, called muscular hydrostat [65], which is also found in the tongues of many terrestrial vertebrates and trunks of elephants. The most important feature of this structure is that it preserves its volume during deformation. Therefore, elongation, shortening, and bending are all movements generated by the selective contraction of different muscle fibers along their bodies. Figure 2.1a shows consecutive snapshots of the movement of an octopus's tentacles approaching a target, highlighting the continuous propagation of selective stiffening of muscle fibers during motion [113].

Plants, on the contrary, have developed another very interesting way to move and adapt to the environment. Instead of having soft contractile proteins (muscle fibers), their cells are surrounded by a much stiffer permeable outer membrane that allows them to sustain a very high hydrostatic pressure ( $\sim 5$  bar) known as turgor pressure. Depending on the amount of water stored inside the cell, the pressure changes causing



the expansion or reduction of the cell volume which in turn generates motion and growth in plants [40]. This phenomenon can be easily observed in spruce cones, in which water absorption causes the opening of seed scales triggered by cell-wall swelling (Figure 2.1b). Plants exhibit also differential swelling in different parts of their structures [45]. This is caused by the different orientations of cellulose fibrils that wind around the walls of the cells (Figure 2.1c). The stiffness of the structure is directly influenced by the orientation of the fibrils with respect to the long axis of the cells (Figure 2.1d). Researchers [44] have found that in tree branches, regions with different fibril angles are arranged in a way that swelling causes internal stress that generates an upward bending of the branches, as shown in (Figure 2.1a).

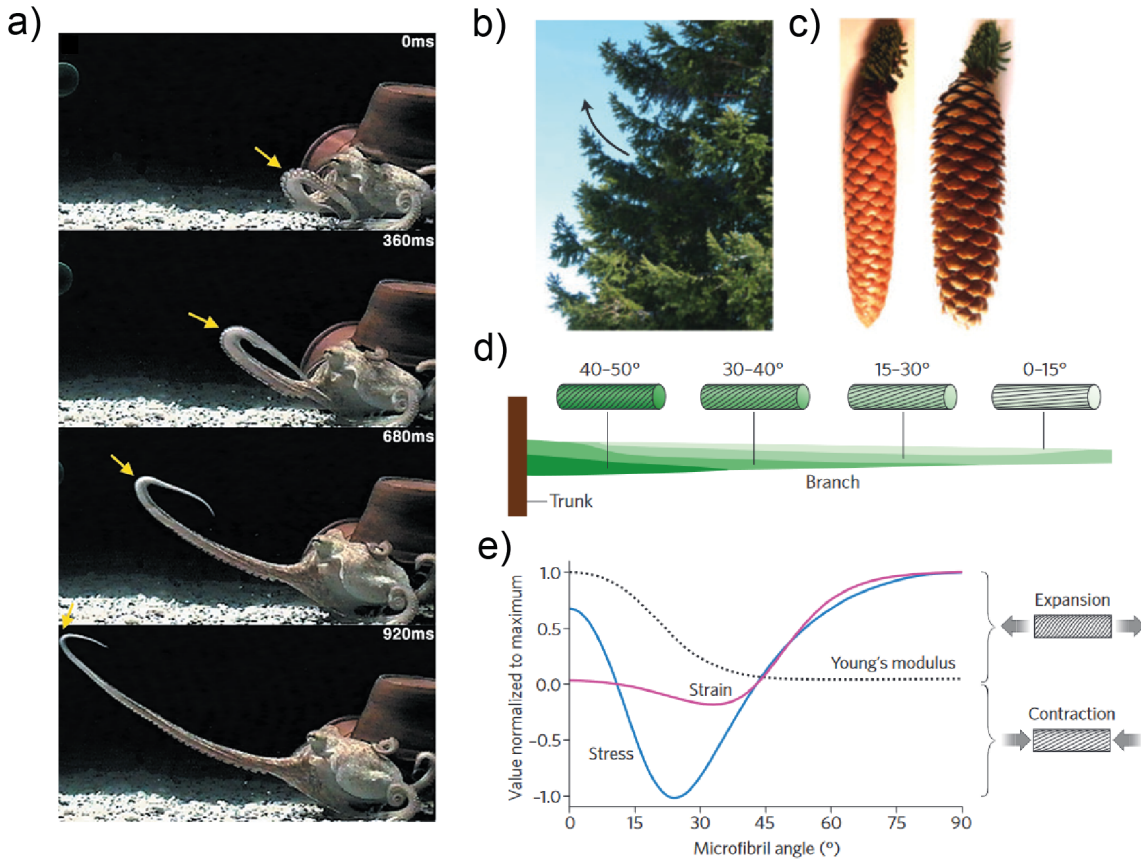


**Figure 2.1:** Variable stiffness structures in animals and plants. a) Snapshots of an octopus moving its arm to reach a target. Yellow arrows indicate the propagation of stiffening during motion (reproduced from [113]). b) Spruce branches bent upwards by cell-wall swelling (reproduced from [43]). c) Spruce cones close and open their seed scales when wet (left) and dry (right) (reproduced from [43]). d) Schematic colour map that indicates the hierarchical orientation of cellulose fibril in branches (reproduced from [43]). e) Stress, strain and Young's modulus variation as a function of the orientations of the fibrils (reproduced from [43]).

### 2.2 Variable stiffness structures in hard robotics

As detailed in the previous paragraph, the incredibly intricate structures of animals and plants, coupled with their highly efficient neuro-mechanical control systems, still far surpass the capabilities of mechanical systems engineered by humans. One of the crucial aspects that determine this unmatched performance lies in the adaptable compliance of biological structures compared to that of traditional robots designed by humans. However, motivated by the need to design robots in applications such as legged locomotion, rehabilitation devices, and tasks in human proximity, researchers realized that to satisfy these new challenging requirements they needed to introduce variable compliance in the mechanical structures of the robots.

A recent excellent review [118] provides a very detailed and well-organized overview of all the different strategies that engineers have developed to achieve variable stiffness in mechanical structures. Following their classification, variable stiffness structures can be divided into two categories:

- **Active compliance by control:** The variable compliance behavior is fully simulated by software algorithms. Coupled with the actuator there are always at least one sensor that measures the error with respect to the desired output and one controller that computes the correction to be sent to the actuator in a closed-loop configuration. Using this strategy, no energy is stored into the system and there is theoretically the possibility to tune the mechanical impedance on demand with an infinite range of stiffness and speed. These solutions were pioneered by DRL and commercialized by KUKA [19].
- **Inherent compliance:** These systems contain a compliant element in their structures and can be further classified in two sub-categories:
  - **Fixed compliance:** These systems still need a controller to achieve variable impedance, but they have the advantage of storing energy and absorbing impact shocks. The stiffness is constant and the force control problem is converted into a position control problem which is much easier for a gear train and greatly improves force accuracy. One of the most famous examples of these systems has been proposed in [93], and it is known as "Series Elastic Actuator" (SEA), in which a spring is placed in series between the actuator and the load.

- **Adaptable compliance:** These systems can both store energy and alter their stiffness. However, they require two motors: one controls the equilibrium position of the elastic element and the other one controls the stiffness. To achieve adaptable compliance engineers have found solutions that can be divided into 3 main groups: changing spring preloads, changing transmission between load and spring and altering the physical structures of the compliant elements.

Figure 2.2 shows examples of the three main types of variable stiffness architectures proposed in hard robotics: active compliance by control (Figure 2.2a), fixed compliance (Figure 2.2b) and adaptable compliance (Figure 2.2c).

The classification provided in this paragraph represents just an overview of the main strategies to achieve variable stiffness in hard robotics. However, this description represents just the tip of the iceberg of a much wider research field. Going into further details is out of the scope of this thesis.

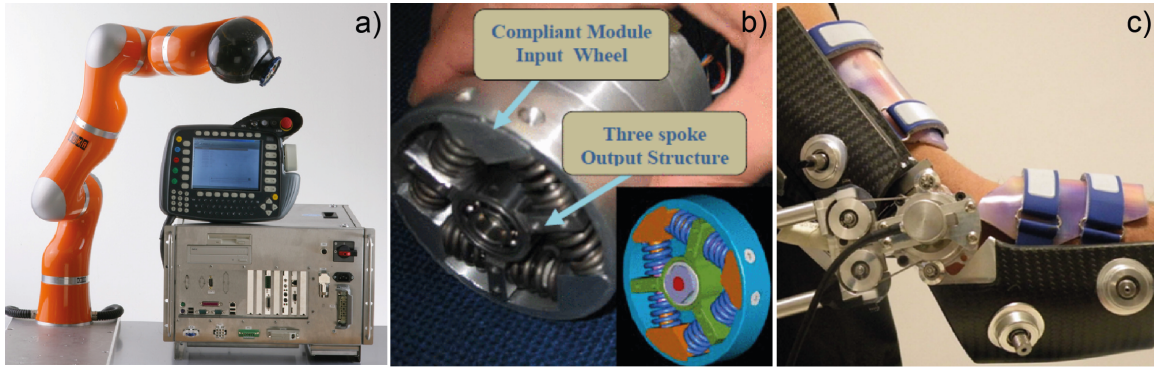


**Figure 2.2:** Examples of variable stiffness structures in hard robotics. a) The first commercially available robotic manipulator with active compliance control, developed by KUKA and DRL in 2008. (reproduced from [19]). b) Compact rotary series elastic actuator developed for the "iCub" robot, a child-size humanoid robot. The desired stiffness is obtained by combining passive compliance with active compliance control based on velocity regulation. (reproduced from [117]). c) NEUROExos, a powered elbow exoskeleton with an antagonistic actuation system with an independent joint position and stiffness control (reproduced from [120]).

## 2.3 Variable stiffness structures in soft robotics

In soft robotics, the approaches proposed to achieve variable stiffness are substantially different from the ones proposed in hard robotics. As described previously, variable stiffness in hard robots has been introduced with two main strategies: active compliance by control and inherent compliance. In both strategies, the material properties are kept fixed, and stiffness variation is obtained either by software control or by elastic springs arranged in different configurations and coupled with one or multiple actuators in series.

On the contrary, in soft robotics, variable stiffness is mainly based upon systems made up of functional materials that can change their mechanical properties (in terms of either Young's modulus or moment of inertia) when activated by external stimuli [79, 123]. Moreover, they can often do it reversibly with very limited displacement and volume variation. This alternative way of achieving tunable stiffness has paved the way for new engineering applications in a wide variety of fields such as soft grippers, medical devices, haptic interfaces, and wearable robotics.

Depending on the source of the external stimuli, variable stiffness structures can be divided into four main categories: thermally enabled, magnetic field induced, electric field stimulated, and pressure-controlled stiffness tuning.

- **Thermally enabled:** Materials that exhibit stiffness variation when subjected to thermal stimulation are mainly shape memory materials (SMM), and low melting point materials (LMPM). In SMM, stiffness variation is obtained by changing the material temperature above or below the glass transition temperature ( $T_g$ ). The atomic structure of these materials shifts from a crystalline or semi-crystalline phase (below  $T_g$ ), in which the Young's modulus is higher, into a viscous or rubbery phase (above  $T_g$ ) in which the Young's modulus is lower. In LMPM, instead, stiffness variation is due to phase change at the melting temperature ( $T_m$ ). At temperatures below  $T_m$  the stiffness of the structure is much higher since the structure is solid, while when the temperature exceeds  $T_m$  the structure changes phase and becomes liquid, resulting in a very large stiffness variation. A notable example of this behavior has been shown in a variable stiffness soft actuator [106]. It consists of a pre-stretched DEA combined with a LMPM substrate. The bending motion is controlled by applying a voltage to the DEA. When the LMPM is in the liquid state the actuator is in its soft state and can freely bend, whereas when the LMPM is activated it becomes rigid and the actuator can maintain a fixed shape (Figure 2.3a).

- **Magnetic field induced:** Magnetorheological fluids (MRFs) and elastomers (MREs) represent a class of materials that change their mechanical properties when an external magnetic field is applied. In general, these materials are obtained by introducing magnetic particles of different shapes and sizes into a dielectric fluid such as silicon oil in the case of MRFs, and in a polymeric matrix in the case of MREs. In MREs, magnetic particles are usually arranged in an anisotropic composite chain-like microstructures. When the external magnetic field is applied the interactions between the magnetic dipoles inside the materials help the structure to counteract mechanical deformations, thereby enhancing its stiffness. Due to their ability to control their stiffness rapidly and accurately, they have already found industrial applications as shock absorbers and damping oscillators. In soft robotics, they have found promising applications in different fields. For example, in the work of Koivikko et al. [70], MRFs have been proposed as a stiffening method in soft robotic grippers. The membrane of their gripper is filled with a MRF, that allows the gripper to conform to the target object in its soft state and then rapidly shift to the rigid state upon magnetic activation, as shown in Figure 2.3b
- **Electric field stimulated:** Materials that exhibit a change in stiffness in response to an applied electric field can be broadly classified into two distinct categories based on their underlying mechanisms of operation: electrostatic approaches such as electrorheological materials, dielectric elastomers, and electrohydraulic that uses high electric fields to generate attraction forces or particle alignment inside the materials, and electrically induced phase change approaches that generally require lower voltages to trigger chemical reactions which cause the movement of ions. In general, the stiffness range is higher in phase change approaches rather than in electrostatic solutions. However, stiffness variation caused by the phase change is much slower than that generated with electrostatic approaches. For this reason, in applications that require very fast stiffness tuning, electrostatic approaches are generally preferred. Figure 2.3c shows an example of an electrostatic approach used to vary the stiffness of a haptic glove [54]. The glove is embedded with electrostatic clutches in which the electrostatic attraction is altered by the applied voltage, resulting in a change in frictional forces between the top and bottom layers of the clutch. In this way, by simply controlling the driven voltage the authors have been able to virtually simulate the stiffness of different objects in a virtual reality scenario

- **Pressure controlled:** Systems in which the stiffness can be controlled with fluid pressure can be divided in two groups: flexible fluidics actuators (FFAs), and jamming systems. FFAs are generally flexible patterned elastomeric chambers that bend when inflated with a fluid. When three FFAs are symmetrically arranged and simultaneously actuated, bending motion is prevented and the bending stiffness can be tuned by altering the pressure inside the chambers, similar to the stiffening strategies of the muscular hydrostat found in nature. Jamming systems instead generally consist of granules, fibers or layers confined in an airtight membrane connected to a vacuum source. When vacuum pressure is introduced inside the membrane, frictional coupling increases, resulting in a dramatic change in stiffness. One of the most famous applications of the jamming phenomenon is represented by the universal gripper developed by Brown et al. [25]. The gripper consists in a membrane filled with grains and connected to vacuum. In the unjammed state (vacuum OFF) the gripper is soft and can conform to the objects without damaging them. In the jammed state (vacuum ON), instead, the gripper becomes rigid and is able to grasp and hold the objects from the top, as shown in Figure 2.3d.



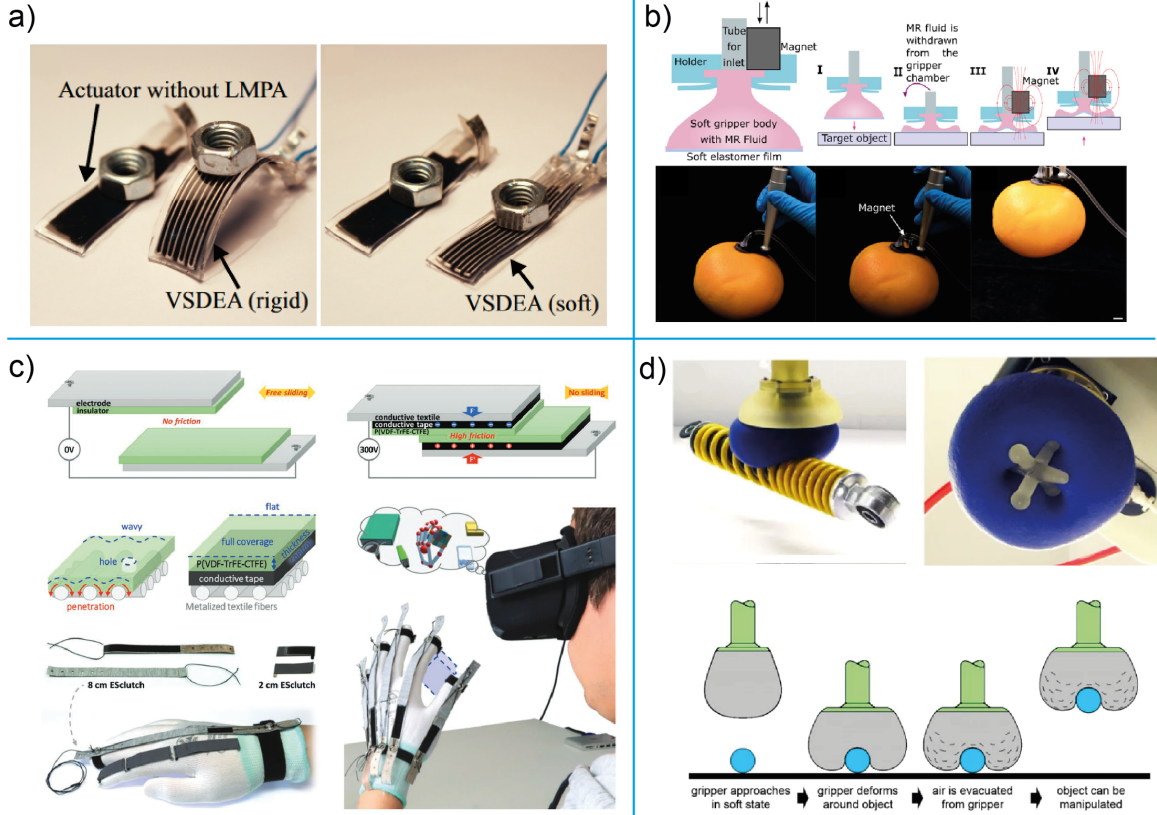


**Figure 2.3:** Examples of the four main variable stiffness strategies used in soft robotics. a) Variable stiffness actuator composed of a dielectric elastomer actuator (DEA) coupled with a low melting point alloy (LMPA). The stiffness of the actuator is dramatically increased due to the phase change experienced by the LMPA at the melting temperature  $T_m$  (reproduced from [106]). b) Magnetically switchable soft gripper. The soft membrane of the gripper is filled with a magnetorheological fluid (MRF) that allows stiffness tuning by magnetic stimulation, during the different phases of a pick and place (reproduced from [70]). c) Variable stiffness haptic glove embedded with electrostatic clutches. The electrostatic attraction between the top and bottom layers of the clutch is altered by the applied voltage, resulting in a change in friction forces. This phenomenon has been exploited to simulate the stiffness of different objects in a virtual reality scenario (reproduced from [54]). d) Universal soft gripper based on the jamming of granular material. The gripper is composed by a membrane filled with grains and connected to a vacuum source. The gripper approaches the target objects in its soft unjammed state (vacuum OFF) and subsequently enters in its hard jammed state (vacuum ON) to grasp the object. (reproduced from [25])



### 2.3.1 Jamming systems

Among the different stiffening methods discussed in the previous paragraph, layer jamming systems are the ones that I deeply explored in this thesis. Therefore, in this paragraph, I want to give a more detailed overview of jamming systems, to provide a general background on how these systems work, what are their advantages and disadvantages and what makes them useful for soft robotics applications (Figure 2.5).

Jamming in soft robotics refers to a purely mechanical phenomenon in which a material transitions from a rigid to a soft state when external forces such as shear or compression act on it. In most cases, jamming structures are made of particles, fibers, or layers and the jamming transition is triggered by a vacuum pressure.

Granular jamming systems (Figure 2.4a) have been the first to be proposed and due to their presence in other fields such as agriculture and the food industry, they have been also the most studied. The granules that have been mostly used are coffee grounds, glass, and plastic spheres. They are usually confined in an airtight bag made of stretchable materials such as silicone and latex rubber. In the unjammed (soft) state, also called the fluid-like state, the particles can easily rearrange and slide on top of each other, resulting in a structure that is very malleable and compliant. When the pressure inside the bag is decreased, the pressure gradient between the atmospheric pressure outside and the vacuum pressure inside the bag, squeezes the particles together, limiting their rearrangement and resulting in a dramatic increase in the stiffness of the structure. Due to their excellent conformability and the ability to harden in all directions, granular jamming systems have found promising applications, especially in haptic interfaces and soft grippers. Despite their widespread use in soft robotics, there are still unknown fundamental questions related to their behavior. Mathematical models based on continuum theories [21], discrete element methods [76], and statistical mechanics [16] have been proposed, but they are often limited to circular particles and simple geometries, making them still unfeasible to be used in real applications.

In layer jamming structures (Figure 2.4c), instead, particles are replaced with layers. The most common material explored by researchers is copy paper, but they have also used other materials such as sandpaper, PLA, and polyethylene films. In general, the jamming phenomenon can be exploited with any kind of sheets of different material, surface properties, and dimensions. The stiffness change in these structures is entirely governed by the shear stress at the interface between the layers. In the unjammed state, the layers are free to slide with respect to each other and

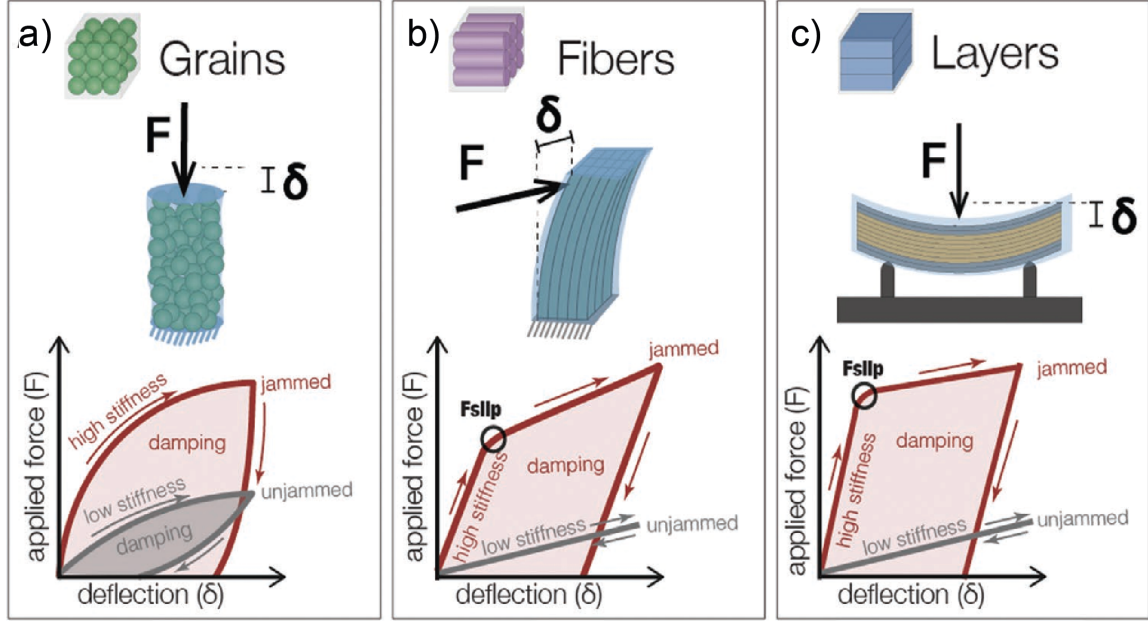


**Figure 2.4:** Qualitative behavior of the three main jamming systems (reproduced from [11]). a) Granular jamming systems loaded in compression, exhibit a remarkable change in stiffness between the jammed and unjammed state. In contrast to layers and fibers, stiffness gradually decreases upon loading, without a distinct yielding. Damping is also present in the unjammed state due to the irreversible rearrangement of particles between loading and unloading. b) Fiber jamming systems loaded in a cantilever configuration, also exhibit a dramatic increase in stiffness when jammed. The structure behaves as a cohesive elastic beam in the first phase of deformation. Then, after the first slip, stiffness decreases and energy is dissipated by the slip between the fibers. In the unjammed state, the stiffness is low and the behavior is purely elastic without damping. c) Layer jamming structures subjected to three-point bending tests behave similarly to fiber jamming systems. When the external load is low, shear stress at the interfaces between layers is lower than the friction limit and the structure behaves as a cohesive beam. As the external load is further increased, shear stress exceeds the friction limit, layers start to slide energy is dissipated and the stiffness gradually decreases. No energy is dissipated in the unjammed state.

the stiffness of the structure is low. When vacuum is introduced inside the airtight membrane, layers are squeezed together, causing an increase in frictional coupling between adjacent layers. As a result, the structure becomes much more rigid and the system behaves as a cohesive beam. The structure remains in this rigid state until the shear stress does not exceed the static friction limit when subjected to external loads. From this point on, as the external loads are further increased, layers begin to slip and the bending stiffness gradually decreases. When all the layers enter in slip, the longitudinal shear stress is constant and equal to the maximum frictional limit along all the interfaces, and the bending stiffness becomes almost equal to that of the unjammed state. Due to their higher stiffness ratio and better controllability of directional stiffness and damping, they have been proposed as wearable devices [9], landing gears [85] and surgical manipulators [68]. Although multiple studies have been published on the behavior of these systems, they have not yet provided explanations on the mechanics of multi-layer jamming systems beyond the initial deformation phase. This thesis has tackled this and other open questions, showing how the change in stiffness in these systems is related to slip propagation between adjacent layers inside the structure. A more detailed analysis of the complex intrinsic mechanics of these structures is provided in Chapter 4.

Fiber jamming (Figure 2.4b), on the other hand, can be considered as a combination of layers and granular jamming approaches. Instead of layers and granules, the airtight bag is filled with fibers. In a plane parallel to their cross-section, the fibers can easily slide and rearrange like the granules in their fluid-like state, whereas on the other two orthogonal planes, the fibers slide with respect to each other similar to the behavior of layers. The next chapter provides an overview of electroadhesion-based soft grippers, which have been the main focus of the second part of this thesis, describing their working principle, different grasping strategies, and main limitations.

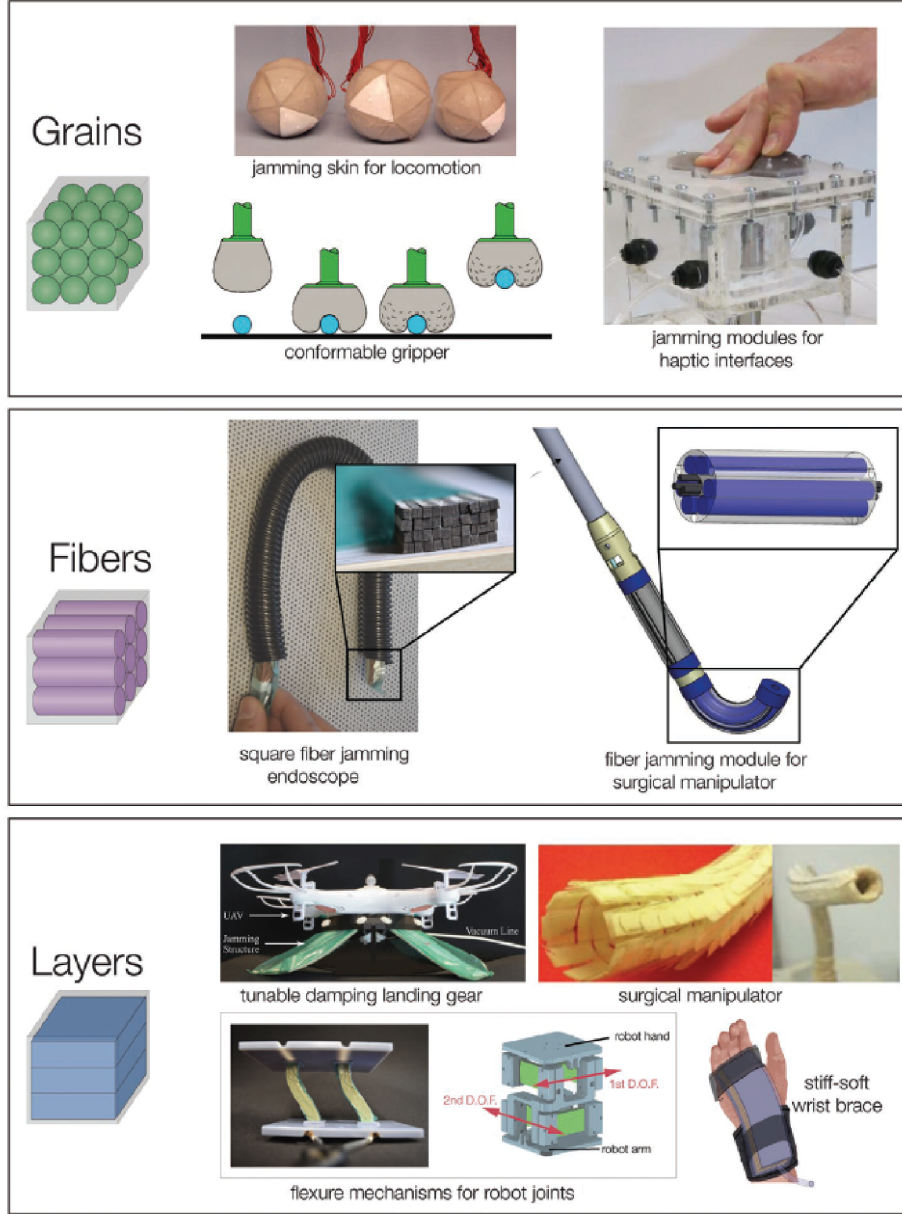


**Figure 2.5:** Jamming systems applications in soft robotics (reproduced from [11]). a) Granular jamming systems proposed as skins for locomotions [112], conformable grippers [25] and haptic interfaces [111]. b) Fiber jamming structures integrated into medical devices such as endoscopes [10] and surgical manipulators [23]. c) Layer jamming structures integrated in drones as tunable damping landing gears [85], flexure mechanisms for robot joints [9], surgical manipulators [68], and wrist braces [84, 63].



# Chapter 3

## Electroadhesion soft gripper

Electroadhesion (EA) soft grippers are a class of soft grippers in which the grasping force is controlled by electrostatic forces. Thanks to their unique features such as silent operation, ultra-low power consumption, fragile object manipulations, and the ability to create adhesion with almost any surface even in vacuum conditions, they have a great potential to revolutionize the gripper industry in the next years.

The phenomenon of electroadhesion is not new, it was discovered more than one century ago [62] and in the last decades it found commercial applications in different fields. In 1953, electroadhesion was introduced in the first plotters to solve the issue of holding papers during the printing process [2]. In the early 1960s, NASA and Chrysler Space Division started to explore the feasibility of exploiting electroadhesion as a means for helping astronauts to perform experiments during missions in zero-gravity environments. In 1970, EA rigid grippers (known as electrostatic chucks) found commercial applications in the semiconductor industry to automate the handling of silicon wafers, and a few years later they were introduced in the textile industry [82] to handle fabrics [4].

Despite these grippers have found commercial applications in the semiconductors and textile markets, they are far from revolutionizing the gripper industry since they are mostly limited to almost perfectly flat and lightweight objects. The vast majority of the studies conducted in the last century were based on rigid materials and were mainly focused on the optimization of electrical properties (dielectric insulating materials and electrode geometries) while the mechanical aspects were almost completely neglected.

Only recently, mechanical aspects have started to be explored. In the last decade, there was a paradigm shift in which researchers started to design electroadhesives grippers made of stretchable and flexible materials. Thanks to this new approach the grasping performance of electroadhesive grippers were dramatically increased. Exploiting the inherent compliance of the gripper components, researchers have shown that soft electroadhesive grippers can autonomously conform to a wide variety of shapes and sizes (highly irregular and curved objects) creating a sufficiently large contact area that allows them to lift objects 600 times higher than their own weight [26].

This new way of designing electroadhesive grippers has led to new and interesting challenges. Mechanical aspects such as peeling and zipping have been discovered to be as important as the electrical aspects and need to be investigated in order to achieve better performance. Understanding the interplay between mechanical and electrical aspects represents one of these challenges that could lead to the development of the next generation of electroadhesive soft grippers that will have all the characteristics to be a valid alternative to the grippers currently used in industry.

In this Chapter, I want to give a general overview of electroadhesive soft grippers, to provide a general background on how these grippers works and what are their advantages and limitations.

Later in Chapter 5, I will discuss in detail the parameters that influence the capabilities of these systems to self-adapt to curved and irregular objects and how to improve their grasping performance.

## 3.1 Electroadhesion working principle

The working mechanism of electroadhesion used in soft grippers applications is illustrated in Figure 3.1. It usually consists of interdigitated electrodes embedded in a dielectric material and connected to an high voltage power source. When a high voltage is applied across the electrodes, charges of the opposite sign accumulate on the electrodes. These charges create fringe electric fields that thanks to the interdigitated design penetrate in the target object inducing surface polarization charges. This polarization is responsible for the mutual attraction between the finger and the object, which generates the electroadhesion force, as shown in Figure 3.1. Electroadhesion forces can be generated both in dielectrics and conductors. In conductors, charges are free to move, and opposite charges migrate towards the electrodes mirroring the distribution of charges of the finger in contact. In dielectrics, charges are not free to move, what happens instead is that the fringe electric fields polarize the



molecules inside the dielectric, resulting in a net adhesion force between the finger and the polarized object. Typically to generate a sufficiently high electrode adhesion force voltages in the range of 1 to 5 kV are required. One of the most important challenges is represented by the very slow release time. When the voltage is switched off residual charges remain accumulated at the interface between the gripper and the object, resulting in a residual attraction force that hinders the release. Mechanisms to speed up the release will be discussed later in this chapter.

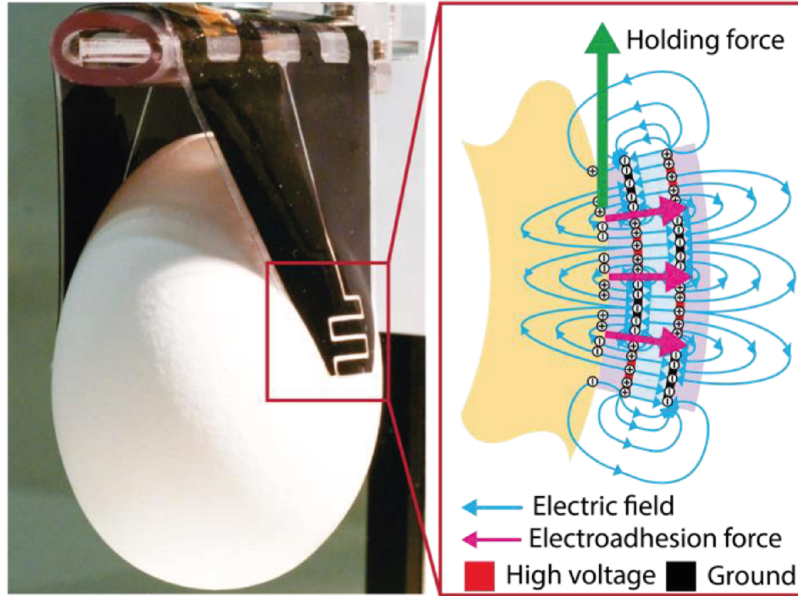


**Figure 3.1:** Electrode adhesion working principle. (Reproduced from [27]). Visualization of the electric field lines and charge distributions that generate the electroadhesion force when high voltage is applied to the electrode adhesion soft gripper.

## 3.2 Active wrapping

The most common design used in electrode adhesion soft grippers is composed of two or more electrode adhesion fingers that grasp the objects from the sides. EA creates mutual attraction between the fingers and the objects, resulting in a large shear force with negligible compression. To achieve this large shear force the fingers need to effectively wrap around the lateral surfaces of the objects establishing the largest possible contact area. This wrapping can be achieved in two ways, 1) actively (using an actuator), 2) passively (using only the attraction generated by the electrode adhesion forces). This section will explore active wrapping techniques, while the following sections will delve into passive wrapping methods.



### Chapter3. Electroadhesion based soft gripper

---

Figure 3.2 shows the gripper developed by Grabit Inc.[4]. The gripper is made of 8 flexible electroadhesive fingers. The angular spacing between adjacent fingers is 45 degrees, with the fingers evenly distributed around the center of the gripper. Flexible wires are attached at the tip of each finger and connected to an electromagnetic motor. The gripper approaches the objects in the "open" configuration as shown in Figure3.2a-c. Then the electromagnetic motor moves and the fingers are bent towards the object by the flexible wires. When the fingers are really close to the object, high voltage is applied, electroadhesion pressure ensures high shear forces and the objects are successfully grasped Figure3.2b-d. The release is achieved by reopening the fingers moving the motor to the opposite side. In [3] the device is shown handling different types of objects such as a metallic can, a plastic bag, and a cookie box.

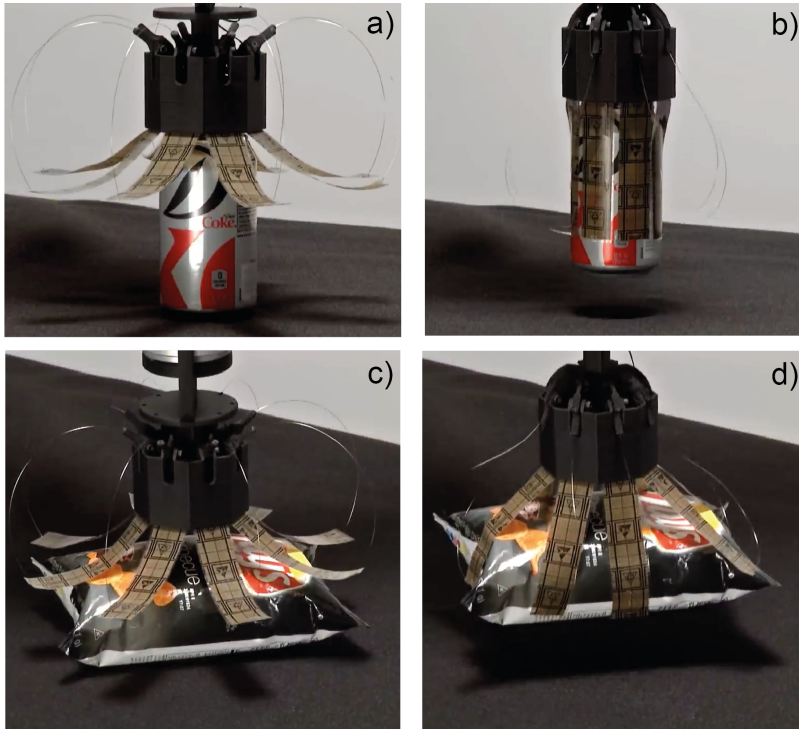


**Figure 3.2:** Electroadhesive gripper developed by Grabit Inc. (Snapshots extracted from the video on the Grabit Inc. website [3]) . The gripper is made of 8 flexible electroadhesive fingers connected to an electromagnetic motor through 8 flexible wires.

Following a similar approach researchers at NASA Jet Propulsion Laboratory developed an electroadhesive grippers for the manipulation of multi-layer insulation (MLI) blankets that provide thermal and debris shielding for satellites [102]. The gripper has been designed to grasp large flexible substrates with minimal preload maintaining the sheets through a wide range of motions and controlling the release with negligible pulling forces. The gripper is comprised of a linear actuator, a com-

pliant spacer and 8 electroadhesive fingers connected to the linear motor through tendons. Figure 3.3 shows the gripper design. In this case, the gripper is less versatile, since the fingers start flat and the motor controls only the disengagement. Therefore only flat or concave shapes can be grasped with this design. The release mechanism is governed by the peeling generated by tendons that are pulled by the linear actuator, as shown in Figure3.3.

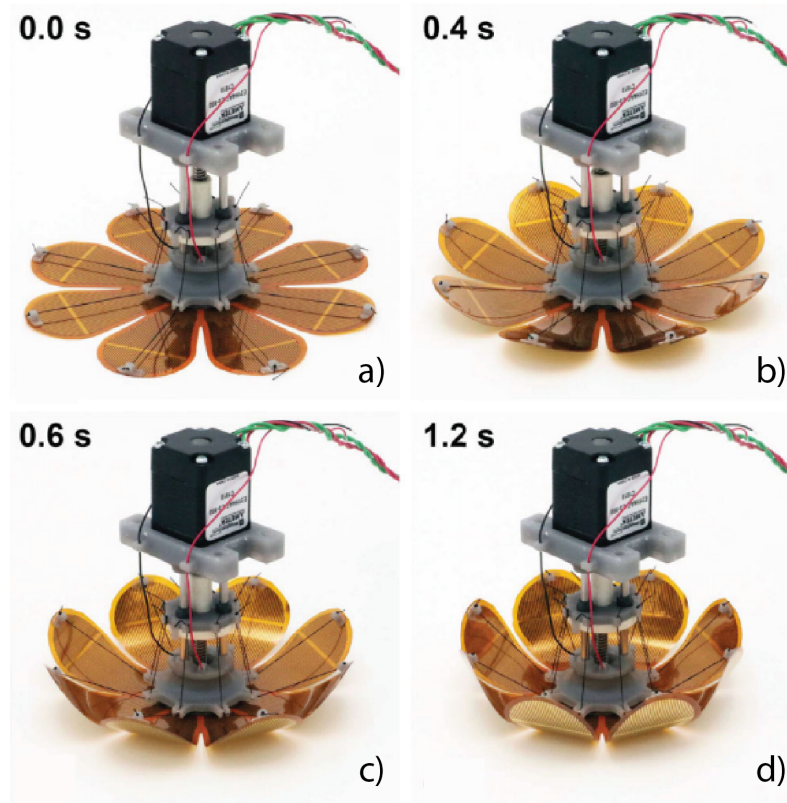


**Figure 3.3:** Electroadhesive gripper developed by NASA Jet Propulsion Laboratory (Reproduced from [102]). A linear actuator controls the tension in the tendons, which peel off the fingers from the grasped object.

### Chapter3. Electroadhesion based soft gripper

A completely different approach has been proposed by Shintake et al. [105]. They proposed a novel method to create electroadhesive soft grippers in which the actuators are directly integrated inside the fingers. The actuation mechanism is achieved using dielectric elastomer actuators. The internal structure of the fingers is shown in Figure 3.4a.

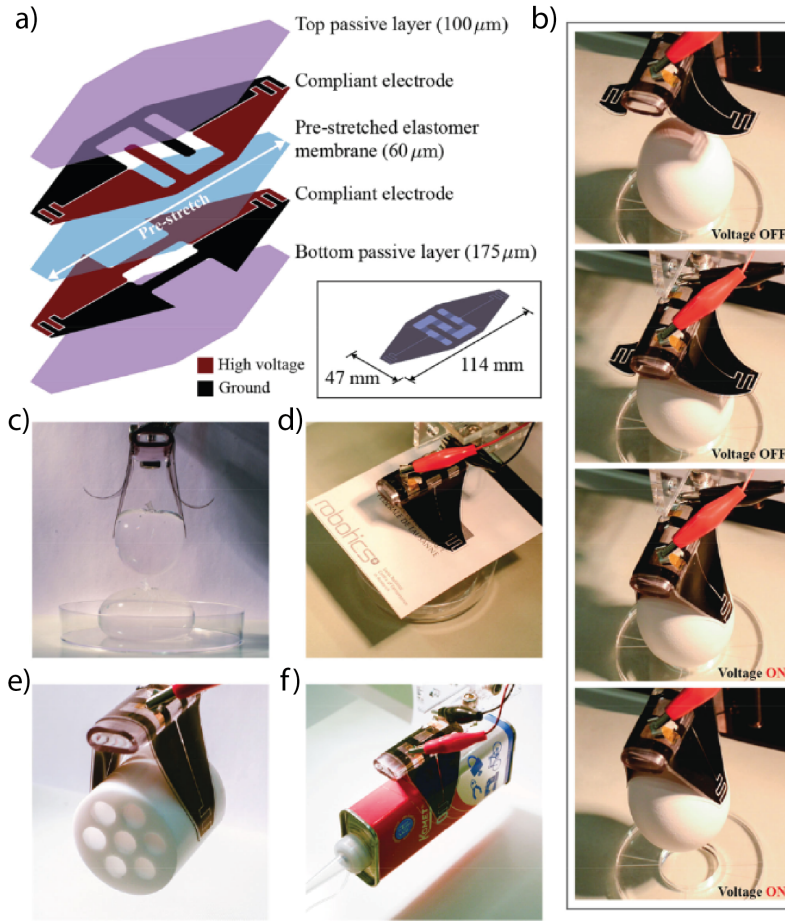


**Figure 3.4:** Electroadhesive soft gripper developed by Shintake et al. (Reproduced from [105]). a) Internal structure of the gripper. b) Demonstration of the actuation mechanism. When the voltage is zero the fingers are curled (open configuration). When the voltage is applied the fingers are actuated and bend toward the objects (closed configuration). The objects are then picked up thanks to the holding force generated by electroadhesion. Successful grasping has been demonstrated on a c) water-filled balloon (35.6 g), d) a flat paper (0.8 g), e) a Teflon tube (80.8 g) and f) a metallic can (82.1 g)

The initial curl shape in the rest state (zero applied voltage) is obtained by using a pre-stretched DEA (formed by an elastomer membrane sandwiched between two compliant electrodes) bonded between two passive layers. In this configuration, the internal stress of the pre-stretched membrane is in equilibrium with the bending

energy accumulated by the passive layers causing the fingers to be curled. Then when a high voltage is applied, the electrostatic pressure generated by the DEA reduces the internal stress resulting in a bending motion toward the object (Figure 3.4c). In this way, the fingers actively conform to the surfaces of the object and thanks to the compliance of the fingers there is no risk of damage caused by the compressive forces. Figure 3.4b shows the grasping of a raw egg demonstrating both the ability to actively conform to the lateral surface of the eggs and the negligible compression forces exerted on them.

In the following section, we will present electroadhesive soft grippers that can autonomously wrap around the object without the need of any external actuators.

### 3.3 Passive wrapping

Passive wrapping represents a promising alternative to active wrapping. Although adding actuators has the advantage of independent active control of the finger motion helping the fingers to envelop the object macroscopically, they usually increase the stiffness of the fingers which negatively influences the actual contact area between the gripper and the object at small scale. Moreover, their fabrication is usually more complex, as in the case of the gripper shown in Figure 3.4.

In contrast, passive wrapping (also known as electroadhesion zipping) leverages electrostatic forces to wrap the fingers around the object without added stiffness, maximizing conformability also at the roughness scale.

This idea has been implemented in the electroadhesive soft gripper developed by Cacucciolo et al. [26]. The gripper has two electroadhesive fingers mounted on a motorized holder. The distance between the fingers is controlled by the rotation of the servomotor. Depending on the size and shape of the objects the relative position between the fingers is adjusted to bring the fingers tangent to the lateral surface of the objects, as shown in Figure 3.5a. Then when a high voltage is applied to the fingers the fringe electric fields polarize the molecule of the object generating a mutual attraction. Thanks to the very low bending stiffness and weight of the fingers, this mutual attraction causes the fingers to wrap around the object leading to very high grasping forces.

During wrapping the fingers bend and lift their center of mass. Therefore the wrapping angle that can be achieved and consequently the holding force, will strongly depend on the ratio between the electrical forces that generate attraction and the mechanical restoring forces. Understanding the interplay between mechanical and

electrical aspects is crucial in these grippers. In Chapter 5 we developed an analytical model to describe this zipping process and we also performed experiments to test the model outcomes, showing the underlying physics that govern this behavior.

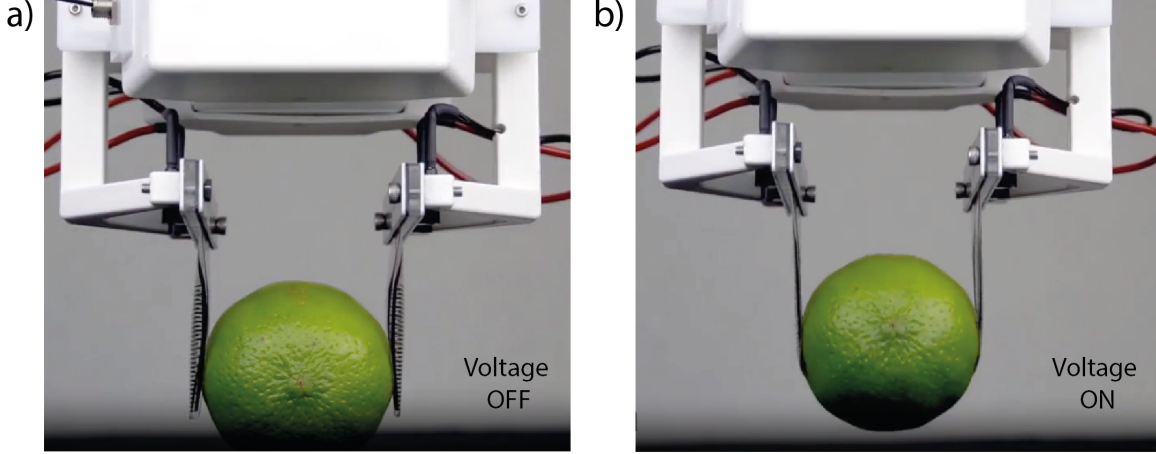


**Figure 3.5:** Electroadhesive soft gripper with passive wrapping capabilities (Reproduce from [26]). The electroadhesive fingers are mounted on a motorized holder and their distance is controlled by a servomotor and a rack-gear. The rotation of the motor brings the fingers close to the object. Then the voltage is applied and the fingers autonomously conform to the lateral surface of the object.

## 3.4 Peeling in electroadhesion soft grippers

Both active and passive electroadhesive soft grippers have demonstrated the ability to grasp a wide variety of objects. It has been shown, however, that in these grippers the grasping force changes over 3 orders of magnitude depending on the grasping posture. The reason behind this huge difference is the peeling angle between the EA fingers and the object. In [27] Cacucciolo et al. reported how the maximum holding force of the EA gripper described in Figure 3.4 changes from 10 mN to over 15 N by changing only the peeling angle between the fingers and the object (Figure 3.6).

In a subsequent work [26] the authors provided an analytical model to study this effect validating their predictions with experiments, showing excellent agreement.

Understanding how peeling influences the grasping forces in this gripper allowed them to optimize the design of the gripper adding an extra degree of freedom (lateral movement of the fingers) to control the grasping posture. In Figure 3.7a-b a successful pick and place of a cherry tomato (10 g) and a lime (70 g) is shown. First, the fingers are positioned tangent to the lateral surface of the objects. Then the voltage is applied and the fingers autonomously wrap around the object creating a large contact area.



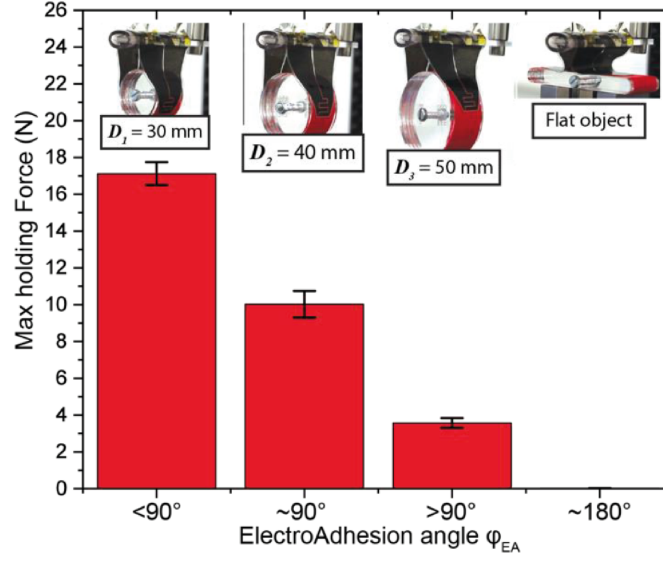


**Figure 3.6:** Force vs displacement test of the soft gripper developed in [105]. (Reproduced from [27]). Maximum holding force decreases with high peeling angles.

Then the robot moves vertically to pick the objects. To achieve the release the robot arm is moved again downwards and the fingers are opened by the servomotor, creating a sufficiently large peeling angle ( $\alpha > 30^\circ$ ) which leads to a successful and fast release. Figure 3.7c shows an attempted grasping with an high peeling angle ( $\alpha > 30^\circ$ ). As expected in this configuration the holding forces are much lower, resulting in a failed grasping. In Figure 3.7d, instead, the peeling angle is kept to zero, resulting in a successful pick and release of a mango (600 g).

Although the additional degree of freedom allows the gripper to successfully grasp a wide variety of objects of different shapes and sizes it still requires free space on the side of the objects to generate high holding forces. This constraint represents a strong limitation, especially in industrial scenarios in which the lateral space is limited and the gripper is forced to grasp the objects directly from the top.

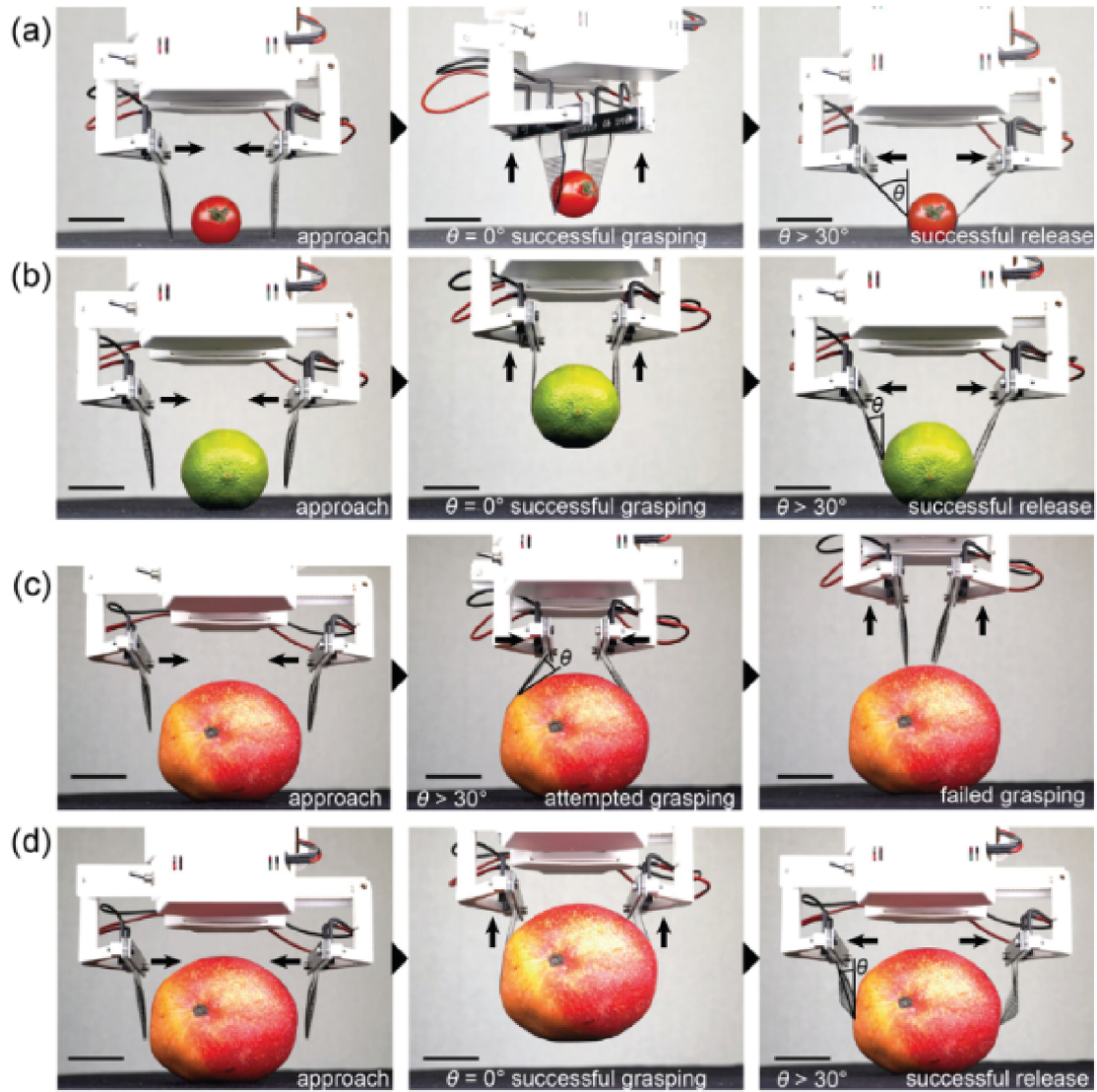


**Figure 3.7:** Pick and place of fruit and vegetables with an electroadhesive soft gripper (Reproduced from [26]). A successful grasp strongly depends on the grasping posture.

### **3.5 Layer jamming in electroadhesion soft grippers**

As discussed in the previous sections, the paradigm shift between soft and rigid materials, dramatically enhanced the performance of electroadhesive grippers. However, the extreme softness of the gripper's fingers has introduced two main challenges: i) peeling, which is responsible for the huge variation in the maximum lifting force (over 3 orders of magnitude), limiting the versatility of the grasping posture (successful grasping is mainly achieved approaching the object from the sides), ii) high deflections when subjected to even moderate bending moments, which limits objects rotation and high-speed manipulation.

Since electroadhesion soft grippers are still in their early stages of development, possible solutions to overcome these limitations are still limited. One promising approach has been proposed by Chen et al. [32]. In this work, they integrated variable stiffness structures, based on electrostatic-induced layer jamming, into electroadhesive soft fingers. Adding variable stiffness elements allowed them to mitigate the impact of peeling by a factor of 4, showing an increase of approximately 24 %, 35 %, and 49 % on the maximum holding force on flat, curved, and convex objects, respectively. Although promising, the gripper proposed in this work is far from being able to grasp and rotate a wide variety of objects of different sizes and shapes. The main problem is that soft fingers are required in the initial phase, which is the phase in which the fingers spontaneously conform to the objects when high voltage is applied, while hard fingers are required to prevent high deflections, allowing high precision during high-speed manipulation and object rotation. If the stiffness of the unjammed (soft) state is excessively high, the fingers will not conform to the object's surface, leading to a failed grasp. Therefore, to effectively integrate electrostatic-induced layer jamming systems into electroadhesive soft grippers it is necessary to maximize the stiffness ratio between the unjammed and jammed state, trying to keep the stiffness of the unjammed state as low as possible to ensure effective wrapping of the fingers on the objects. To solve this problem, we first need to find an answer to these two fundamental questions: - How the stiffness change of layer-jamming systems is influenced by the main design parameters, such as the number of layers, pressure between layers and coefficient of friction? - How the bending stiffness influences the ability of electroadhesion soft grippers to self-adapt to the surface of the objects?

The following Chapters seek to answer these questions. This would not only contribute to a better understanding of the underlying mechanics of these systems



### **Chapter3. Electroadhesion based soft gripper**

---

but would also provide a design tool to help researchers develop EA soft grippers with extended and improved capabilities.

# Chapter 4

## Layer jamming: Modeling and experimental validation

In this Chapter, the complex intrinsic mechanics of layer jamming systems is deeply investigated. Analytical models and finite element methods are presented and then validated with experiments. In particular, this study was motivated by the desire to answer the following fundamental questions:

- 1) Can we analytically predict the behavior of multi-layer jamming structures after the first (purely elastic) deformation phase?
- 2) How does the slip between the layers propagate inside a multi-layer jamming structure?
- 3) How the propagation of slip is related to the gradual decrease in stiffness in the partial-slip phase?
- 4) Does the overhanging length outside the supports influences the bending stiffness of the structures in a three-point bending test?

---

This Chapter has been adapted from the following articles:

[28] Fabio Caruso, Giacomo Mantriota, Luciano Afferrante, and Giulio Reina. A theoretical model for multi-layer jamming systems. *Mechanism and Machine Theory*, 172:104788, 2022

[30] Fabio Caruso, Giacomo Mantriota, and Giulio Reina. An analytical model for cantilever layer-jamming structures. In *The International Conference of IFToMM ITALY*, pages 193–200. Springer, 2022

[29] Fabio Caruso, Giacomo Mantriota, Vincenzo Moramarco, and Giulio Reina. Layer jamming: Modeling and experimental validation. *International Journal of Mechanical Sciences*, 251:108325, 2023

### 4.1 Introduction

As partially described in Chapter 1 and Chapter 2, in the last two decades, researchers started to design robots using compliant materials giving life to a new exciting field called Soft robotics [129, 78, 35]. This shift came from the desire to overcome the limitations of hard robots to safely interact with humans and to adapt autonomously to unstructured environments [91, 98, 73]. However, building robots with soft materials led to new and interesting challenges [72, 122, 95].

One of them is the ability to control and tune the stiffness of the soft structures [79, 123, 131]. This is particularly important in applications that require both compliance and the ability to withstand high forces, such as minimally invasive surgery [20, 97, 36], wearable haptics [133, 100], soft grippers [104, 128, 125, 135] and smart fabrics [127, 71, 103].

As described in Chapter 2, depending on the specific application, researchers came up with different techniques to achieve stiffness modulation, including thermal [116, 15], magnetic [37], electric [124] and pressure-induced (jamming [42]) stimulation. Among these techniques, jamming-based systems are usually preferred for their easy fabrication process and fast and reversible transition between soft and rigid states with very limited volume variation.

The jamming phenomenon generally consists of granules [52, 60], fibers [130, 59, 24, 90] or layers [34, 77] confined in a thin airtight membrane connected to a vacuum source. When vacuum is introduced inside the membrane frictional coupling increases, resulting in a dramatic change in stiffness (Figure 4.1a). This simple yet effective technique has proven to be useful in several applications. In Chapter 2, in subsection 2.3.1, a more detailed overview of the three main jamming approaches is provided, with a direct comparison of the systems' performance and different behaviors upon loading. In this Chapter, instead, only layer jamming systems will be analyzed. One of the first applications of this concept is represented by the snake-like manipulator developed by Kim et al. [68, 67] in which thin layers are assembled into a helical pattern to maximize stiffness change between jammed and unjammed states. Ou et al. [87] introduced layer jamming to develop dynamic haptic interfaces with tunable stiffness capabilities.

Inspired by these preliminary works, researchers started to explore the advantages of layer jamming in a wide variety of soft robotic applications. Several works employed layer jamming to increase the performance of soft grippers [132, 41, 126]. The low stiffness in the rest state allows the fingers to conform to the shape of the object

being grasped, while the high stiffness upon activation ensures high holding forces [47, 46, 38]. Layer jamming has been also proposed in soft controllable dampers [9] and wearable orthosis [58, 84]. Choi et al. [33] designed a soft wearable linear break in which the breaking force is controlled by the vacuum pressure applied to the layers.

Following the same principle, Narang et al. [85] demonstrated that layer jamming structures can be used to tune the impact response of aerial robots, while Wanasinghe et al. [121] integrated them in soft gloves as hand tremor suppressors.

Although the increasing interest, few studies tried to develop analytical models to understand the mechanical behavior of these structures. The mechanics of multi-layer structures is not new and has been extensively studied for predicting the behavior of laminate composites [101]. Analytical models [99] and numerical simulations [50] have been developed to predict both mechanical properties and interlaminar failure. However, these models are typically quite complex. They are based on higher order shear deformation theory to account for stresses at the interfaces caused by the variations of internal properties of the layers. While the complexity of these models is essential to accurately predict the behavior of laminate composites, they are overly complex for layer jamming systems in which the behavior is simply controlled by friction and vacuum pressure.

Narang and colleagues [86] were the first to provide an analytical model, based on the Euler Bernoulli beam theory, to predict the change in stiffness due to slip propagation in a two-layer cantilever jamming structure subjected to a distributed load. In the same work [86] they developed finite element models to extend the predictions to many-layer jamming structures. These models were then validated with experiments showing excellent agreement.

Subsequent research extended these models introducing a 3D FE-based numerical tool that predicts the mechanical response of layer jamming structures subjected to arbitrary loading and boundary conditions [119].

Although these works represent a significant step forward in the effort of understanding layer jamming systems, they have not yet provided analytical models for multi-layer jamming systems beyond the initial deformation phase. The main problem of finite element models is that the computational time increases with the number of layers. Therefore, for jamming structures with many layers, the computational time may become prohibitive and can significantly delay the design process.

To overcome this limitation, in this thesis is proposed for the first time an analytical model extended to a structure with an arbitrary number of layers [28, 29]. The model demonstrates that the typical nonlinear behavior of these structures can

be well described with a piecewise linear approximation between subsequent slips. It also predicts how the slip propagates inside the structure and how these slips can be related to the gradual stiffness change. Analytical predictions were then compared with finite element simulation, both in a three-point bending and cantilever configuration [30], showing very good agreement. Experimental tests were also conducted to validate the proposed approach as well as finite element simulations to confirm the prediction about slip propagation inside the structure. The model was able to predict with great accuracy the effect of the number of layers, vacuum pressure, friction coefficient, and energy dissipated by friction in a load-unload cycle, demonstrating that the complex intrinsic mechanics of these systems can be well approximated by a 2D analytical model.

### 4.2 Analytical formulation

Consider a layer-jamming structure with an arbitrary number of layers  $n$ , subjected to a 3-point bending test. Let the structure be subjected to a vacuum pressure  $p$ . As the load  $F$  increases, the structure experiences three different deformation phases (Figure 4.1b-c):

- 1) A pre-slip phase, in which the longitudinal shear stress at the interfaces between layers remains below the static friction limit ( $\mu P$ ).
- 2) A partial-slip phase, in which the structure can be considered divided in two parts. An external cohesive region, where the longitudinal shear stress at the interfaces between two adjacent layers remains below the friction limit, and an internal slip region where the longitudinal shear stress at the interfaces equals the maximum admissible shear stress. As a result, layers in the internal region are in slip while those of the external region remains in stick regime.
- 3) A full-slip phase, in which all the layers are in slip. Depending on the deformation phase, the stiffness of the structure will be different.

To describe this behavior, we assume that the layers height is considerably smaller than its length and width, the structure undergoes small deflections, and the deformations are restricted to the  $xy$  plane. Therefore, we model the layers using the Euler-Bernoulli beam theory, as this is a commonly adopted model for this problem [86, 7]. Also, we neglect edge effects and interactions between layers and the membrane and we assume that the coefficient of friction  $\mu$  and the pressure  $p$  are constant along the interfaces. Under this assumption, the relationship between the deflection at the center of the structure  $w$  and the applied load  $F$  is given by the well known

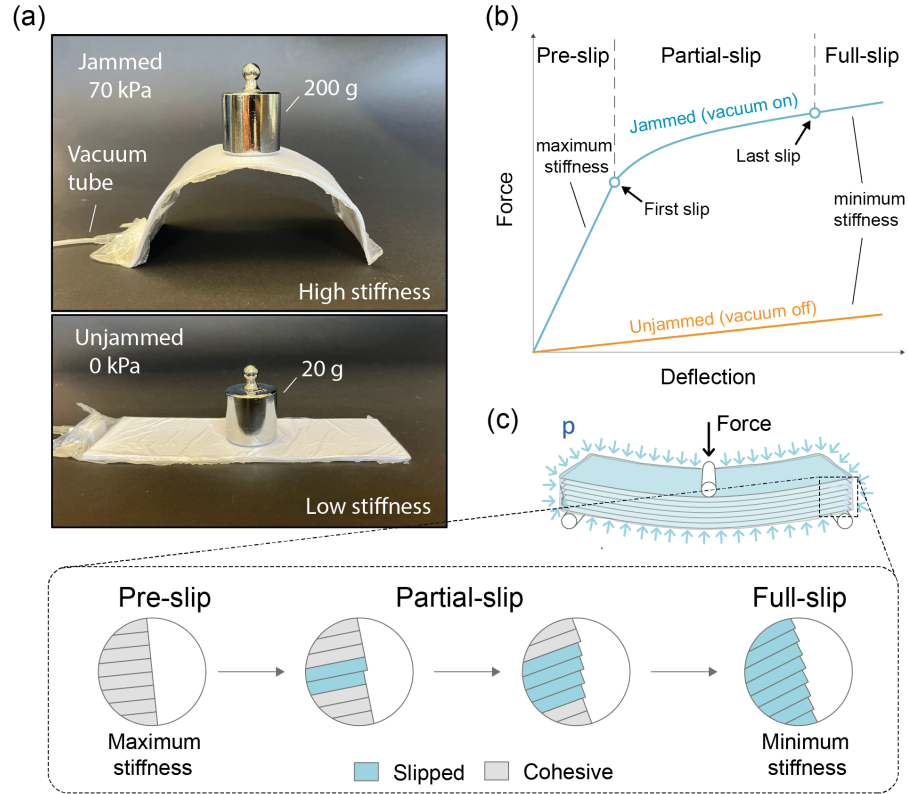


**Figure 4.1:** Stiffness change and slip propagation in layer jamming systems (reported from [29]). a) Visualization of the dramatic change in stiffness when the structure is jammed (70 kPa) and unjammed (0 kPa). b) Fundamental behavior of layer jamming structures subjected to three-point bending tests. c) Schematic representation of slip propagation. In the pre-slip phase the shear stress at each interface remains below the static friction limit, the stiffness is maximum and the system behaves like a single beam. Then as the external load increases, the structure enters in the partial-slip phase. Here, slip starts from the central interface and propagates outward. The behavior becomes nonlinear and the stiffness decreases. In the last phase (Full-slip) all the layers are in slip and the stiffness is minimum.

formula

$$w = \frac{FL^3}{48EI} \quad (4.1)$$

where  $E$  is the Young's modulus of the layers,  $I$  is the second moment of area and  $L$  is the length of the structure. During the pre-slip and full-slip phases, the values of  $I$  are already known in literature and can be expressed by

$$I_{pre-slip} = \frac{b(nh)^3}{12} \quad (4.2)$$

$$I_{full-slip} = \frac{nbh^3}{12} \quad (4.3)$$

where  $b$  and  $h$  are the width and the height of a single layer and  $n$  is the total number of layers. However, to the best of the author's knowledge, no studies investigated the computation of the bending stiffness during the partial-slip phase and the critical transverse loads at which slip occurs.

In order to facilitate the understanding of the model, in the following subsections we first derive the governing equations for a structure with only 4 layers and then we provide a general formulation that can be applied to a structure with an arbitrary number of layers.

### 4.2.1 Four Layers

Consider the four-layer jamming structure shown in Figure 4.2. Due to the load and geometry symmetry, only one-half of the structure is needed to investigate the problem. As already mentioned, in the pre-slip phase, the whole structure behaves as a single beam. Therefore, the relationship between the resultant moment at each cross-section and the axial stress distribution is given by the Navier equation,

$$\sigma(x, y) = \frac{y M(x)}{I_{pre-slip}} \quad (4.4)$$

where  $M(x) = F(L/2-x)/2$  is the resultant moment and  $y$  is the distance from the neutral axis. As the load  $F$  increases the longitudinal shear stress at the interfaces will rise as a consequence. According to the Jourasky formula applied to rectangular cross-sections, the maximum shear stress occurs at the central interface and is given by

$$\tau_{slip} = \frac{3 F_0}{2 A} \quad (4.5)$$

## Chapter 4. Layer jamming: Modeling and experimental validation

---

where  $F_0$  is the maximum load before slip occurs and  $A = 4bh$  is the cross-section area. As the maximum possible shear stress at the interfaces is equal to the frictional limit ( $\mu p$ ), the value of  $F_0$  can be expressed as

$$F_0 = \frac{2\mu p A}{3} \quad (4.6)$$

The corresponding maximum value of the axial stress  $\sigma_0$  occurs at  $x = 0$ ,  $y = 2h$   $F = 2F_0$ , i.e.,

$$\sigma_0 = \sigma(0, 2h) = \frac{3F_0 L}{16bh^2} \quad (4.7)$$

Equation (4.5) can be also expressed as a function of  $\sigma_0$  indeed, from the static equilibrium of the upper half of the beam along the x-axis we obtain

$$\tau_{slip} = \mu p = \frac{2\sigma_0 h}{L} \quad (4.8)$$

When the transverse load reaches the critical value  $F_0$ , the interface between layers 2 and 3 starts to slip. For successive load enhancements, we can assume that the structure is divided into two beams that experience the same deflection and are subjected to the same stress state. The axial stress distribution, in this case, could be seen as the sum of the distribution in the pre-slip phase, caused by  $F_0$ , and the distribution generated by an additional force, as shown in Figure 4.2a. As the transverse load increases, the longitudinal shear stress between the interfaces that are still in full stick will grow. In order to find the value of the additional force  $F_1$  that causes slip, we need to derive an expression for the longitudinal shear stress at the interfaces between layers 1-2 and 3-4 as a function of  $\sigma_0$  and  $\sigma_1$ . Solving the static equilibrium of layers 1 and 4 along the longitudinal direction, we obtain

$$\tau_{1-2} = \tau_{3-4} = \frac{h}{L} (\sigma_0 + 2\sigma_1) \quad (4.9)$$

Equating 4.8 and 4.9, and solving for  $\sigma_1$ , we get  $\sigma_1 = \sigma_0/2$  and hence in terms of the external transverse loads

$$F_1 = \frac{F_0}{4} \quad (4.10)$$

Table 4.1 and Figure 4.2b summarize the relationships between the applied load  $F$ , the second moment of area  $I$  and the deflection at the center of the structure  $w$ , during the three deformation phases.



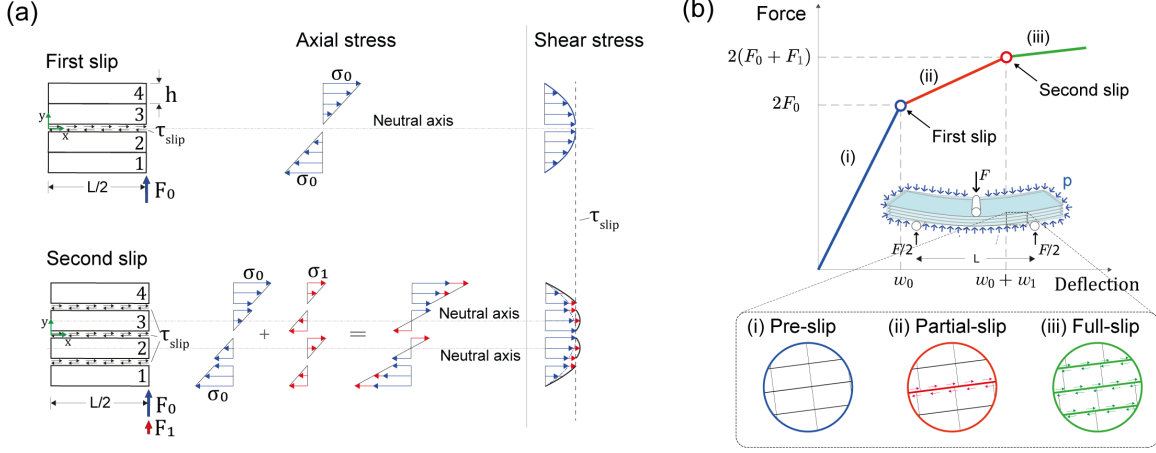


**Figure 4.2:** Analytical model of four-layer jamming structures. (a) Schematic representation of the axial and shear stress distribution. When the transverse load is equal to  $F_0$  the longitudinal shear stress at the central interface reaches the frictional limit ( $\tau_{slip} = \mu p$ ) and layers 2 and 3 start to slip. As the external load is further increased by the additional load  $F_1$ ,  $\tau_{slip}$  is reached also at the interface between layers 1-2 and 3-4 and all the layers enter in slip. (b) Qualitative representation of the change in stiffness and slip propagation during a three-point bending test in all the three deformation phases

	Pre-slip	Partial-slip	Full-slip
$F$	$F < 2F_0$	$2F_0 < F < 2(F_1 + F_0)$	$F > 2(F_0 + F_1)$
$I$	$I_{pre-slip} = \frac{b(4h)^3}{12}$	$I_{partial-slip} = \frac{2b(2h)^3}{12}$	$I_{full-slip} = \frac{4bh^3}{12}$
$w$	$w = \frac{FL^3}{48EI_{pre-slip}}$	$w = \frac{(F-2F_0)L^3}{48EI_{partial-slip}}$	$w = \frac{(F-2(F_0+F_1))L^3}{48EI_{full-slip}}$

Table 4.1: Relationships between the applied load  $F$ , the second moment of area  $I$  and the deflection at the center of the structure  $w$ , during the three deformation phases of a four-layer jamming structure

### 4.2.2 Arbitrary number of layers

Consider a more general case, in which the number of layers  $n$  is an arbitrary even number. Due to the symmetry of the problem after the first slip, we can further simplify the formulation considering only the upper half of the structure. Compared to the previous case, there are multiple interfaces at which the slip could occur. In order to determine the first interface that reaches the frictional limit we need to calculate the longitudinal shear stress  $\tau(0, y)$  at the cross-section  $x=0$  by solving the static equilibrium along the longitudinal direction for a generic portion of the structure of length  $L/2$  and height  $H-y$ , which returns

$$\tau(0, y) = \frac{\sigma_0 + 2\sigma_1 y/H + \sigma_0 y/H}{L} H(1 - y/H) \quad (4.11)$$

where  $H$  is the height of upper half of the structure,  $L$  is the length of the entire structure and  $\sigma_0$  and  $\sigma_1$  are the axial stresses caused by the transverse loads  $F_0$  and  $F_1$  (Figure 4.3). Now, equating (4.11) to the maximum value of the longitudinal shear stress ( $\tau_{slip} = \sigma_0 H/L$ ) and solving for  $y/H$ , we obtain

$$\frac{\bar{y}}{H} = \frac{\frac{2\sigma_1}{\sigma_0}}{1 + \frac{2\sigma_1}{\sigma_0}} \quad (4.12)$$

where  $\bar{y}$  is the height at which the shear stress of slip  $\tau_{slip}$  is reached. Figure 4.3b, shows  $\bar{y}$  is a monotonically increasing function of  $\sigma_1/\sigma_0$ , so demonstrating that, the first interface that enters in slip is the one nearest to the center of the structure. Therefore, during the transition from pre-slip to full-slip, the structure can be described as divided in two parts. A cohesive region, in which the layers are attached to each other, and a slip region in which layers are detached (Figure 4.4). Following the same procedure of the four-layer structure, we compute the value of the maximum axial stress  $\sigma_i$  and the corresponding additional transverse force  $F_i$  that causes slip at the  $i$ th interface. Generalizing Eq.4.9 we define an expression for  $\tau(i)$  which is the longitudinal shear stress at the  $i$ th interface

$$\tau(i) = \frac{\sigma_{top}(i) + \sigma_{int}(i)}{L} (H - ih) \quad (4.13)$$

where  $\sigma_{int}(i)$  and  $\sigma_{top}(i)$  are

$$\sigma_{int}(i) = \sigma_{bot}(i) + m(i)h \quad (4.14)$$

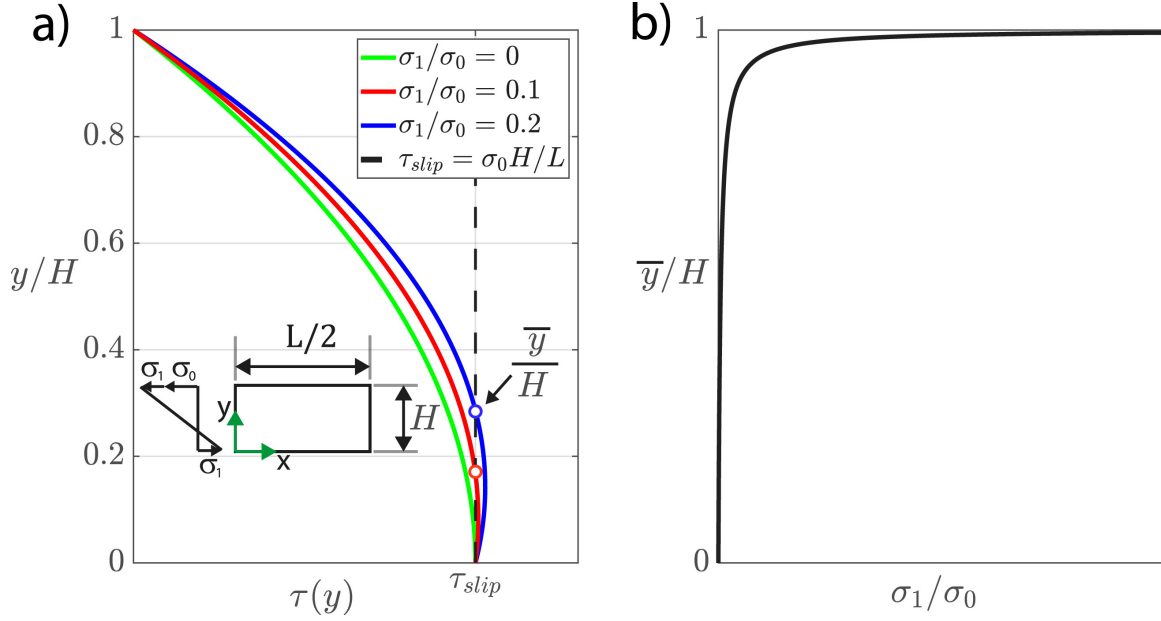


**Figure 4.3:** a) Longitudinal shear stress along the cross-section of the upper half of a multi-layer jamming structure at  $x = 0$ , for three different values of  $\sigma_1/\sigma_0$ . b) Plot of equation (4.12)

$$\sigma_{top}(i) = -\sigma_{top}(i-1) - \sigma_i \quad (4.15)$$

and  $m(i)$  is given by

$$m(i) = \frac{\sigma_{top}(i) - \sigma_{bot}(i)}{H - (i-1)h} \quad (4.16)$$

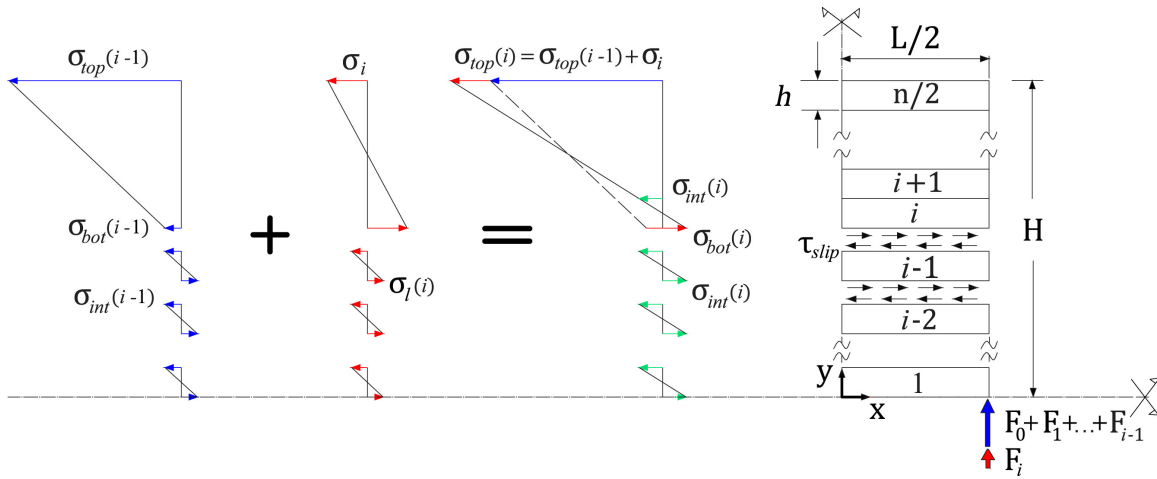


**Figure 4.4:** Schematic representation of the transverse loads, axial and longitudinal shear stresses in the partial-slip phase of a multi-layer jamming structure.

## Chapter4. Layer jamming: Modeling and experimental validation

---

Now, equating 4.13 to the maximum value of the longitudinal shear stress ( $\tau_{slip} = \sigma_0 H/L$ ) and solving for  $\sigma_i$ , we obtain

$$\sigma_i = \frac{(H - h(i - 1)) \left( \frac{H\sigma_0}{2} + (H - h i) \left( \frac{\sigma_{int}(i-1)}{2} + \frac{\sigma_{top}(i-1)}{2} - \frac{h(\sigma_{int}(i-1) - \sigma_{top}(i-1))}{2(H - h(i-1))} \right) \right)}{h(H - h i)} \quad (4.17)$$

which is the value of the additional axial stress experienced by the layers in the cohesive region, which causes slip at the  $i$ th interface. The expression of the corresponding additional transverse force  $F_i$  is given by

$$F_i = \frac{2\sigma_i(H - h(i - 1))^2 + h^2\sigma_l(i)(i - 1)}{6L} \quad i = 1, \dots, n/2 - 1 \quad (4.18)$$

where  $\sigma_l$  is the additional axial stress experienced by the layers that are already in slip

$$\sigma_l(i) = \sigma_{int}(i) - \sigma_{int}(i - 1) \quad (4.19)$$

The general expression of the second moment of area  $I$  during the partial-slip phase can be computed as follows

$$I_{partial-slip}(i) = 2 \frac{b[(n/2 + 1 - i)h]^3}{12} + \frac{2bh^3}{12}(i - 1) \quad i = 1, \dots, n/2 - 1 \quad (4.20)$$

where  $b$  and  $h$  are the width and height of a single layer and  $n$  is the total number of layers. Substituting equations 4.18 and 4.20 into 4.1 we obtain the additional deflection  $w_i$  caused by the additional force  $2F_i$

$$w_i = \frac{2F_i L^3}{48EI_{partial-slip}(i)} \quad i = 1, \dots, n/2 - 1 \quad (4.21)$$

Now, extending (4.8) to the case of  $n$  layers ( $\sigma_0 = \mu p L/(nh/2)$ ), writing  $\sigma_{top}$ ,  $\sigma_{bot}$ ,  $\sigma_{int}$  and  $\sigma_l$  in terms of  $\mu p$ , and substituting into equation (4.17), the formulas of the transverse forces and the corresponding deflections can be also expressed in terms of the coefficient of friction  $\mu$ , vacuum pressure  $p$ , width  $b$ , number of layers  $n$ , layers height  $h$ , Young modulus  $E$  and layers length  $L$

$$F_0 = \frac{2\mu p b h n}{3} \quad (4.22)$$

$$F_1 = \frac{\mu p b h n}{3(n - 2)} \quad (4.23)$$

$$F_2 = \frac{2\mu p b h (n^2 - 6n + 12)}{3(n^2 - 6n + 8)} \quad (4.24)$$

$$F_i = \frac{2\mu p b h (n^3 - 6(i-1)n^2 + 12(i-1)^2 n - 8(i^3 - 3i^2 + 2i))}{3(n^3 - 6(i-1)n^2 + (12(i-1)^2 - 4)n - 8(i^3 - 3i^2 + 2i))} \quad i = 3, \dots, n/2-1 \quad (4.25)$$

$$w_0 = \frac{\mu p L^3}{3 E h^2 n^2} \quad (4.26)$$

$$w_1 = \frac{2\mu p L^3}{3 E h^2 n^2 (n-2)} \quad (4.27)$$

$$w_2 = \frac{4\mu p L^3}{3 E h^2 n (n^2 - 6n + 8)} \quad (4.28)$$

$$w_i = \frac{4\mu p L^3}{3 E h^2 (n^3 - 6(i-1)n^2 + (12(i-1)^2 - 4)n - 8(i^3 - 3i^2 + 2i))} \quad i = 3, \dots, n/2-1 \quad (4.29)$$

Table 4.2 summarizes the relationships between the applied load  $F$ , the second moment of area  $I$ , and the deflection at the center of the structure  $w$ , during the three deformation phases of a  $n$ -layer-jamming structure. Figure 4.4 show a schematic representation of the loads and stresses experienced by the structure in the partial-slip phase. In particular, in blue are indicated both the transverse load and the distribution of the axial stresses causing slip between layers  $i$  and  $i-1$ , while in red are indicated the additional transverse force and the distribution of the additional axial stresses producing slip between layers  $i$  and  $i+1$ .

	Pre-slip	Partial-slip	Full-slip
$F$	$F < 2F_0$	$2F_0 < F < 2(F_0 + \sum_{i=1}^{n/2-1} F_i)$	$F > 2(F_0 + \sum_{i=1}^{n/2-1} F_i)$
$I$	$I_{pre-slip} = \frac{b(nh)^3}{12}$	$I_{partial-slip}(i) = 2 \frac{b[(n/2+1-i)h]^3}{12} + \frac{2b(i-1)h^3}{12}$	$I_{full-slip} = \frac{nbh^3}{12}$
$w$	$w = \frac{FL^3}{48EI_{pre-slip}}$	$w = \frac{F-2(\sum_{i=0}^{i-1} F_i)L^3}{48EI_{partial-slip}(i)}$	$w = \frac{(F-2(\sum_{i=0}^{n/2-1} F_i))L^3}{48EI_{full-slip}}$

Table 4.2: Relationships between the applied load  $F$ , the second moment of area  $I$  and the deflection at the center of the structure  $w$ , during the three deformation phases of a multi-layer jamming structure

### 4.2.3 Model refinement including the effect of the overhangs

The model presented in the previous subsection computes the deflections at the center of the structure assuming that the structure can be treated as a typical simply supported beam using the well-known formula reported in 4.1. However, as we will see in detail in the next section, this approximation is valid only in the Pre-slip phase,

## Chapter4. Layer jamming: Modeling and experimental validation

---

where the structure behaves like a cohesive single beam and the overhanging portion of the beam outside the supports does not influence the deformation and therefore is usually neglected. In layer-jamming structures, instead, this condition is no longer true in the presence of slip.

Indeed, due to the discontinuity in the shear stress caused by the concentrated load at the support, the structure can be divided in two regions: an internal region, between the supports, in which the transversal load is constant ( $V = F/2$ ); an external region, outside the supports, in which the transversal load is zero ( $V=0$ ). For this reason, as the external load increases, the portion of the interfaces between the supports will start to slip (when the longitudinal shear stress equals the frictional limit  $\mu p$ ) while the external region will remain cohesive. In reality, sliding propagates also in the external regions Figure 4.13, although to a lesser extent.

Therefore, to keep the complexity of the model at an acceptable level, the interface between these two adjacent regions is approximated to a clamped boundary condition. Under this hypothesis, the additional deflections after the first slip are computed using the Euler-Bernoulli formula for a clamped-clamped beam, that is

$$w = \frac{FL^3}{192EI} \quad (4.30)$$

All the steps to derive the critical transverse loads are identical to those described in the previous sections, the only difference is the change in the boundary conditions from the simply supported beam, in the pre-slip phase, to the clamped-clamped boundary condition, in the partial-slip and full-slip phase. The following are the modified equations that take into account the effects of the overhangs

$$F_0 = \frac{2\mu p b h n}{3} \quad (4.31)$$

$$F_1 = \frac{\mu p b h n}{3(n-2)} \quad (4.32)$$

$$F_2 = \frac{2\mu p b h (n^2 - 6n + 12)}{3(n^2 - 6n + 8)} \quad (4.33)$$

$$F_i = \frac{2\mu p b h (n^3 - 6(i-1)n^2 + 12(i-1)^2n - 8(i^3 - 3i^2 + 2i))}{3(n^3 - 6(i-1)n^2 + (12(i-1)^2 - 4)n - 8(i^3 - 3i^2 + 2i))} \quad i = 3, \dots, n/2-1 \quad (4.34)$$

$$w_0 = \frac{\mu p L^3}{3E h^2 n^2} \quad (4.35)$$

$$w_1 = \frac{\mu p L^3}{6 E h^2 n^2 (n - 2)} \quad (4.36)$$

$$w_2 = \frac{\mu p L^3}{6 E h^2 n (n^2 - 6 n + 8)} \quad (4.37)$$

$$w_i = \frac{\mu p L^3}{3 E h^2 (n^3 - 6 (i - 1) n^2 + (12 (i - 1)^2 - 4) n - 8 (i^3 - 3 i^2 + 2 i))} \quad i = 3, \dots, n/2 - 1 \quad (4.38)$$

#### 4.2.4 Cantilever configuration

The same approach used for the case of the simply supported configuration can be used to describe the behavior of cantilever jamming structures. In this case, the deflection at the free end is given by the well-known formula

$$w = \frac{FL^3}{3EI} \quad (4.39)$$

Since the derivation of the transverse loads and the corresponding deflections is identical to the case of the simply supported beam, here are reported only the general formulas for a cantilever layer jamming structures with an arbitrary number of layers

$$F_0 = \frac{2 \mu p b h n}{3} \quad (4.40)$$

$$F_1 = \frac{\mu p b h n}{3 (n - 2)} \quad (4.41)$$

$$F_2 = \frac{2 \mu p b h (n^2 - 6 n + 12)}{3 (n^2 - 6 n + 8)} \quad (4.42)$$

$$F_i = \frac{2 \mu p b h (n^3 - 6 (i - 1) n^2 + 12 (i - 1)^2 n - 8 (i^3 - 3 i^2 + 2 i))}{3 (n^3 - 6 (i - 1) n^2 + (12 (i - 1)^2 - 4) n - 8 (i^3 - 3 i^2 + 2 i))} \quad i = 3, \dots, n/2 - 1 \quad (4.43)$$

$$w_0 = \frac{8 \mu p L^3}{3 E h^2 n^2} \quad (4.44)$$

$$w_1 = \frac{16 \mu p L^3}{3 E h^2 n^2 (n - 2)} \quad (4.45)$$

$$w_2 = \frac{32 \mu p L^3}{3 E h^2 n (n^2 - 6 n + 8)} \quad (4.46)$$

$$w_i = \frac{32 \mu p L^3}{3 E h^2 (n^3 - 6 (i - 1) n^2 + (12 (i - 1)^2 - 4) n - 8 (i^3 - 3 i^2 + 2 i))} \quad i = 3, \dots, n/2 - 1 \quad (4.47)$$

## Chapter4. Layer jamming: Modeling and experimental validation

To facilitate the understanding, Figure 4.5 shows the schematic representation of axial and shear stress distribution in the case of a four layer-jamming cantilever structure, whereas Figure 4.6 illustrates slip propagation between layers inside the structure, during the three main deformation phases.

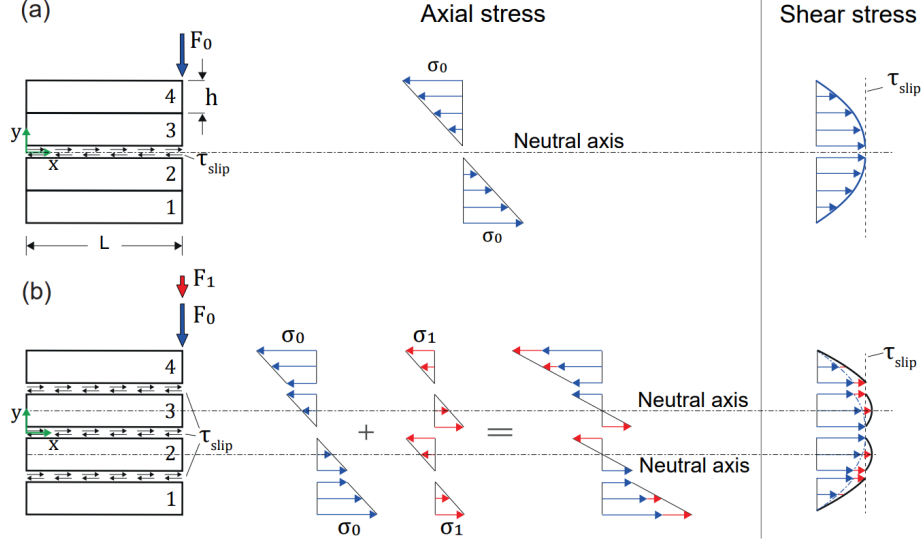


**Figure 4.5:** Representation of the axial and shear stress experienced by a cantilever structure with four layers (reproduced from [30]). a)  $F_0$  is the critical force at which the structure shift from the pre-slip to the partial-slip phase. b)  $F_1$ , instead, is the additional load needed to shift from the partial-slip to the full-slip phase.



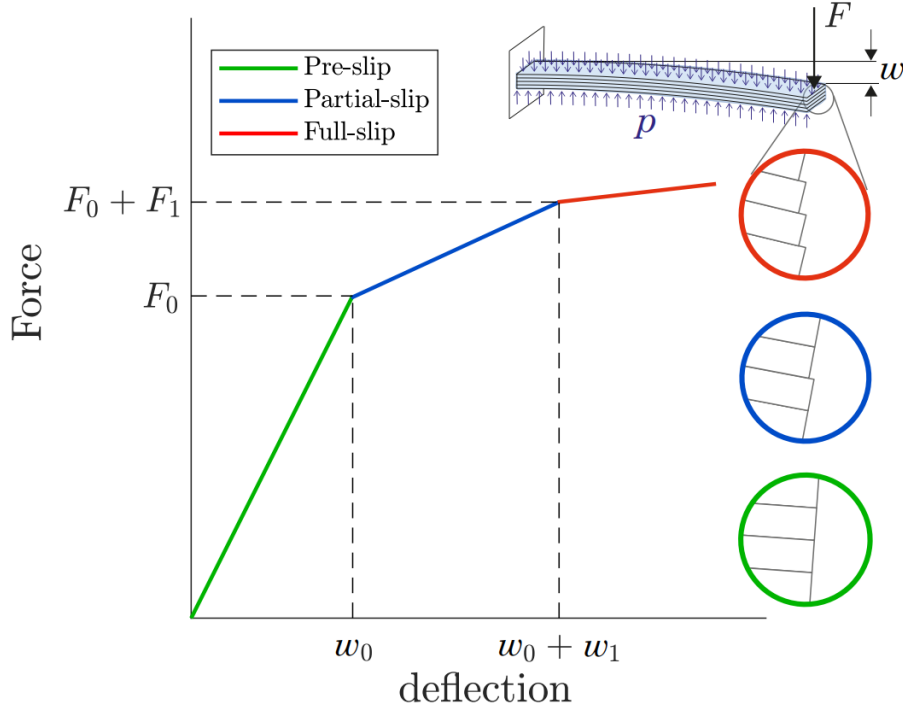


**Figure 4.6:** Qualitative representation of slip propagation experienced by a cantilever jammed structure with four layers. (reproduced from [30])

## 4.3 Materials and methods

### 4.3.1 Finite element model for small deflections

To validate the analytical model proposed in the previous section, a finite element model was developed. The simulations were performed using the commercial software ANSYS. Since all the loads and the corresponding deflections occur in the x-y plane, each layer was modeled with 2-D plane-strain elements (PLANE182). Each layer was meshed using a square four node plane strain element with a side length equals to half of the layer height, according to Narang et al. [86]. The interaction between two adjacent layers was modeled using the elements CONTA172 and TARGE169 with a constant coefficient of friction based on Coulumb's Law. The vacuum pressure was applied through a uniform distributed load acting on all the external surfaces of the structure. Due to the symmetry of the problem, the computational cost of the simulations was reduced considering only one half of the structure. For this reason, a zero horizontal displacement boundary condition was applied at the nodes on the left edge of the model. Furthermore, vertical displacement was constrained at the right edge of the structure at the central interface. Finally, an incremental downward

vertical displacement was applied at the first node of the top surface. Notice that the effect of the overhanging length outside the support was not considered in this set of simulations. Therefore in the finite element model, the length of the structure outside the support was set to zero. In the next section, the effect of the overhanging length on the bending stiffness of the structure will be discussed and incorporated into the finite element models.

### 4.3.2 Effect of the number of layers

In order to study the effect of the number of layers on the bending stiffness of the structure, five simulations were carried out varying the number of layers  $n$  from 4 to 20 in increments of four. In all simulations, geometric and material properties were chosen in accordance with the typical range of values used in layer-jamming applications [42], that are: height  $h = 0.5$  [mm], length  $L = 100$  [mm], width  $b = 50$  [mm], Young's modulus  $E = 6$  [GPa], Poisson's ratio  $\nu = 0.156$ . In addition, a vacuum pressure  $p = 50$  [kPa] was applied on the external surfaces and the coefficient of the friction was set to  $\mu = 0.5$ . Notice that in the analytical model the elastic modulus  $E$  was replaced by the plane strain Young's modulus  $\bar{E} = \frac{E}{1-\nu^2}$  as  $b \gg h$ . As shown in Figure 4.7, the predictions of our analytical model are in good agreement with the results obtained by the finite element simulations. Red dots identify the transition loads  $F_i$  and the corresponding deflections  $w_i$ , where the bending stiffness changes due to slip occurring at the  $i$ th interface. As expected, in the pre-slip phase, the bending stiffness of the structure is proportional to  $n^3$  according to 4.2. In addition, the force  $F_0$  and the deflection  $w_0$ , at which the first slip occurs, are proportional to  $n$  and  $1/n^2$ , respectively. These dependencies are already known in literature and have been confirmed both from experiments and finite element simulations [86]. As the load  $F$  increases, the structure enters in the partial-slip phase and the force versus deflection relationship becomes non-linear. In our model we capture this behavior with a piece-wise linear approximation, in which the gradual change in stiffness and the transition loads at which this change occurs are described by Eqs. 4.20 and 4.18, respectively. Thanks to this approach, we are also able to predict the last transition load at which the structure enters in the full-slip phase. Its expression is given by

$$F_{full-slip} = 2 \left( F_0 + \sum_{i=1}^{n/2-1} F_i \right) \quad (4.48)$$

where  $F_0$  and  $F_i$  are given by Eqs. 4.22 and 4.18, respectively. As shown in Figure 4.7, the value of  $F_{full-slip}$  scales with  $n$ . In addition, it is interesting to observe that the deflection  $w_{full-slip}$  at which full-slip occurs does not depend on the number of layers. The analytical expression of  $w_{full-slip}$  is given by

$$w_{full-slip} = w_0 + \sum_{i=1}^{n/2-1} w_i \quad (4.49)$$

where  $w_0$  is the deflection at which the structure shifts from the pre-slip to the partial-slip phase, while  $w_i$ , given in Eq 4.21, is the additional deflection due to the additional force  $F_i$ . With reference to Figure 4.7, the difference between the slope of the last segment (full-slip phase) and that of the previous one (last stage of the partial-slip phase) reduces as the number of layers increases. As a result, the percentage variation of the bending stiffness, which is proportional to the slope of the segments, becomes negligible when the number of layers is sufficiently large. Furthermore, most of the change in bending stiffness is confined to a small range of deflections. Finally, we notice the percentage difference between the values of  $F_{full-slip}$  given by our analytical model and the corresponding values obtained by FEM simulations slightly increases with the number of layers. One of the main reasons for such an increase is probably due to the overall growth in the height of the structure. Indeed, the more the height increases the more we move away from the Euler-Bernoulli assumption  $h \ll L$ . In addition, a second source of error could be due to the stress concentration occurring near the supports and the applied load, which is observed to increase with the number of layers.

### 4.3.3 Effect of the vacuum pressure

To investigate the effect of the vacuum pressure on the bending stiffness of the structure, five simulations were performed and the vacuum pressure was varied from 20 to 100 [kPa] in increments of 20 [kPa]. The number of layers was kept constant and equals to  $n = 20$  and all the other variables were maintained equal to the previous set of simulations. Figure 4.8 shows the comparison between the analytical and numerical results. As expected, until all layers are stuck in the pre-slip phase, the bending stiffness does not depend on the vacuum pressure. However, both the first transition force  $F_0$  and the corresponding deflection  $w_0$  scale with  $p$  and, in addition,  $F_{full-slip}$  and  $w_{full-slip}$  show a proportional dependence on it.

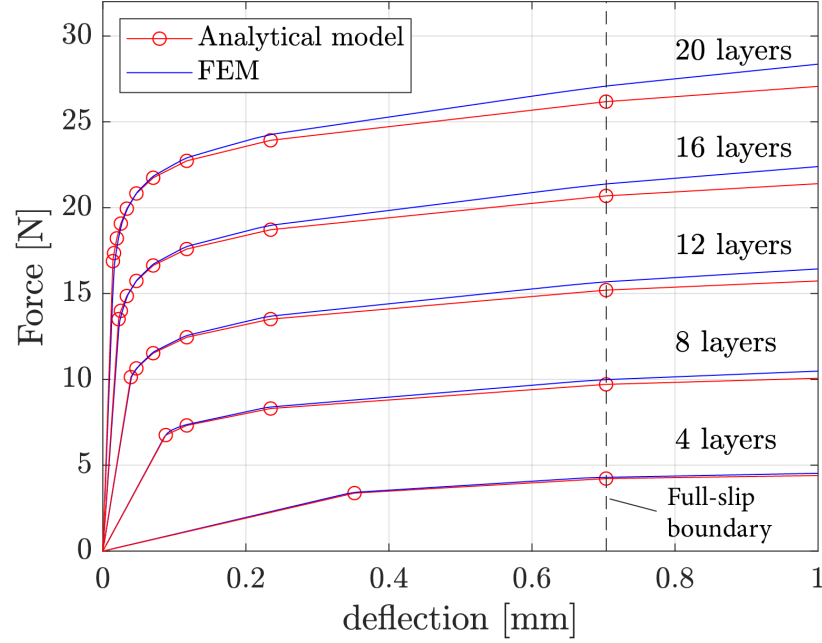


**Figure 4.7:** The force vs. deflection relation for a multi-layer jamming structure with a different number of layers (reproduced from [28]). Analytical predictions (red) are compared with FEM results (blue)

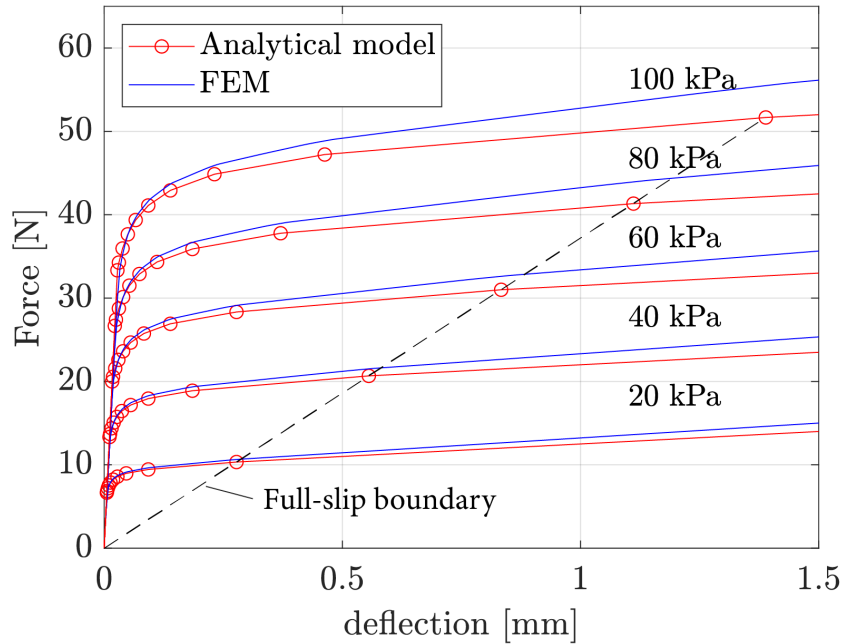


**Figure 4.8:** The force vs. deflection relation for a 20-layer jamming structure with different values of the vacuum pressure (reproduced from [28]). Analytical predictions (red) are compared with FEM results (blue).

### 4.3.4 Effect of the coefficient of friction

To investigate the effect of the coefficient of friction  $\mu$ , five simulations were performed with  $\mu$  varying from 0.2 to 0.6 in increments of 0.1. The number of layers and the vacuum pressure were kept constant and equals to  $n = 20$  and  $p = 50$  [kPa], respectively. All the other variables were maintained equal to the first set of simulations. Analytical and numerical results are compared in Figure 4.9. As expected, changing either the coefficient of friction or the vacuum pressure produces the same effect on the general behavior of the structure. As in the previous case, the slope of the curve (which is proportional to the bending stiffness) in the pre-slip phase does not depend on  $\mu$  because no interface is sliding. On the contrary, the forces of first slip  $F_0$  and full slip  $F_{full-slip}$  (and corresponding deflections) linearly increase with the friction coefficient.

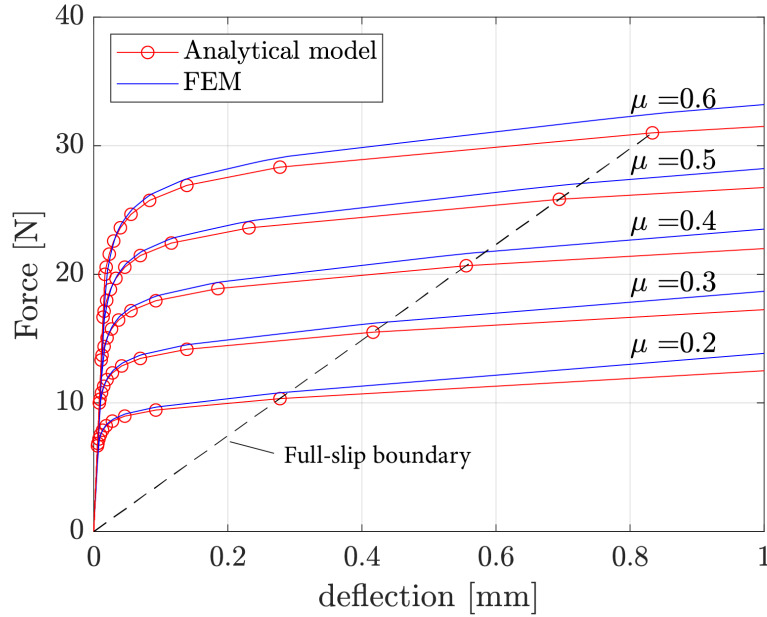


**Figure 4.9:** The force vs. deflection relation for a 20-layer jamming structure with different values of the coefficient of friction. (reproduced from [28]). Analytical predictions (red) are compared with FEM results (blue).

Figure 4.10 shows FEM results of the three deformation phases experienced by an 8-layer structure. In the pre-slip stage (Figure 4.10a) all the layers are still attached, while in the partial-slip phase (Figure 4.10b) two different regions can be observed: an inner one, in which layers are in slip, and an outer one where the layers are still in stick regime. These results confirmed the prediction of the model that slip propagates from the inner to the outer interfaces. Finally Figure (4.10c) shows that at high deflections the full-slip phase is reached with all the layers in slip.

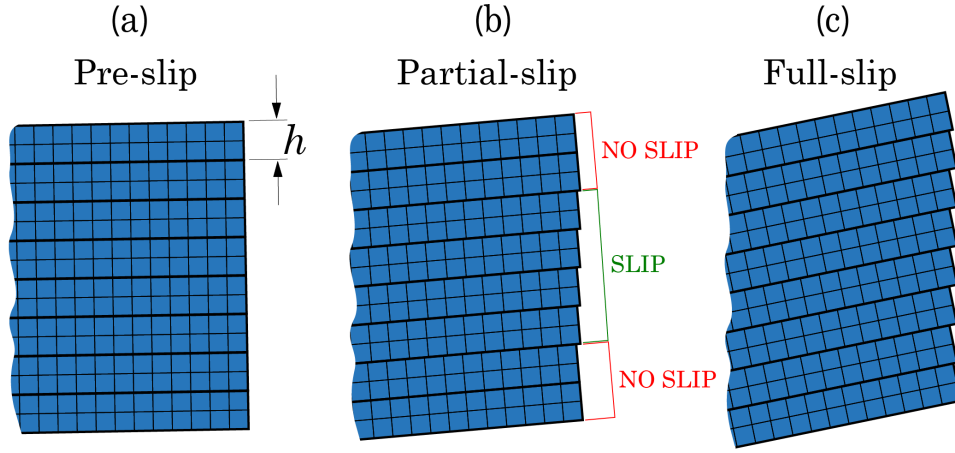


**Figure 4.10:** Deformation phases in a 8-layer structure from FEM simulations: a) pre-slip phase in which all the layers are attached, b) partial-slip phase in which the layers in the inner region are in slip (green bracket) while the layers in the outer region are still attached (red brackets). c) full-slip phase in which all the layers have slipped. For the sake of readability, only the right-end portion of the structure is shown. (reproduced from [28])

### 4.3.5 Finite element model for large deflection

In this paragraph, the finite element model developed for simulating large deflections is presented. The approach is similar to the one used for small deflection apart from the software that has been used. The software used to simulate large deflection is the commercial package ABAQUS/Standard 2017. ABAQUS was selected over ANSYS due to the more efficient contact detection algorithm employed, which is based on the penalty contact method, resulting in a significant reduction of the total computational costs of the simulations.

Each layer was discretized using four-node bilinear hybrid plane strain elements

with reduced integration (CPE4RH), with a side length equal to half of the layer height. A linear isotropic elastic material with Young's modulus and Poisson's ratio equal to those of the copy paper used in the experiments was assigned to the layers. ( $E = 1.7$  GPa and  $\nu = 0.156$ ). A standard surface-to-surface contact with penalty friction formulation was used to model the interaction between two adjacent layers. A very low value of maximum elastic slip  $5 * 10^{-5}$  was set to reduce the undesired non-physical elastic slip.

Vacuum pressure was simulated imposing a uniformly distributed load to all the outer edges of the structure. Symmetric boundary conditions were applied on the left edge of each rectangle. The support was simulated by assigning a zero vertical displacement to a node of the bottom layer 50 mm from the center of the structure.

Lastly, the deflection at the center of the structure was simulated by applying a vertical displacement at the first node of the top layer. In all the simulations, nonlinear effects due to large deflections were also taken into account (NLgeom ON).

The results of the finite element simulations using the ABAQUS software will be shown in the Results section.

### 4.3.6 Experimental set-up

Three-point bending tests were conducted to characterize stiffness change in layer-jamming structures, as shown in Figure 4.11a. We measured force and central displacement using an MTS Alliance RT/30 electromechanical machine equipped with a 1 kN load cell (MTS-E31665) with 0.01 N resolution. In each test, the distance between the support rollers (1 cm diameter) was set to 10 cm. The specimens were loaded at a constant displacement rate of 5 mm/min until a maximum deflection of 8 mm and then unloaded with the same velocity. Force and deflection data were acquired at a sampling rate of 10 Hz. A vacuum pump (Piab M10A6-BN) connected to a manual vacuum regulator and a highly flexible TPU tube was used to generate the vacuum pressure inside the specimens. We tested both the influence of the number of layers and vacuum pressure. We fabricated four layer-jamming structures with different numbers of layers (8,12,16,20). Each specimen was tested at a constant vacuum pressure of 68 kPa. We also tested the 20-layer structure at different vacuum pressure levels (24,48,68 kPa). Before each test, specimens were flattened on a rigid planar shelf and then centered on the supports. Each test was repeated three times and mean and standard deviation were computed.

### 4.3.7 Fabrication process

Specimens were fabricated following three main steps. i) First, sheets of copy paper (Fabriano, Copy2) with height  $h = 0.1$  mm were cut in stripes of 18 x 6 cm. ii) Then, the envelope was created. A thin film of TPU (0.009 mm in thickness) was cut in a rectangle of dimensions 20 x 13 cm. A 3D printed connector was inserted through a tiny hole inside the film and a thin layer of silicone was used to prevent air leakage. iii) Lastly, sheets were inserted inside the envelope and the edges were sealed through a thermosealer with a welding edge of 2 mm. In order to compare the experimental results to the theoretical predictions we experimentally evaluated the coefficient of friction  $\mu = 0.55$  and the Young's modulus  $E = 1.7$  GPa. These values are in accordance with the range of values found in literature [61, 134]. Due to the difficulties involved in the measure of the Poisson's ratio and the little influence on the analytical predictions, we used a value of  $\nu = 0.156$  found in literature [86].

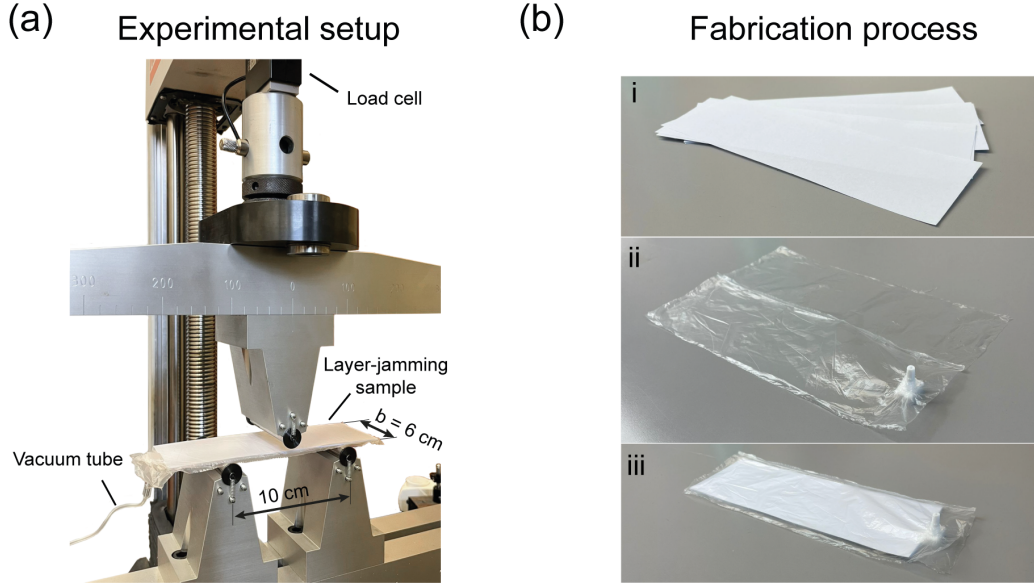


**Figure 4.11:** a) Experimental set-up for the three-point bending tests. b) Fabrication process of the layer jamming structures. i) First, sheets of copy paper were cut in stripes. ii) Then the envelope was created using a thin film of TPU and a 3D printed connector for the vacuum tube. iii) Lastly, sheets were placed inside the envelope and the edges were sealed with a thermosealer. (reproduced from [29])



## 4.4 Results

This section reports the results of the three-point bending experiments conducted on layer-jamming structures and the comparison with finite element analysis (large deflection model using ABAQUS) and the analytical predictions. The section is organized as follows. We first describe the effect of the number of layers, vacuum pressure and coefficient of friction during loading and unloading tests. Then we discuss the influence of the overhangs and guidelines for design optimization. Notice that for the coefficient of friction no test were conducted due to the difficulty involved in precisely controlling this parameter experimentally. Therefore, analytical predictions were only compared with finite element simulations.

In all the tests we measured force  $F$  and deflection  $w$  (Figure 4.12) as described in detail in the Experimental set-up section. Each combination of parameters was tested three times and mean curves and standard deviation (shaded area in Figure 4.12b-e) were computed.

### 4.4.1 Influence of the main design parameters

To study the influence of the number of layers, four structures were tested with different number of layers  $n$  (8,12,16,20) with  $b = 6$  cm (width),  $L = 18$  cm (total length),  $h = 0.1$  mm (height of a single layer),  $E = 1.7$  GPa (Young's modulus),  $\nu = 0.156$  (Poisson's ratio) and  $\mu = 0.55$  (coefficient of friction). The distance between the support was set to 10 cm and a constant vacuum pressure of 68 kPa was applied inside the structures. Tests were conducted following the experimental procedure explained in detail in the previous section.

Figure 4.12b shows the comparison between the analytical model, finite element simulations, and experiments during the loading phase. Both experiments and finite element simulations confirmed the assumption that in the first phase (Pre-slip) layer-jamming structures behave like a single linear elastic beam with a bending stiffness that scales with  $n^3$  since it is proportional to the second moment of area of the entire structure ( $I_{p-s} = b n^3 h^3 / 12$ ).

In this phase the stiffness is maximum and layers remain cohesive (no slip occurs at the interface between two adjacent layers). As the structure is further deflected, the shear stress increases until it reaches the frictional limit value  $\tau_{slip} = \mu p$  at the central interface. The model predicts that this shift happen when the external load reaches  $2F_0$  (Eq.4.31) which corresponds to a deflection of  $w_0$  (Eq. 4.35), and that these values scale with  $n$  and  $1/n^2$ , respectively.

Both experiments and numerical simulations confirmed that the model predicts this shift with great accuracy. For example, in the case of 8 layers, the model predicts that the structure remains in the pre-slip phase until  $w_0 = 11.3$  mm. Indeed, in the range of deflection tested (from 0 to 8 mm), the behavior of the 8-layer structure remains linear. After the first slip the bending stiffness begins to decrease and the behavior becomes nonlinear.

As explained in the analytical formulation section, we modeled this behavior using a piece-wise linear approximation based on slip propagation. Dots on the model curves indicate the critical loads and deflections at which these slip occurs and are described by Eqs. 4.31-4.38. We can observe that as the number of layers increases, the model underestimates the bending stiffness for high deflection with respect to both experiments and numerical simulations. The reason behind this difference is probably due to the increase in the shear stress caused by the increase in the contact pressure generated by the interaction with the supports. This effect is neglected in our model while is present in finite element simulations.

The loading phase was stopped at a deflection of 8 mm and the energy dissipated by the friction forces, represented by the area under each hysteresis curve, was evaluated by unloading the structures as shown in Figure 4.12d. We can observe that the energy loss due to friction increases with the number of layers and that in the unloading phase, the system releases only the bending energy accumulated in the pre-slip phase. Analytical predictions are in good agreement with experimental results and finite element simulations, demonstrating that the model is also able to accurately capture this hysteretic behavior.

Figure 4.12c shows the effect of vacuum pressure. The model predicts that the bending stiffness in the initial phase is not influenced by the vacuum pressure and that all the critical loads and deflections scale with the vacuum pressure  $p$ . This effect is captured by the model and reflected in both experiments and finite element simulations. It can be observed that the model underestimates the bending stiffness for high deflection as the vacuum pressure increases.

As discussed previously the reason behind this difference is probably due to the increase in the contact pressure in correspondence of the supports. Even in this case, the loading phase was stopped at 8 mm and the structures were unloaded (Figure 4.12e). Both experiments and finite element simulations confirm that the energy loss due to friction increases almost linearly with the vacuum pressure, as predicted by the model.

As explained previously no tests were conducted to evaluate the influence of

the friction coefficient. However, we compared analytical predictions with finite element simulations for a structure with 20 layers with different friction coefficients  $\mu$  (0.2, 0.3, 0.4, 0.5). The vacuum pressure was set to 70 kPa and all the dimensions were set equal to the real structure used in the experiments.

As expected, changing either the coefficient of friction or the vacuum pressure has the same influence on the behavior of the structure. Also in this case the energy dissipated by friction scale almost linearly with the coefficient of friction  $\mu$ .

### 4.4.2 Influence of the overhangs on the bending stiffness of the structure

For a typical single-layered beam subjected to a 3-point bending test, the curvature maintains a constant sign and the overhangs (regions of the beam outside the supports) do not influence its stiffness. However, for layer jamming structures, experiments and finite elements simulations have shown that the curvature sign changes and the overhangs remain almost flat, resembling the elastica of a clamped-clamped beam.

As described previously, we hypothesize that this counterintuitive behavior can be attributed to the difference in slip propagation between the regions inside and outside the supports. In the internal region (between the supports) the transverse load is constant and equal to  $(F/2)$ , while outside the support, it is zero. As the transverse load increases, the shear stress at the interfaces between the support increases. Therefore, when the shear stress reaches the frictional limit  $\mu p$ , the interfaces between the supports begin to slip, while the external regions remain attached.

Based on this assumption, the model considers the imaginary vertical line starting from the supports and separating the internal and external regions as perfectly clamped after the first slip. To test the validity of our hypothesis finite element simulations were conducted at different values of the overhanging length  $L_h$  for a structure with 20 layers subjected to a vacuum pressure  $p = 68 \text{ kPa}$  and with all the other parameters equal to the real structures used in the experiments.

Figure 4.13a shows the comparison between the prediction of the basic analytical model and that of the refined analytical model (which includes the influence of the overhangs). The predictions of the two models were compared with finite element simulations at different overhang lengths  $L_h$ . In the first phase (Pre-slip), finite element simulations are in excellent agreement with both the analytical models, confirming that when no slips occur, the presence of the overhangs has no effect on the bending

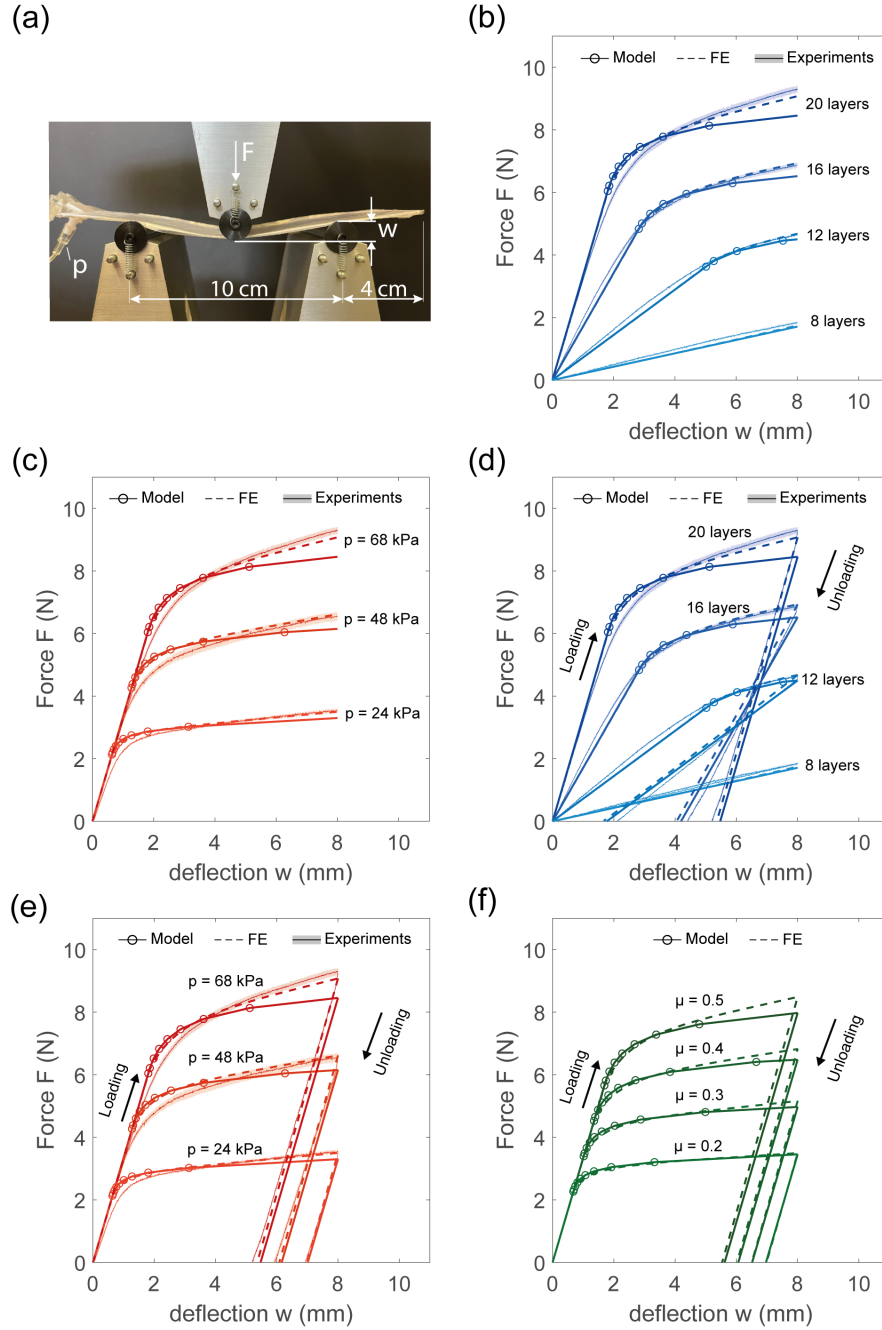


**Figure 4.12:** Comparison between theoretical predictions, finite element simulations and experiments. a) Photograph of the three-point bending set-up used in all the tests. b) Influence of the number of layers during the loading phase at a constant vacuum pressure (68 kPa). c) Influence of the vacuum pressure during the loading phase for a 20-layer structure. d) Energy dissipated by friction during a loading and unloading cycle with a different number of layers. e) Energy dissipated by friction during a loading and unloading cycle at different vacuum pressures. f) Energy dissipated by friction during a loading and unloading cycle with different coefficients of friction. (reproduced from [29])

stiffness of the structure.

In this initial phase, the structure behaves like a single-layered beam, since both the internal and external interfaces remain cohesive. However, after the first slip, finite element simulations show that bending stiffness is minimum for  $L_h = 0$  and then increases with  $L_h$  until it converges to a maximum value as depicted in Figure 4.13a. Interestingly, it is worth noting that all the possible behaviors obtained by varying  $L_h$  fall between an upper and lower limit that are well represented by the basic analytical model (simply supported) and the refined model (perfectly clamped).

Another important aspect is highlighted in Figure 4.13b, which shows images extracted from finite element simulations at the maximum deflection  $w = 4$  mm, both at the free end of the external region (green dashed box) and at an internal region between the supports (black dashed box), for different values of  $L_h$ . Images show that the propagation of slip in the internal region follows an opposite trend with respect to the external region. In particular, as  $L_h$  increases the number of interfaces that are in slip decrease at the free end while increase in the internal region. This fundamental aspect is also captured by the model (blue dots are more than red dots) and can be easily explained by considering that the bending stiffness grows with the increase in  $L_h$ . Having a higher bending stiffness means that the transverse load required to obtain the same deflection will be higher. Thus, higher transverse loads lead to higher shear stress at the interfaces, resulting in more interfaces that reach the frictional limit in the internal region.

Finally, Figure4.14 shows the comparison between the basic and refined theoretical models as well as finite element simulations at different number of layers, vacuum pressure, and coefficient of friction. All the dimensions, material properties and boundary conditions were chosen equal to those used in the experiments reported previously.

As already explained, all the plots show that until reaching the first slip, both models and finite elements simulations are in perfect agreement. Then, after the first slip, the basic model underestimates the bending stiffness of the structure while the refined model remains in good agreement with finite element results, confirming the importance of introducing the stiffness increase caused by the overhangs in the analytical formulation.

### 4.4.3 Design optimization

Having experimentally verified the accuracy of the analytical model across a range of conditions, the focus shifts to identifying performance characteristics and trends that can provide insights for designing and optimizing layer jamming structures for real-world applications. For example, consider an application in which the stiffness ratio between the jammed and unjammed state need to be maximized (e.g. for a soft ankle foot orthosis).

The goal is to design a system that is as soft as possible in its rest state (to ensure comfort) and as rigid as possible upon activation (to prevent ankle sprains). To achieve this goal we need to design a structure with as many layers as possible within the maximum allowable total thickness. As described previously, the stiffness ratio between the jammed and unjammed state scales with the square of the number of layers  $n^2$ , thus decreasing the thickness of the layers leads to an increase in the number of layers and consequently an increase in stiffness ratio.

For example, with a structure of 100 layers with a thickness of 0.1 mm (total thickness of 1 cm), an increase in stiffness of four orders of magnitude can be obtained. However, if the structure is subjected to high external loads or deflections (e.g. unexpected fall) the layers will enter in slip and the stiffness will dramatically decrease. This problem could be mitigated by increasing either the vacuum pressure or the coefficient of friction, which has the effect of increasing the loads and deflections at which the structure will enter in slip, as shown in Figure4.12c and Figure4.12f.

Similarly, the vacuum pressure and the coefficient of friction play an important role also in applications in which we want to tune the dynamic response of the systems (e.g. soft dampers, hand tremor suppressors). As shown in Figure4.12e-f, the energy dissipated by friction scales almost linearly with both the vacuum pressure and the coefficient of friction. Therefore, if we want to double the energy dissipated by the system, then we can double either the vacuum pressure or the coefficient of friction. The vacuum pressure can be adjusted on command by a vacuum regulator, thus the damping tuning can also be controlled in real-time.

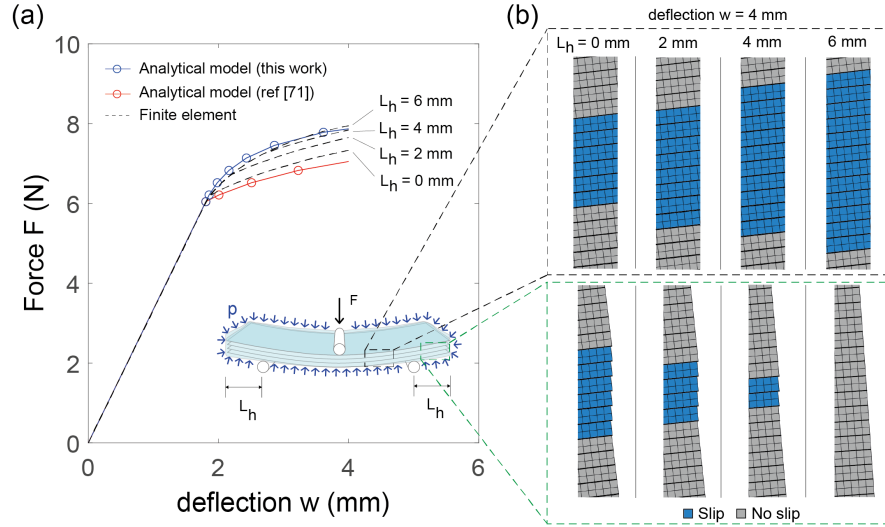


**Figure 4.13:** Influence of the length of the overhangs on the bending stiffness of layer jamming structures. a) Comparison between theoretical predictions and finite element simulations at different overhang lengths  $L_h$ . b) Images extracted from finite element simulations at a deflection of  $w = 4$  mm, showing the propagation of slip both in the internal and external regions. (reproduced from [29])

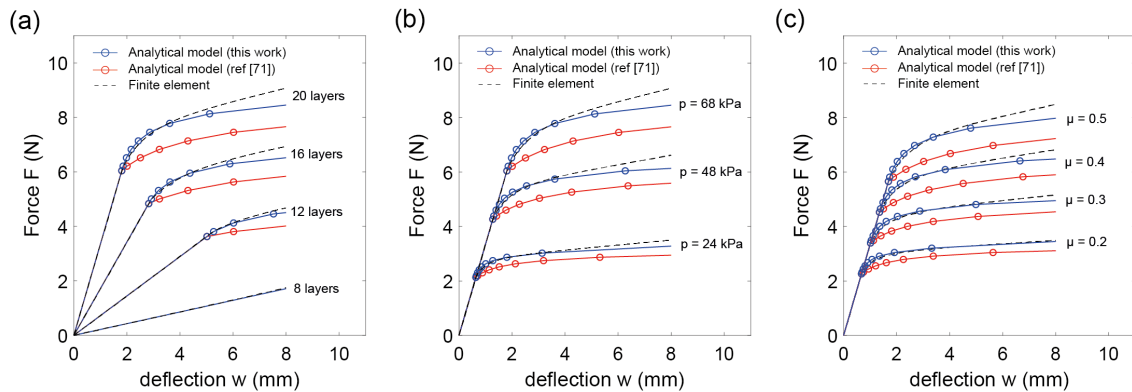


**Figure 4.14:** Comparison between the predictions of the basic model [28] that of the refined model [29] and finite element simulations, varying: a) the number of layers, b) vacuum pressure, c) coefficient of friction. (reproduced from [29])

### 4.5 Conclusions

In this chapter, the intrinsic mechanics of multi-layer jamming have been deeply investigated. We have presented a 2D analytical model for predicting the change in bending stiffness of a multi-layer jamming structure both in 3-point bending and cantilever configurations. Previous works introduced analytical models limited to the case of two-layers jamming structures and extended the analysis to multi-layer structures using finite element models.

In contrast, the model presented in this chapter predicts the change in stiffness as well as the transition loads and the corresponding deflections of a structure with an arbitrary number of layers. The model uses a piecewise linear approximation to capture the nonlinear change in stiffness in the partial-slip phase. To the best of the authors' knowledge, no studies investigated the computation of the bending stiffness during this nonlinear phase as well as the critical transverse loads at which these slips occur.

To keep the complexity of the formulation at an acceptable level, we have used the Euler-Bernoulli beam theory to model the layers and computed all the equilibria in the undeformed configuration. Our formulation is simple and computationally efficient compared to the finite element model, where the computational cost increases with the number of layers and the solution takes larger time to be obtained.

The experimental validation of the proposed approach was discussed by performing three-point bending tests, which showed good agreement between the predicted and actual behavior, especially considering that no fitting coefficients were adopted. Highly accurate finite element models were also constructed to further validate the theoretical predictions, showing how slip propagates between the layers.

Experimental and numerical evidence confirmed all the most important prediction of the model. Specifically, the model shows that the nonlinear behavior, beyond the initial deformation phase, can be well described with a piecewise linear approximation between subsequent slips. The stiffness declines as the slip propagates inside the structure. In particular, the model predicts that slip starts at the innermost interface and then progressively propagates towards the outer interfaces.

We have also refined the model including the effect of the overhangs outside the support. We discovered that the bending stiffness increases with the length of the overhangs, until it converges to a maximum value, which is well approximated by our theoretical predictions.

Finally, our model also provides a rapid design tool for the fabrication of improved



## **Chapter4. Layer jamming: Modeling and experimental validation**

---

layer jamming structures, predicting the influence of the main design parameters (number of layers, vacuum pressure and coefficient of friction) as well as the energy dissipated by friction during a load-unload cycle.

We believe that this work represents a significant step forward in understanding the complex intrinsic mechanics of layer-jamming structures that will help researchers to design more advanced variable stiffness applications in soft robotics.

# Chapter 5

## Electroadhesion zipping with soft grippers on curved objects

### 5.1 Introduction

As partially explained in Chapter 3, Electroadhesion (EA) soft grippers [104, 105, 32, 13, 102, 57], grasp fruit and vegetable without damaging them [26], separate textiles from a stack [39], are self-sensing [108] and hold large weights [27, 75]. Electroadhesion is silent, clean and low-power. Thin elastomer fingers conform to the shape of the object and ensure a delicate touch. EA creates mutual attraction between finger and object, which results in a large shear force [27, 75, 80, 89] with negligible compression of the object. Effective grasping requires the fingers to wrap around the object, conforming to its shape and establishing large surface area contact. This wrapping can be achieved in two ways, (1) by an actuator, (2) using EA force. Adding actuators has the advantage of independent control yet results in stiffer fingers with reduced conformability and complex fabrication [105, 75]. Recent works by the authors show how optimizing the grasping posture of EA soft grippers can lead to over 1000x increased grasping force [80]. In this work, we focus on using EA forces to wrap the fingers around an object, combining high conformability, soft fingers, and large holding forces.

Similar to electrostatic zipping actuators, EA fingers can be designed to spontaneously zip on an object when a voltage is applied. We report a model and a set

---

This Chapter has been adapted from the article:

[81] Massimiliano Mastrangelo, Fabio Caruso, Giuseppe Carbone, and Vito Caciucio. Electroadhesion zipping with soft grippers on curved objects. *Extreme Mechanics Letters*, 61:101999, 2023

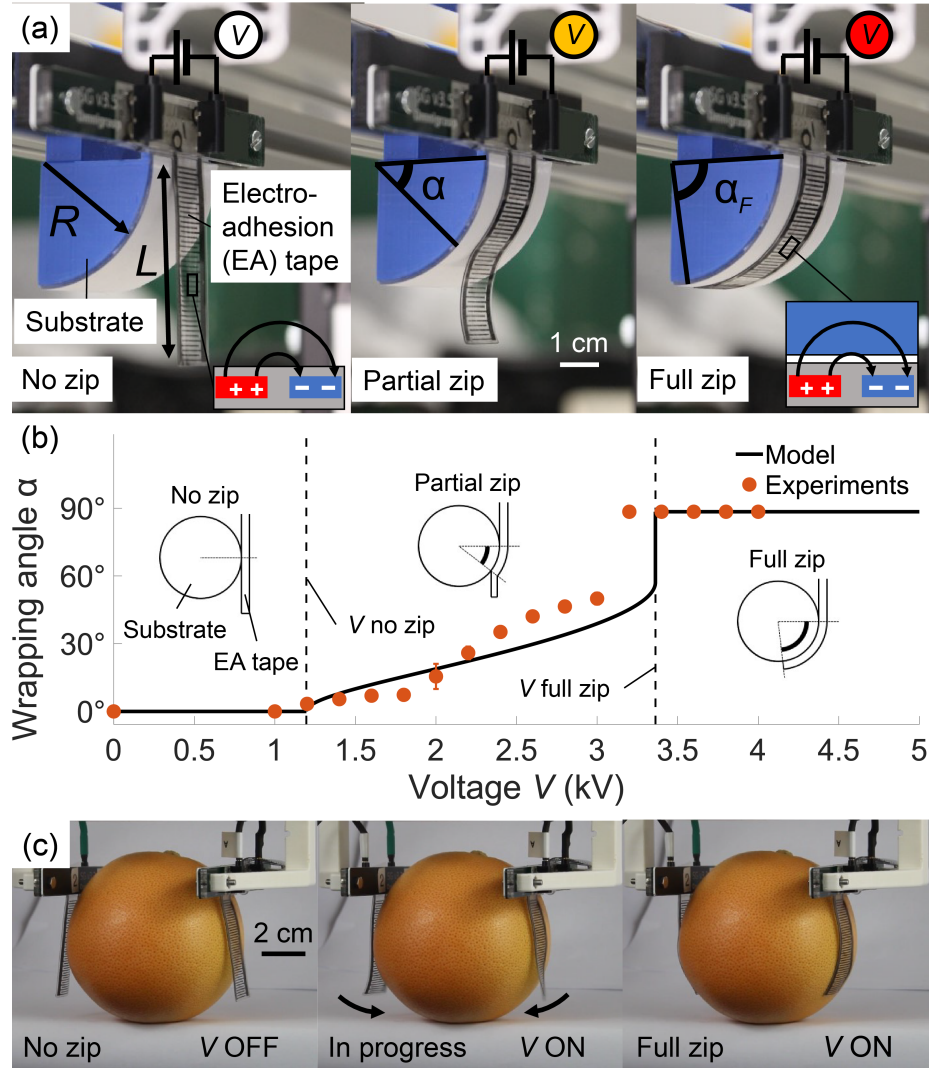


**Figure 5.1:** a) Zipping of an electroadhesion (EA) finger ( $L = 48$  mm) on a cylindrical object ( $R = 30$  mm), measured by the wrapping angle  $\alpha$ . Applying a voltage difference  $V$  across the interdigitated electrodes of the EA finger creates electrostatic forces that attract the finger to the curved substrate. The higher the voltage, the higher the wrapping angle, until the finger completely zips onto the objects (angle  $\alpha_f$ ). b) Voltage vs. wrapping angle model and experimental results ( $R = 30$  mm, DC voltage). Below the  $V$  no zip voltage threshold, the attraction forces are too weak to move the finger ( $\alpha = 0$ ). When the voltage exceeds  $V$  no zip, the finger partially zips on the object ( $\alpha < \alpha_f$ ). When the voltage further exceeds the  $V$  full zip threshold, the finger fully zips on the object, similarly to a pull-in instability ( $\alpha = \alpha_f$ ). c) A soft gripper with two fingers that wraps around a grapefruit using electroadhesion zipping (EAZ).

of experiments that characterize the design parameters (mechanical and electrical) for the zipping to happen on objects with different materials and geometry. The achieved large wrapping angles promise very high forces with simple and compliant soft grippers.

Electroadhesion (EA) uses electric fields to generate normal and shear forces between two contacting surfaces [89]. It enables wall climbing robots [48], electrohaptic devices [94, 54], soft actuators (where EA induces muscle-like contraction of the device) [115, 96, 74], electrical wound patches [22], and grippers [104, 13]. Its advantages are electrical control, absence of residues, and adaptation to a wide range of shapes and materials. EA soft grippers use interdigitated electrodes buried in a dielectric elastomer. When a voltage is applied between the electrodes, the fringing electric field induces charges on both the surface of the finger and the object. The surfaces mutually attract, generating adhesion (Figure 5.1a).

The holding force of EA grippers is strongly influenced by the grasping posture. As shown in previous works, the holding force increases by several orders of magnitude when the peeling angle between finger and object decreases [26] and keeps increasing exponentially when the fingers wrap around the object [27, 80]. Grippers that actively conform to the objects' shape have been demonstrated by combining EA with Dielectric Elastomer Actuators (DEAs) [105], Fin-Ray mechanism [31], and pneumatic actuation [49]. While helping the fingers envelop the object macroscopically, adding actuators results in higher stiffness, which negatively influences the actual contact area between the gripper and the object at a small scale. In contrast, EA zipping leverages electrostatic forces to wrap the fingers around the object without added stiffness, maximizing conformability at the roughness length scale. Electrostatic zipping has recently been demonstrated in a wide range of high-performance actuators such as electro-ribbon [115], HASELs [96], and HAXELS [74]. In these devices, the zipping typically happens between two films, each containing a flat electrode. Dielectric liquids are placed between the films to amplify the force output. EA zipping shares the main mechanism with zipping actuators but concerns soft fingers with interdigitated electrodes that zip on a curved object. There is no liquid in this case and the object can be made of any material and does not include electrodes. The goal is to use EA forces to make the fingers wrap around the object, which leads to very high grasping forces. Wrapping requires the fingers to bend and lift their center of mass (Figure 5.1a). The wrapping angle that can be achieved depends on the ratio between the EA forces and the mechanical restoring forces (bending moment and weight).

## Chapter5. Electroadhesion zipping with soft grippers on curved objects

This work reports an analytical and experimental investigation of EA zipping on curved objects. Our model and experimental data quantify the relation between the maximum wrapping angle, the applied voltage, and the finger and object mechanical (bending stiffness, mass, object radius) and electrical (dielectric constant) parameters. We discovered that the zipping of a flat finger on a cylindrical object is characterized by two voltage thresholds: a first one under which no zipping occurs and a second one over which the whole finger collapses onto the object (Figure 5.1b). Our results show that the zipping angle increases with  $V^2/d$ , unlike the  $V^2/d^2$  dependence previously reported for EA forces. By characterizing the two voltage thresholds we aim at providing a design tool to select materials and geometry for EA soft grippers that zip and effectively grasp a wide range of objects. We finally demonstrate the successful zipping of a pair of soft EA fingers on a set of real items (as shown in Figure 5.2).

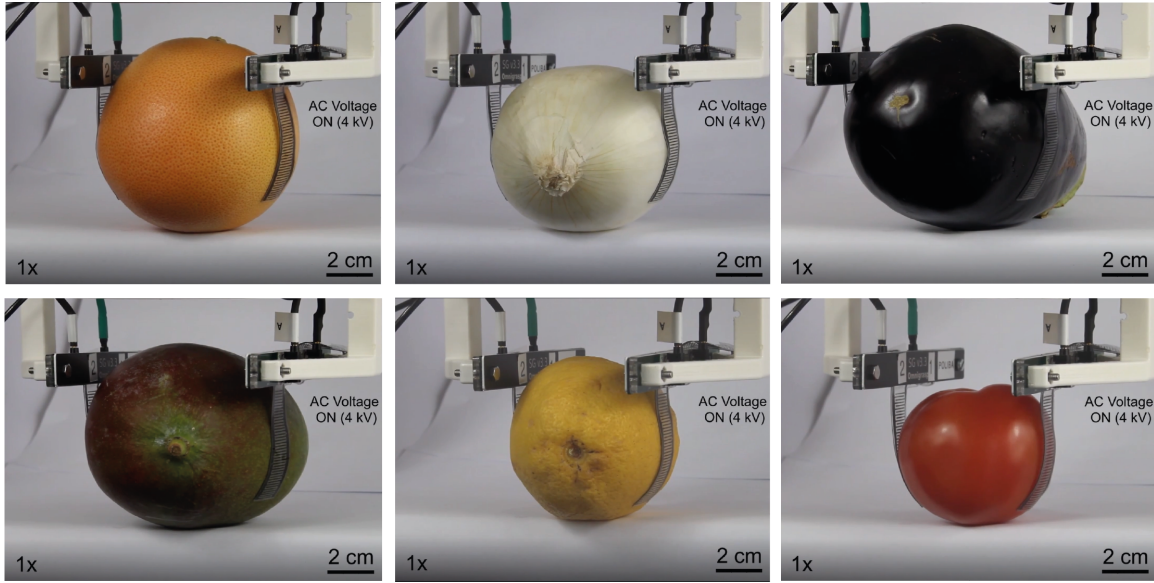


**Figure 5.2:** Snapshots taken from Supplementary video 4 [81]. Two electroadhesive soft fingers successfully zip on both sides of real objects of different sizes and shapes, when activated with an AC voltage (4 kV at 10Hz).

## 5.2 Analytical formulation

This section describes the mathematical model relating the wrapping of the EA finger, described by the angle  $\alpha$ , with the applied voltage  $V$ , for given materials and geometries of EA finger and object. We derived the formulation by writing the potential energy balance (in differential form) of the system composed of finger + object + battery, as similarly done for dielectric elastomers [114, 51] and fluid transducers [83, 64]. The model identifies two voltage thresholds. First, when the voltage is below a minimum value ( $V < V_{NOZIP}$ ) the EA fingers does not move ( $\alpha = 0$ ). For  $V > V_{NOZIP}$  the wrapping angle  $\alpha$  increases with the voltage. When the voltage exceeds the second threshold ( $V > V_{FULLZIP}$ ) the finger fully wraps around the object, reaching the maximum angle  $\alpha_F = L/R$ , with  $L$  the finger length and  $R$  the object radius (assumed constant). The relation between angle and voltage is nonlinear due to the gravitational energy term, while the electrostatic and the elastic energy terms are linear in this configuration.

We also report the equations of equilibrium obtained by writing the total potential energy of the system (function of  $\alpha$  and  $V$ ) and identifying the points where its derivative with respect to the angle  $\alpha$  is zero. This second method is reported later in subsection 5.2.5. The two methods lead to the same results.

We consider the system composed of the EA finger, modeled as an electrical capacitor formed by the interdigitated electrodes, air, and the curved object in its proximity, and a power supply modeled as a battery providing constant voltage  $V$ . The energies involved in the wrapping process are (1) the bending strain energy of the finger (Figure 5.3a) (2) the gravitational energy of the finger (Figure 5.3b), and (3) the electrical energy (Figure 5.3c) of both the finger capacitor and the battery. The model is quasi-static, so we do not include dynamic terms.

We analyze the equilibrium of the EA finger zipping on a cylindrical object of radius  $R$ . To write the equilibrium equation, we consider a small perturbation  $d\alpha$  from the system equilibrium described by the wrapping angle  $\alpha$  and the voltage  $V$ . A change in wrapping angle  $d\alpha$  is associated with the following variations in the system (Figure 5.4a,b): (1) the length of the EA finger in contact with the object increases linearly by a quantity  $d\alpha R$ , resulting in an increased capacitance of the EA capacitor, (2) a finger section of length  $d\alpha R$  deforms elastically from an undeformed straight position into a bent position of radius  $R$ , (3) the center of mass of the EA finger is lifted vertically by a quantity  $dz$  (nonlinear function of  $\alpha$ ).

The energy required for an infinitesimal increase of (1) the electrostatic energy



## Chapter 5. Electroadhesion zipping with soft grippers on curved objects

stored in the capacitor  $dU_{EL}$ , (2) the bending strain energy  $dU_F$  and (3) the gravitational energy  $dU_G$  of the EA finger is provided by the electrical power supply in the form of electrical work  $dW_{EL} = dQV$ . The potential energy balance of the system at equilibrium is written in differential form as:

$$dU_{EL} + dU_F + dU_G = dW_{EL} \quad (5.1)$$

The electrostatic energy of the capacitor can be written as  $dU_{EL} = 1/2 dQV$ , with  $Q$  the charge stored in the capacitor. The total electrical energy variation of the system results in  $dU_{EL} - dW_{EL} = -1/2 dQV$ . We introduce  $dU_{EA} = 1/2 dQV = 1/2 dCV^2$  as the variation of the electroadhesion energy system (with  $C$  the EA finger capacitance), where the electroadhesion energy is the electrical energy stored in the finger capacitor.

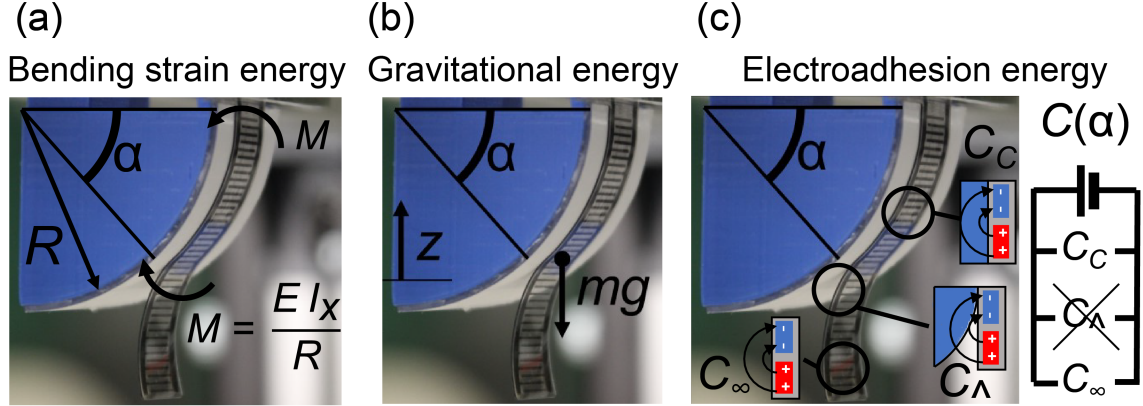


**Figure 5.3:** Energy components of the system involved in the zipping process: a) the bending strain energy, due to the bending of the finger around the object.  $M = EI_x/R$  is the pure homogeneous moment due to conforming to the constant curvature  $1/R$  of the object according to the Euler-Bernoulli slender beam theory, with  $E$  = finger Young's modulus,  $I_x = bt^3/12$  = second moment of area of the finger section; b) the gravitational energy due to the lifting of the finger center of mass ( $m$ ); c) the electroadhesion energy of the capacitor formed by the object, the finger and the surrounding air. The capacitance of the system  $C(\alpha)$  is calculated based on the capacitance values when the finger is fully zipped ( $C_c$ ) or at infinite distance from the object ( $C_\infty$ ). We found that the proximity of the object (accounted by  $C_\lambda$ ) barely affects the capacitance of the system.

Eq. 5.1 can be then written as

$$dU_F + dU_G = dU_{EA} \quad (5.2)$$

showing that the increased EA capacitive energy associated with an increase in the wrapping angle  $d\alpha$  balances the increase in mechanical energy  $dU_F + dU_G$ .

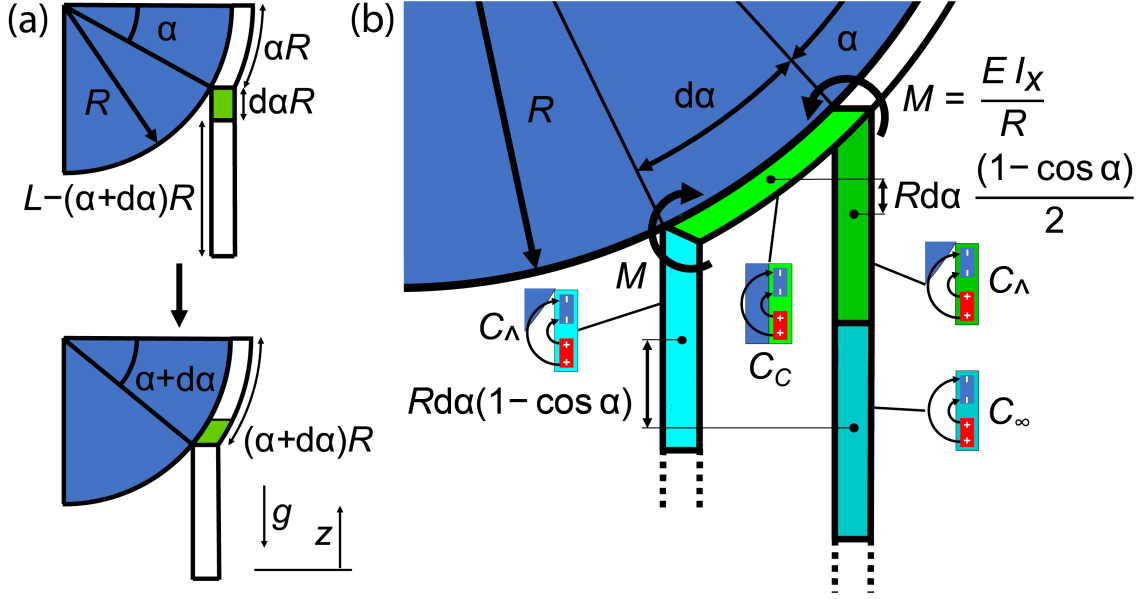


**Figure 5.4:** Schematic representation of the infinitesimal increase in the wrapping angle during the zipping process. a) The zipping advancement by an angle  $d\alpha$  involves the wrapping of an infinitesimal section  $Rd\alpha$  of the finger. b) When the infinitesimal section  $Rd\alpha$  of the finger wraps the object, it bends, and stores strain energy related to the moment  $M = EI_x/R$ . Its center of mass rises a quantity  $(Rd\alpha/2)(1 - \cos \alpha)$ , and the remaining unzipped finger center of mass rises by  $Rd\alpha(1 - \cos \alpha)$ . The capacitances of both the contributions change accordingly to new positions assumed with respect to the object.

### 5.2.1 Gravitational energy

When the wrapping angle increases by a quantity  $d\alpha$ , a finger portion of length  $Rd\alpha$  zips on the object (Figure 5.4a) and its center of mass rises by a quantity  $1/2Rd\alpha(1 - \cos \alpha)$  (Figure 5.4b). The mass of this finger portion is  $Rd\alpha \rho t b$ , with  $\rho$ ,  $t$  and  $b$  the mass density, thickness, and width of the finger, respectively. The center of mass of the remaining unzipped portion of the finger rises by a length  $Rd\alpha(1 - \cos \alpha)$ . The mass of this unzipped portion is  $(L - (\alpha + d\alpha)R)\rho t b$ . The infinitesimal variation of the gravitational energy  $dU_G$  is

$$dU_G = 1/2Rd\alpha \rho t b g Rd\alpha(1 - \cos \alpha) + (L - (\alpha + d\alpha)R)\rho t b g Rd\alpha(1 - \cos \alpha) \quad (5.3)$$



The derivative of  $U_G$  with respect to  $\alpha$  results in (second order terms neglected)

$$\frac{dU_G}{d\alpha} = (L - \alpha R)\rho t b g R(1 - \cos\alpha) \quad (5.4)$$

which is nonlinear due to the  $\cos\alpha$  term.

### 5.2.2 Bending strain energy

When the finger zipping increases of an angle  $d\alpha$ , a finger length  $Rd\alpha$  bends from straight to circular (radius  $R$ ), generating the restoring moment  $M$  (Figure 5.4b). The associated bending strain energy is  $dU_F = 1/2 M d\alpha = \frac{1}{2} \frac{E I_x}{R} d\alpha$ , according to the Euler-Bernoulli slender beam theory, with  $E$  = finger Young's modulus,  $I_x = \frac{bt^3}{12}$  second moment of area of the finger (Figure 5.7a). The infinitesimal variation in the bending strain energy of the finger is  $dU_F = \frac{1}{24} \frac{E b t^3}{R} d\alpha$ , so the derivative of  $U_F$  respect to  $\alpha$  is a constant value

$$\frac{dU_F}{d\alpha} = \frac{1}{24} \frac{E b t^3}{R} \quad (5.5)$$

### 5.2.3 Electrode adhesion energy

We define  $C(\alpha)$  the finger capacitance at wrapping angle  $\alpha$ .  $C_c$  is the capacitance of the finger when fully in contact with the object ( $\alpha = \alpha_F$ ), and  $C_\infty$  is the capacitance when the whole finger is at an infinite distance from the object. When the wrapping angle  $\alpha$  increases, the capacitance of the finger  $C(\alpha)$  increases since the dielectric constant of the object is always higher than the one of air. To capture the increase in capacitance due to an infinitesimal zipping  $d\alpha$ , we introduce the capacitance variation per unit length  $\Delta_\epsilon$ .  $\Delta_\epsilon$  is defined as the difference between the capacitance of a semi-electrode pair (half positive and half negative electrode, separated by a distance  $w$ , Figure 5.3c) when in contact with the object and when at infinite distance, divided by its length. When the finger zips of an angle  $d\alpha$ , its capacitance increases by a quantity  $\Delta_\epsilon R d\alpha$ . We use a semi-electrode pair as a unit since it fully captures the electric field shape for interdigitated electrodes. We computed the capacitance of a semi-electrode pair by using COMSOL FEM electrostatic simulations as done in [26], since for interdigitated geometries we cannot use simple analytical formulas as for parallel plate capacitors. By introducing  $\Delta_\epsilon$  and computing it once for given geometry and material using FEM simulations, we can then use an analytical formulation similar to parallel plate capacitors, where capacitance increases linearly with capacitor length  $C(\alpha) = \Delta_\epsilon R \alpha$ .

In reality the unzipped portion of the finger is at a finite distance from the object (Figure 5.4b), but we show that (1) we can neglect the small field concentration at the zipping boundary since this boundary effect is constant with zipping (the zipping boundary translates) and so it does not influence the capacitance difference and (2) the electrostatic energy of an unzipped region a few mm away from the object is practically very similar to the one of a finger at infinite distance. Figure 5.5 shows the comparison between the capacitance computed as  $C(\alpha) = \Delta_{\hat{c}} R \alpha$  and the one obtained simulating the whole finger using COMSOL FEM, demonstrating that the linear approximation introduces a negligible error.

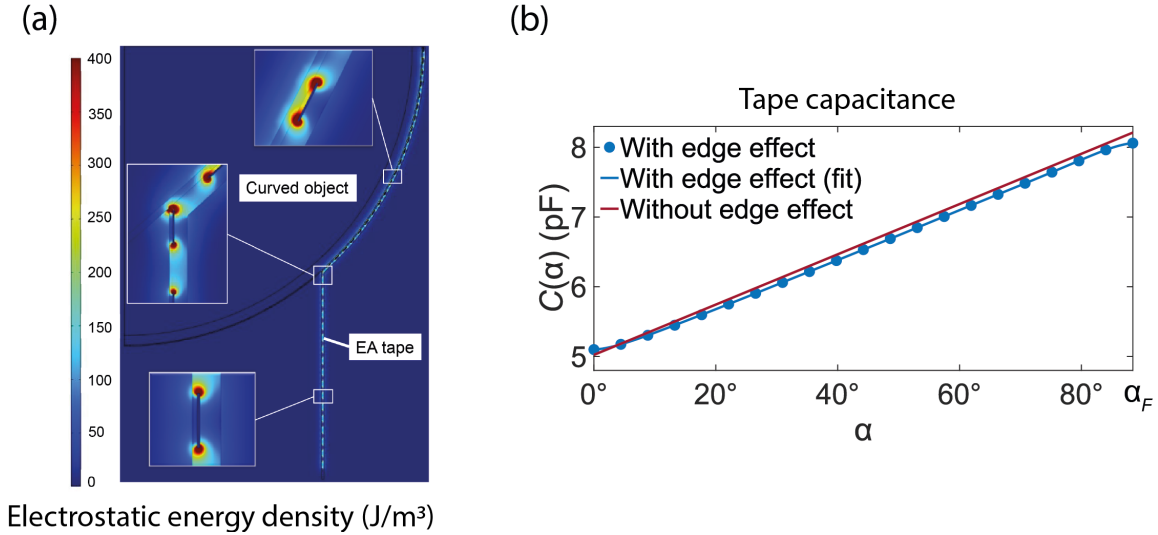


**Figure 5.5:** Electrostatic energy and capacitance of the entire tape computed with COMSOL. a) Visualization of the electrostatic energy density during the zipping process, extracted from COMSOL simulations. b) Tape capacitance with and without considering the edge effect. In blue the results from COMSOL simulation (including the edge effect at the zipping front), in magenta the results of the analytical model (neglecting the edge effect). The comparison shows that the assumption of neglecting the additional capacitance at the zipping front has little impact on the overall trend of the total capacitance of the tape. Therefore it has been neglected in the analytical formulation.

Following these considerations, we obtain the variation of  $U_{EA}$  with  $\alpha$  as a constant value during zipping, depending on the voltage squared

$$\frac{dU_{EA}}{d\alpha} = \frac{C_c - C_\infty}{2L} R V^2 = \frac{1}{2} \Delta_{\hat{c}} R V^2 \quad (5.6)$$

### 5.2.4 Wrapping angle as a function of the applied voltage

Following the potential energy balance of the system Eq. 5.28, we can write the equilibrium as

$$\frac{d(U_G + U_F)}{d\alpha} = \frac{dU_{EA}}{d\alpha} \quad (5.7)$$

and by using Eqs. 5.4-5.6 we obtain:

$$(L - \alpha R)\rho t b g R(1 - \cos\alpha) + \frac{1}{24} \frac{E b t^3}{R} = \frac{1}{2} \Delta \epsilon R V^2 \quad (5.8)$$

The LHS and RHS of Eq. 5.8 are plotted in Figure 5.6. The intersection points in the plot represent the states of equilibrium. The RHS (EA bending moment) increases with  $V^2$  and is plotted for different values of  $V$ . No equilibrium point exists until  $\frac{dU_{EA}}{d\alpha}$  reaches a minimum value, showing that zipping does not start until a voltage threshold ( $V$  no zip) is reached.

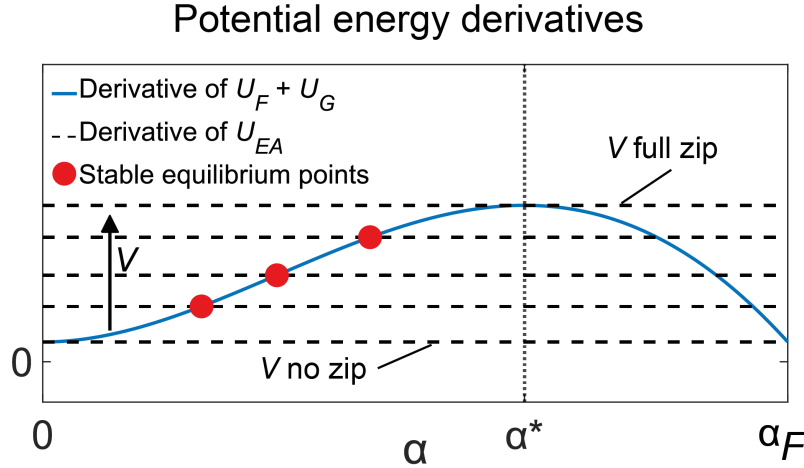


**Figure 5.6:** Visualization of the trends of the potential energy derivatives of Eq. 5.7. Red dots indicate the stable equilibrium points of the systems. The plot shows that there are no equilibrium points below the voltage threshold  $V_{NOZIP}$  and the wrapping angle remains zero. Between  $V_{NOZIP}$  and  $V_{FULLZIP}$  the systems can be in a stable equilibrium, and the wrapping angle increases with the voltage. When  $\alpha^*$  is reached the systems become unstable and the finger fully zips around the object. This interesting behavior has been predicted by the model and also confirmed by the experiments.

The value of  $V$  no zip can be calculated by using Eq. 5.8 at  $\alpha = 0$

$$V_{NOZIP} = \frac{1}{R} \sqrt{\frac{1}{12} \frac{E b t^3}{\Delta \epsilon}} \quad (5.9)$$

## Chapter 5. Electrode adhesion zipping with soft grippers on curved objects

---

It is interesting to notice that the mass density disappears (mass does not influence  $V$  no zip). Eq. 5.9 quantifies the minimum voltage that needs to be applied to an EA finger to initiate the zipping process. A higher bending stiffness leads to a higher  $V_{NOZIP}$  and a higher  $\Delta_{\hat{e}}$  leads to a lower value. Zipping on objects with a smaller radius  $R$  requires a higher voltage.

Solving Eq. 5.8 for the voltage, we obtain the relationship between applied voltage and wrapping angle at equilibrium

$$V = \sqrt{\frac{2}{\Delta_{\hat{e}}} \left[ (L/R - \alpha) \rho t b g R (1 - \cos \alpha) + \frac{1}{24} \frac{E b t^3}{R^2} \right]} \quad (5.10)$$

A higher wrapping angle  $\alpha$  requires a higher voltage  $V$ . Stable equilibrium (red points in Figure 5.6) at intermediate wrapping ( $\alpha < \alpha_F$ ) are only possible until a certain angle  $\alpha^*$ . Beyond that point, the whole finger collapses onto the object, similarly to an electrostatic pull-in. This effect is due to the nonlinear form of the gravitational energy term. The voltage that corresponds to this threshold is defined as  $V$  full zip. We compute its value using Eq. 5.8 and replacing  $\alpha = \alpha^*$ . The angle  $\alpha^*$  is obtained using the stability condition  $\frac{d^2(U_G+U_F)}{d\alpha^2} = \frac{d^2(U_{EA})}{d\alpha^2}$  that gives:

$$\rho t b g R [(L - \alpha R) \sin(\alpha) + R \cos(\alpha) - R] = 0 \quad (5.11)$$

Eq. 5.11 is satisfied for  $\alpha = 0$  and  $\alpha = \alpha^*$ . By rearranging and by recalling  $\alpha_F = L/R$ , one gets, for the case of  $\alpha = \alpha^*$ :

$$\alpha_F = \alpha^* + \frac{1 - \cos(\alpha^*)}{\sin(\alpha^*)} \quad (5.12)$$

The relationship between  $\alpha_F$  and  $\alpha^*$  appears to be constant and independent of any physical parameters. The reason is that both the bending strain energy and the EA energy are linear with  $\alpha$ , so they disappear in the second derivative. Therefore,  $\alpha^*$  depends only on the shape of the gravitational energy function and its geometric nonlinearities. We solved Eq. 5.12 numerically for  $\alpha_F < 90^\circ$  and found that  $\alpha^*$  can always be approximated as  $\alpha^* = 0.65\alpha_F$ . This result means that the angle at which the instability occurs is always the 65% of the final zipping angle  $\alpha_F = L/R$ . By replacing  $\alpha = \alpha^* = 0.65\alpha_F$  in Eq 5.10 we get an analytical solution for  $V$  full zip

## Chapter 5. Electroadhesion zipping with soft grippers on curved objects

---

(valid for  $\alpha_F < 90$ , which is practically always the case for EA soft grippers)

$$V_{FULLZIP} = \sqrt{\frac{2}{\Delta_{\hat{e}}} \left[ 0.35 \rho b t L g (1 - \cos(0.65L/R)) + \frac{1}{24} \frac{E b t^3}{R^2} \right]} \quad (5.13)$$

Eqs. 5.9 and 5.13 can be written to show the dependence of the two voltage thresholds on the ratio between the physical parameters of the system. By defining  $BS = \frac{1}{12} E b t^3$  as the bending stiffness of the EA finger, Eq. 5.9 becomes:

$$V_{NOZIP} = \frac{1}{R} \sqrt{\frac{BS}{\Delta_{\hat{e}}}} \quad (5.14)$$

$V_{NOZIP}$  represents both the theoretical threshold to initiate zipping and to initiate unzipping (Figure 5.6).

Similarly, by defining  $\gamma = 0.70 R^2 (1 - \cos(0.65L/R))$  the geometric factor, and using the mass  $m = \rho b t L$ ,  $V$  full zip from Eq. 5.13 becomes:

$$V_{FULLZIP} = \frac{1}{R} \sqrt{\frac{m g \gamma + BS}{\Delta_{\hat{e}}}} \quad (5.15)$$

Eqs. 5.14 and 5.15 can be used to quantify the zipping voltage required to initiate and fully zip an EA soft finger on a cylindrical object, given the geometry and materials of both finger and object.

### 5.2.5 Alternative approach

The following approach is an alternative with respect to the approach presented in the previous paragraph. Rather than modeling the system balance in differential form, here we write the total potential energy of the system, following the methods developed for dielectric elastomer actuators [51] and zipping actuators [83], modified with the use of the EA surface energy as shown in [26].

The energy components involved are (1) the bending strain energy  $U_F(\alpha)$  and (2) the gravitational energy  $U_G(\alpha)$  of the finger, and (3) the total electrical energy of the finger and the battery, written in terms of electroadhesion energy. The total potential energy  $U_T$  of the system is therefore:

$$U_T(\alpha, V) = U_F(\alpha) + U_G(\alpha) - U_{EA}(\alpha, V) \quad (5.16)$$

If the finger wraps the curved object by an angle  $\alpha$ , it becomes subject to a pure

## Chapter 5. Electrode adhesion zipping with soft grippers on curved objects

---

homogeneous moment  $M$  due to the constant curvature of the object. The associated bending strain energy is:

$$U_F(\alpha) = 1/2 M \alpha \quad (5.17)$$

By using Euler-Bernoulli slender beam theory, one gets that  $M = EI_x/R$ , with  $E$  = finger Young's modulus,  $R$  = object's radius,  $I_x = \frac{bt^3}{12}$  = second moment of area of the finger section with respect to the x-axis (Figure 5.7a),  $b$  = finger width,  $t$  = finger thickness. By recalling Eq. 5.17

$$U_F(\alpha) = \frac{1}{24} \frac{\alpha E b t^3}{R} \quad (5.18)$$

The gravitational energy related to the lifting of the finger center of mass during zipping is  $U_G(\alpha) = mgz(\alpha)$ , with  $m$  = finger mass,  $g$  = gravitational acceleration,  $z(\alpha)$  = vertical coordinate of the finger center of mass (Figure 5.7b). Define  $m = \rho b t L$ , with  $\rho$  = finger density,  $L$  = finger length. Consider the reference system  $z'$  (Figure 5.7b). When  $\alpha = 0$  the gravitational energy is

$$U'_G(\alpha = 0) = mgz'(\alpha = 0) = \rho b t L g L / 2 \quad (5.19)$$

In the zipped state, the gravitational energy is the sum of two contributes: (1) the one from the zipped section and (2) the one from the unzipped section:

$$U'_G(\alpha) = m_1(\alpha) g z'_1(\alpha) + m_2(\alpha) g z'_2(\alpha) \quad (5.20)$$

where  $m_1(\alpha)$  and  $z'_1(\alpha)$  are the mass and the  $z'$ -coordinate of the centre of mass of the zipped section, and  $m_2(\alpha)$  and  $z'_2(\alpha)$  are the mass and the  $z'$ -coordinate of the centre of mass of the unzipped section, respectively. Eq 5.20 becomes:

$$\begin{aligned} U'_G(\alpha) &= R^2 b t \rho g \int_0^\alpha \sin \theta d\theta + (L - \alpha R) b t \rho g \left( R \sin \alpha + \frac{L - \alpha R}{2} \right) \\ &= b t \rho g \left[ R^2 (1 - \cos \alpha) + (L - \alpha R) \left( R \sin \alpha + \frac{L - \alpha R}{2} \right) \right] \end{aligned} \quad (5.21)$$

By switching to the reference system  $z$ , since  $z = L/2 - z'$ , one gets:

$$U_G(\alpha) = \rho b t L g L / 2 - U'_G(\alpha) \quad (5.22)$$

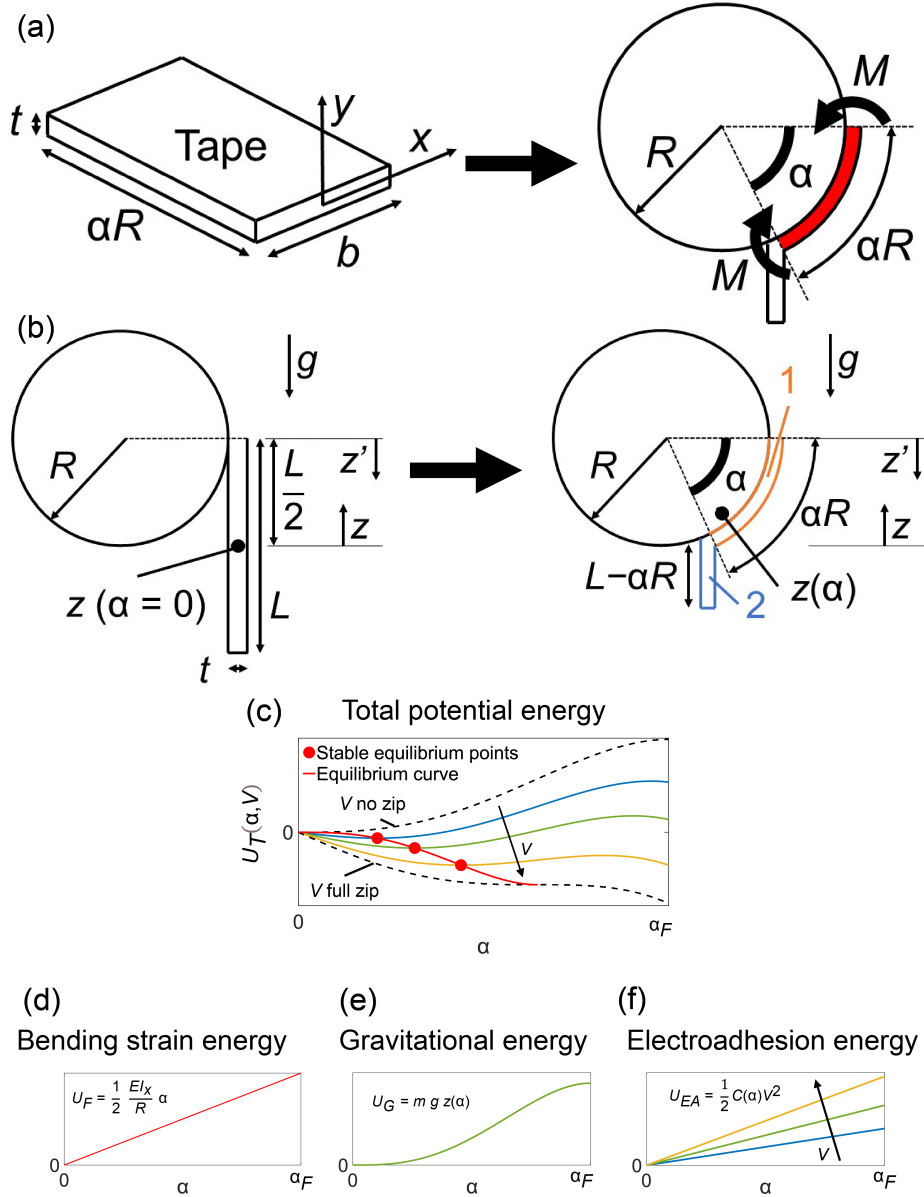


**Figure 5.7:** Schematic representation of reference systems and total potential energy contributions. a) The undeformed section  $\alpha R$  of the beam, and the same section (red) subject to bending. b) when undeformed, the gravitational energy of the finger is 0 in the  $z$ -reference system. When zipped, the gravitational energy of the finger is the sum of the contributions from sections 1 and 2. c) The total potential energy of the system (Eqs 5.16 and 5.25). d) The bending strain energy term (Eq. 5.18). e) The gravitational energy term (Eq. 5.23). f) The electroadhesion energy term (Eq. 5.24)

## Chapter 5. Electrode adhesion zipping with soft grippers on curved objects

and by recalling Eq. 5.22 one finally obtains:

$$\begin{aligned}
 U_G(\alpha) &= \rho b t L g L/2 - R^2 b t \rho g \int_0^\alpha \sin \theta d\theta - (L - \alpha R) b t \rho g (R \sin \alpha + \frac{L - \alpha R}{2}) \\
 &= b t \rho L g \left[ L/2 - \frac{R^2(1 - \cos \alpha) + (L - \alpha R)(R \sin \alpha + \frac{L - \alpha R}{2})}{L} \right] \quad (5.23)
 \end{aligned}$$

The total electrical energy of the system is the sum of the energy stored in the battery  $Q_b V$  and in the EA capacitor  $1/2 Q V = 1/2 C V^2$ . During zipping, charges move from the battery into the capacitor, but the total electrical charge of the system  $Q_T = Q_b + Q$  stays constant (conservation of charge). Therefore, we can write the total electrical energy as  $V(Q_b + 1/2 Q) = V Q_T - 1/2 V Q$ . Since the quantity  $V Q_T$  is constant, we neglect it and use as total electrical energy  $U_{EL} = -U_{EA}(\alpha, V) = -1/2 V Q = -1/2 C(\alpha) V^2$ , with  $C(\alpha)$  = capacitance of the EA finger. We introduced  $U_{EA}(\alpha, V)$  as the electrode adhesion energy, defined as the electrical energy stored in the capacitor formed by the interdigitated electrode, air and the portion of the curved object in contact with the finger.

We model  $C(\alpha)$  as the sum of two contributions (Figure 5.4c). One is the contribution coming from the zipped section of the finger. Given  $C_c$  the capacitance of the finger when fully wrapped around the object, when the finger is partially adhered to the object (wrapping angle =  $\alpha$ ) the contribution coming from the zipped section is  $C_c \frac{\alpha R}{L}$ .  $C_\infty$  is the capacitance of the whole finger when at an infinite distance from any object. The second contribute to  $C(\alpha)$  is therefore  $C_\infty \frac{L - \alpha R}{L}$ .  $C(\alpha)$  becomes  $C(\alpha) = C_c \frac{\alpha R}{L} + C_\infty \frac{L - \alpha R}{L} = C_\infty + (C_c - C_\infty) \frac{\alpha R}{L}$  and the total electrode adhesion energy becomes:

$$U_{EA}(\alpha, V) = \frac{1}{2} C_\infty V^2 + \frac{1}{2} (C_c - C_\infty) \frac{\alpha R}{L} V^2 \quad (5.24)$$

By using Eqs 5.18, 5.23, 5.24 becomes:

$$\begin{aligned}
 U_T(\alpha, V) &= U_F(\alpha) + U_G(\alpha) - U_{EA}(\alpha, V) = \frac{1}{24} \frac{a E b t^3}{R} - \frac{1}{2} (C_c - C_\infty) \frac{\alpha R}{L} V^2 - \frac{1}{2} C_\infty V^2 + \\
 &+ \rho b t L g \left[ \frac{L}{2} - \frac{R^2(1 - \cos \alpha) + (L - \alpha R)(R \sin \alpha + \frac{L - \alpha R}{2})}{L} \right] \quad (5.25)
 \end{aligned}$$

By deriving Eq 5.25 with respect to  $\alpha$ , one obtains the equilibrium of the system as expressed by Eq 5.8



### 5.3 Materials and methods

We conducted zipping tests with EA fingers on cylindrical objects to measure the wrapping angle  $\alpha$  while varying the applied voltage  $V$ . We tested both the quasi-static and dynamic responses. We tested both zipping and unzipping to evaluate the hysteresis. We used objects with radii of 30 and 45 mm, coated with either dielectric or conductive materials. As EA fingers we used thin rectangular stripes (48 mm long, 16 mm wide, 0.26 mm thick) made of PDMS (Polydimethylsiloxane) with carbon-loaded PDMS electrodes (Figure 5.8a). The electrodes are interdigitated, with an electrode width of 0.5 mm and a pitch of 0.7 mm (Figure 5.8b). The thickness of the insulating PDMS layer between the electrodes and the object is 0.045 mm. Since the volume fraction of electrodes materials is small, we assume homogeneous material properties equal to those of PDMS Sylgard 184 (Dow Corning): Young's modulus  $E = 3.9$  MPa [88], density  $\rho = 1030 \text{ kg/m}^3$  (Dow Corning datasheet [1])

We used Ketjenblack EC-300J (AkzoNobel) as carbon black for the electrodes. Finger fabrication followed the procedure described in [26]: (1) blade casting and curing of the PDMS backing, (2) blade casting and curing of conductive PDMS-carbon composite, (3) laser engraving of the electrodes, (4) blade casting and curing of PDMS top insulating layer.

We used 3D-printed PLA (Polylactic Acid, dielectric constant  $\epsilon_{PLA} = 3$  [17]) for the structure of the cylindrical objects (Figure 5.8). We applied four different coatings on these objects to study the influence of electrical and surface properties (Figure 5.8c): (1) 0.1 mm-thick paper ( $\epsilon_{paper} = 3$  [107]), (2) 0.1 mm-thick paper on top of 0.1 mm-thick copper, (3) 18  $\mu\text{m}$ -thick P(VDF-TrFE-CTFE) ( $\epsilon_{PVDF} = 30$  [5]), (4) 0.1 mm-thick copper. Coatings are bonded to the PLA object using a 3M VHB 4910 adhesive (1 mm-thick, dielectric constant  $\epsilon_{VHB} = 4.7$  [69]).

Each experiment starts with the finger in vertical position, tangent to the object (Figure 5.8a). We apply the voltage to the electrodes and measure the wrapping angle  $\alpha$ . For the quasi-static tests, we increased the voltage at a slow rate (200 V every 10 s) until full zipping. For the dynamic experiments, we applied a voltage step for 3s, followed by voltage off for 3s. The cycle is repeated increasing the voltage value by 400 V. We used voltage values not exceeding 4 kV to prevent electrical breakdown (4 kV corresponds to an electric field value in the top insulating layer of about 45 kV/mm, well below the 100 kV/mm breakdown threshold of Sylgard 184 films [12]). We used both DC and AC voltage (10 Hz bipolar square wave) applied with a DC-HVDC converted (XP Power A series) and high-voltage optocouplers (VMI OC 100G).

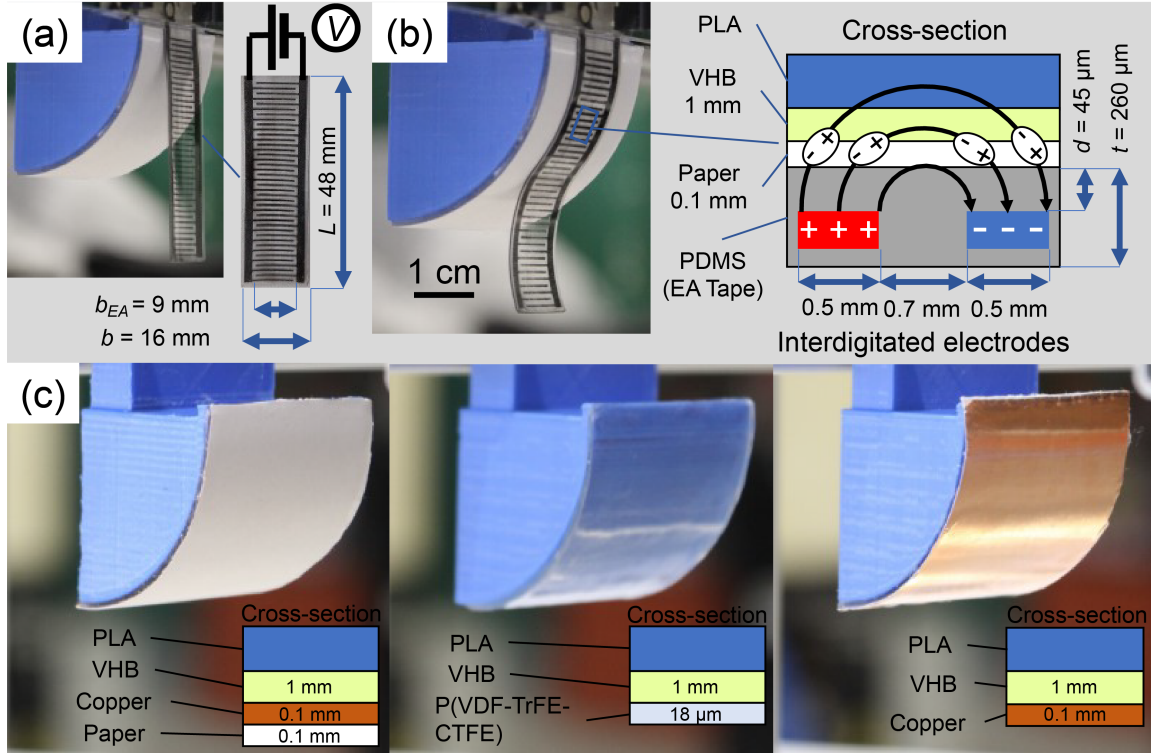


**Figure 5.8:** a) EA finger starting position for the experiments: the finger is vertical, tangent to the object. The finger length is  $L = 48$  mm,  $b = 16$  mm is the finger width, and  $b_{EA} = 9$  mm is the width of the interdigitated electrodes region. b) Finger partially zipped over the paper-covered object and schematic cross-section of the finger. The presence of the finger induces charges onto the object's surface, and the finger and the object mutually attract. c) Pictures of the curved objects used in the experiments covered by: 0.1 mm thick paper on top of 0.1 mm-thick copper (left); 18  $\mu$ m-thick P(VDF-TrFE-CTFE) (center); 0.1 mm-thick copper (right).

## 5.4 Results and discussion

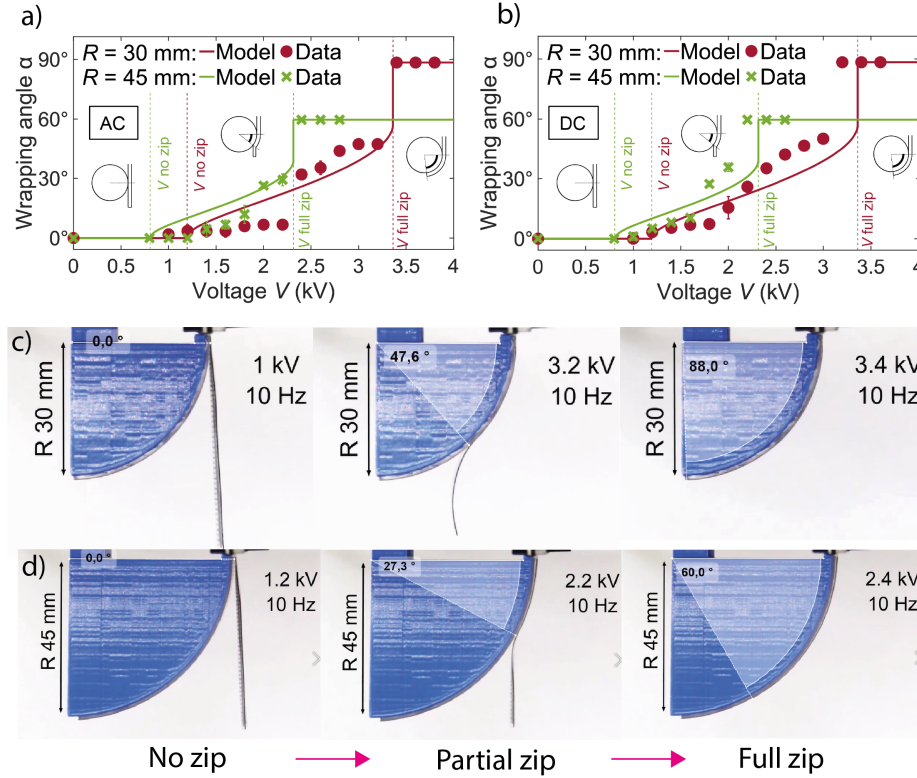
This section reports the results of the zipping experiments with EA fingers and the comparison with the model predictions. We conducted the following tests: 1) quasi-static zipping tests with different object radii using AC and DC voltage, 2) cycling zipping and unzipping tests, 3) comparison between different coating materials, 4) dynamic zipping tests, 5) load lifting. At the end of the section, we also report the results of a set of FEM simulations that can be used as a design tool to improve the zipping performance of an electroadhesive soft gripper. We also explore the feasibility of introducing layer jamming structures to vary the stiffness of the electroadhesive fingers.

### 5.4.1 Quasi-static zipping tests

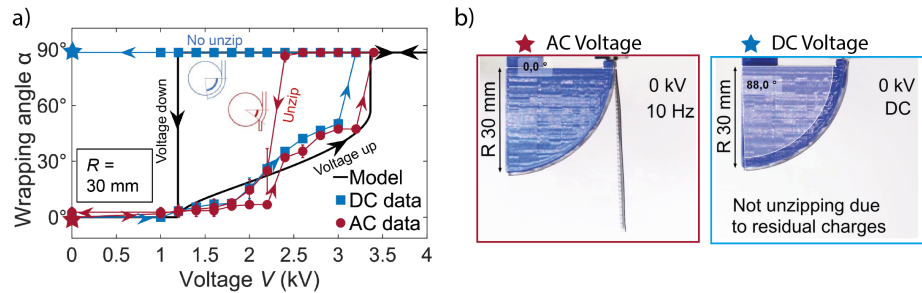
For all the quasi-static tests the voltage increasing rate is 200 V every 10 s. For AC voltage we use a superimposed bipolar square wave at 10 Hz. Each test is repeated three times and we plot the mean and standard deviation over the three trials.

Figure 5.9 show the validation of the zipping model, at two different radii (30 and 45 mm). Voltage is applied from 0 to 3.8 kV using a superimposed AC bipolar square wave (10 Hz). The AC modulation has the effect of both reducing dry adhesion and preventing charges building up in the dielectric materials facing the electrodes. Both model and data show that until reaching a minimum voltage value  $V$  no zip, the finger does not start moving. For higher voltages, the EA finger partially zips (wrapping angle  $\alpha > 0^\circ$ ) and keeps this position as long as the voltage is held. When the voltage value exceeds the  $V$  full zip threshold, the EA finger fully zips on the object. The model fits the trend in the data with good accuracy, especially considering that no fitting has been done on the parameters (all physical values). Possible reasons for the observed discrepancies include: (1) non-flatness of the EA finger due to the fabrication process, (2) unzipped region modeled as a vertical straight line for simplicity.

Figure 5.9b repeats the configuration of Figure 5.9a (the model is identical) but with the use of DC voltage. We observe that DC voltage leads to zipping at a lower voltage compared with model predictions. This effect is arguably due to charges building up in the dielectrics with time, as described in the literature for EA and other electrostatic actuators [54].



**Figure 5.9:** Quasi-static zipping tests. Validation of the zipping model for two object's radii (30 and 45 mm), by applying increasing AC (a) and DC (b) voltages. Both cases show the absence of wrapping until a voltage value ( $V$  no zip) is applied, and the increase in the wrapping angle with the voltage until full zip. c) and d) present snapshots from the recorded experiments, demonstrating the electroadhesive soft finger's ability to autonomously wrap progressively around the two curved objects tested as the voltage increases.



**Figure 5.10:** Zipping and unzipping cycle for both AC and DC voltage ( $R = 30$  mm). a) Comparison between model predictions and experiments. Apart from the differences between the two cases, the experiments capture the hysteresis predicted by the model due to the nonlinear shape of the potential energy. b) Snapshots extracted from the experiments, showing that in the case of DC voltage, the finger does not unzip due to residual charges.

### 5.4.2 Cycling zipping and unzipping tests

Figure 5.10 presents model and experimental results for a zipping and unzipping cycle, using both DC and AC voltage. Due to the nonlinear shape of the system free energy (Figure 5.7c) the EA finger remains zipped on the object when the voltage is decreased below the  $V$  full zip value. This effect is captured by the model and reflected in both AC and DC experiments. The model prediction is that unzipping should happen for  $V \leq V$  no zip. However, the unzipping with AC voltage happens earlier (higher voltage) than model predictions. The reason lies in the flatness of the free energy function in the full zip configuration (the range of stability is narrow). Dynamic effects due to AC oscillations are large enough to induce earlier detachment. In the DC case on the contrary, the finger remains attached even when voltage is removed (no unzip), arguably due to building up of charges in the dielectrics and creation of dry adhesion forces due to prolonged electrostatic pressure.

### 5.4.3 Influence of coating materials

To account for materials with different surface and electrical properties, we measured both no zip and full zip voltage values on a 30 mm radius object with 4 different coatings (quasi-static, DC voltage) (Figure 5.11). Coating materials: 0.1 mm-thick copper, 0.1 mm-thick paper on top of 0.1 mm-thick copper, 18  $\mu\text{m}$ -thick P(VDF-TrFE-CTFE), 0.1 mm-thick paper, all bonded to the object by means of 1 mm-thick VHB. Paper was chosen for most experiments as in normal conditions it does not stick to the silicone of the EA finger (negligible dry adhesion). We observe very good agreement between model and experiments for the case of paper. We then tested 18  $\mu\text{m}$ -thick P(VDF-TrFE-CTFE), which is a high- $\epsilon$  material (dielectric constant  $\epsilon = 30$  [5]). The model predicts lower values for both  $V$  no zip and  $V$  full zip compared to paper as the higher  $\epsilon$  leads to higher electrostatic forces. Data also show earlier zipping, while the value of  $V$  full zip is over 40% higher than model predictions. The reason behind this difference is yet to be understood. Possible explanations lie in the polarization dynamics of P(VDF-TrFE-CTFE). Since EA works with both dielectric and conductive objects, we also tested an electrically conductive surface (0.1 mm-thick copper coating). In this case, both  $V$  no zip and  $V$  full zip predicted by the model are lower than the  $\epsilon = 30$  case, as electrostatic forces are even higher. However, data values are over two times higher than predictions, and only slightly lower than data for paper coating. We cannot draw a conclusion about this discrepancy with these data only: the model does not include dynamics of electrical charges and by

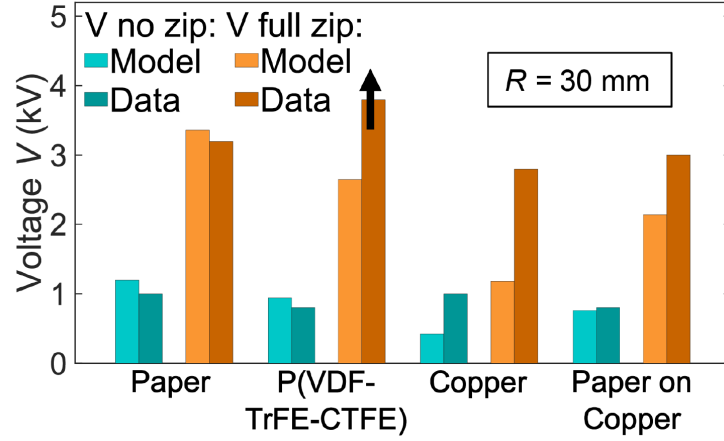


**Figure 5.11:** Comparison between model outcomes and experimental results of the wrapping of the EA finger around a curved object ( $R = 30 \text{ mm}$ ) coated with different substrates.

changing coating, both electrical and surface properties change at the same time. In order to control for surface, we finally tested an object coated by 0.1 mm-thick paper on top of 0.1 mm-thick copper. In this configuration, electrical forces are higher than in the paper case (due to the copper layer), yet the surface is unchanged. The error between model and experiments is reduced. The no zip voltage shows a very good matching, while the full zip voltage shows a 40% error (compared to over 200% for the copper case). The error reduction compared to the copper coating can be due to (1) controlling for surface, (2) electrical effects not modeled mediated by the presence of the paper layer.

#### 5.4.4 Dynamic zipping and unzipping tests

Time response of both zipping and unzipping is very important for the use of EA in soft grippers. We conducted dynamic tests by applying repeated voltage steps (3s on and 3s off, increased by 400 V at each cycle). Results of zipping time at different voltages are shown in (Figure 5.12a) and zipping and unzipping cycles in (Figure 5.12b). For the highest used voltage (3.6 kV) we measure a 90%-time response for zipping (0.419 s) and unzipping (0.328 s).



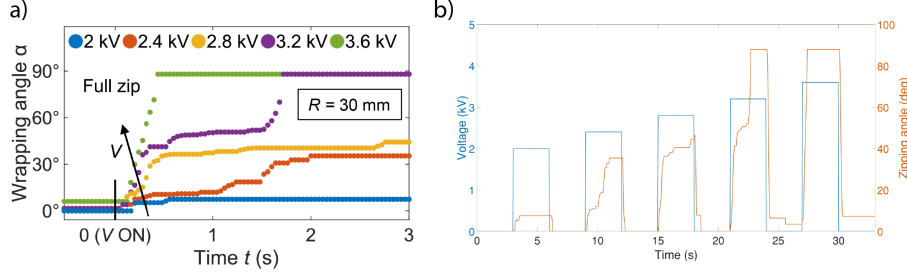


**Figure 5.12:** Dynamic zipping and unzipping tests. a) Wrapping angle vs. time at different applied voltages. Zipping speeds dramatically increase with the applied voltage. Full zip is reached at  $V = 3.2$  kV, and increasing the voltage to  $V = 3.6$  kV lead to a notable increase in wrapping speed. b) Plot of the applied voltage and wrapping angle during time.

#### 5.4.5 Influence of finger's mass

Finally, to further validate the model we conducted experiments of EA zipping, attaching a small load (1 g) at the finger tip and measuring the zipping angle at different voltages ( $R = 45$  mm, substrate paper). The effect of this additional load has been included in the model. The modified potential energy of the system is given by

$$U_T(\alpha, V) = \frac{1}{24} \frac{\alpha E b t^3}{R} + \rho b t L g \left[ \frac{L}{2} - \frac{R^2(1 - \cos \alpha) + (L - \alpha R)(R \sin \alpha + \frac{L - \alpha R}{2})}{L} \right] - \frac{1}{2} C_\infty V^2 - \frac{1}{2} (C_c - C_\infty) \frac{\alpha R}{L} V^2 + P g R (\alpha - \sin \alpha) \quad (5.26)$$

Eq 5.26 is plotted in Figure 5.13b. It is interesting to notice that in this case the wrapping angle  $\alpha$  increases with voltage until  $\alpha_F$  without instabilities (electrical pull-in is not expected in this case). Moreover, as already demonstrated in Eq.5.9 and confirmed by experiments,  $V_{NOZIP}$  is not influenced by the mass of the finger. On the contrary,  $V_{FULLZIP}$  increases significantly, as shown in Eq.5.15, becoming higher than the value that is safe to apply to the EA finger (4 kV). Also in this case model and experiments show a very good agreement (Figure 5.13a)

#### 5.4.6 Improving zipping performance

In this section, we report a set of simulations that map the change in capacitance  $\Delta_c$  for a given thickness  $d$  of the dielectric layer that separates the electrodes from the object and spacing  $w$  of the interdigitated electrodes. These results can be used as a design tool to increase  $\Delta_c$  and decrease the voltage required for zipping, for given

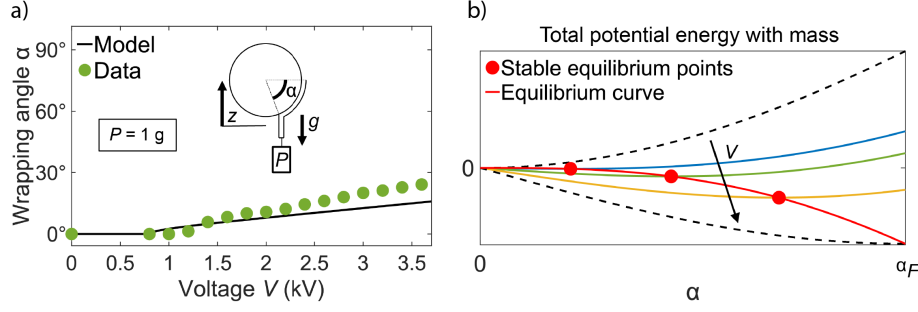


**Figure 5.13:** Influence of finger's mass. a) Comparison between model predictions and experiments conducted with a small weight (1 g) attached at the tip of the finger. b) Total potential energy of the system and stable equilibrium points including the effect of the additional mass.

mass and bending stiffness of the EA fingers.

The analytical model derived in the previous section describes how the zipping process is influenced by four quantities: (1) finger bending stiffness  $BS$ , (2) finger mass  $m$ , (3) capacitance variation per unit length  $\Delta\epsilon$ ; (4) a geometric factor  $\gamma$ . Eqs. 5.14, 5.15 suggest that the voltage required to start zipping ( $V$  no zip) and reach full wrapping on the object ( $V$  full zip) can be reduced by increasing the change in capacitance per unit length  $\Delta\epsilon$ , defined as the difference between the capacitance of a semi-electrode pair when in contact with the object  $C_c$  and when at infinite distance  $C_\infty$ , divided by its length.

As described in the previous section, we used COMSOL Multiphysics to compute the values of  $C_c$  and  $C_\infty$  for given geometry and materials, since the interdigitated electrodes geometry prevents the use of simple analytical formulas. The electrodes were modeled as contours with length  $250 \mu\text{m}$ , height  $25 \mu\text{m}$ , and an out-of-plane dimensions of  $9 \text{ mm}$ , with rounded edges to avoid field singularities. These values were chosen equal to the ones of the real finger used in the experiments. A constant potential difference  $V$  was applied between the electrodes. The EA finger cross-section is a rectangle with a fixed height of  $260 \mu\text{m}$  and a length that was varied as a function of the spacing between the electrodes  $w$ . The presence of the object (top) and the air (bottom) was modeled with a sufficiently large bounding box (height  $3 \text{ mm}$ ) to ensure that the size of the boundaries does not influence the estimated capacitance. Finally, to take into account the different dielectric materials involved, a dielectric permittivity was assigned to air ( $\epsilon_{\text{air}} = 1$ ), object ( $\epsilon_{\text{object}}$ ) and finger ( $\epsilon_{\text{tape}}$ ). Figure 5.14a shows a schematic representation of the semi-electrode pair used in the simulations. Figure 5.14b-d show the capacitance variation  $\Delta\epsilon$  as a function of the ratio between the spacing between the electrodes and the thickness of the dielectric layers  $w/d$ , with



$d = 45\mu\text{m}$ , for different combinations of dielectric permittivity of the object and EA finger. All plots show the same trend. The change in capacitance per unit length  $\Delta_{\hat{c}}$  increases by decreasing  $w/d$ , which is a result of the increase in the electrostatic energy density due to the reduction of the spacing between the electrodes (in other words, same electrodes boundaries per unit length). Values of  $w/d < 2$  are not shown as such geometry results in a higher electric field in-between the electrodes than between electrodes and the object. Such a situation is unwanted as the electric field in-between the electrodes does not contribute to EA. Figure 5.14b shows that when  $\varepsilon_{\text{tape}}$  is small, increasing  $\varepsilon_{\text{object}}$  leads to higher  $\Delta_{\hat{c}}$ . Figure 5.14c,d show that increasing  $\varepsilon_{\text{tape}}$  leads to a higher  $\Delta_{\hat{c}}$  only until  $\varepsilon_{\text{tape}} \leq \varepsilon_{\text{object}}$ . When  $\varepsilon_{\text{tape}} \geq \varepsilon_{\text{object}}$  further increasing  $\varepsilon_{\text{tape}}$  has negligible advantages. This effect can be explained by considering that the increase in  $\varepsilon_{\text{tape}}$  leads to an increase in both  $C_c$  and  $C_{\infty}$ , while  $\varepsilon_{\text{object}}$  influences only  $C_c$ .

Finally, we produced two maps that can be used as design tools for EA soft grippers. Figure 5.14e,f show the voltage required to initiate zipping ( $V$  no zip) and the voltage for fully wrapping the fingers around the object ( $V$  full zip) for different values of dielectric layer thickness  $d$ , fingers bending stiffness  $BS$  and finger mass  $m$ . We kept constant the ratio  $w/d = 16$  (value used in our experiments), the dielectric permittivity of the finger ( $\varepsilon_{\text{tape}} = 3$ ) and the object ( $\varepsilon_{\text{object}} = 3$ ).

The plots are obtained by first computing  $\Delta_{\hat{c}}$  using COMSOL and then using this value in Eqs. 5.14,5.15 to compute  $V$  no zip and  $V$  full zip for given mass and bending stiffness and with the geometrical factor  $\gamma = 311\text{mm}^2$ , which corresponds to an object of radius 30 mm and a finger length of 48 mm. Figure 5.14e,f show the regions of feasible design to obtain zipping with given finger geometry and material. As previously discussed, EA zipping does not scale with  $V^2/d^2$ . On the contrary, higher dielectric thickness ( $d$ ) and higher voltage lead to successful zipping with increased bending stiffness and mass. This effect will in turn influence the holding force of EA grippers for two reasons. The first one is that zipping influences how much a finger macroscopically wraps around an object, which greatly influences the grasping force [104]. The second reason is that zipping governs the microscopic compliance of the gripper with an uneven surface, which determines the surface area of the contact, which in turn determines the adhesion force [105].

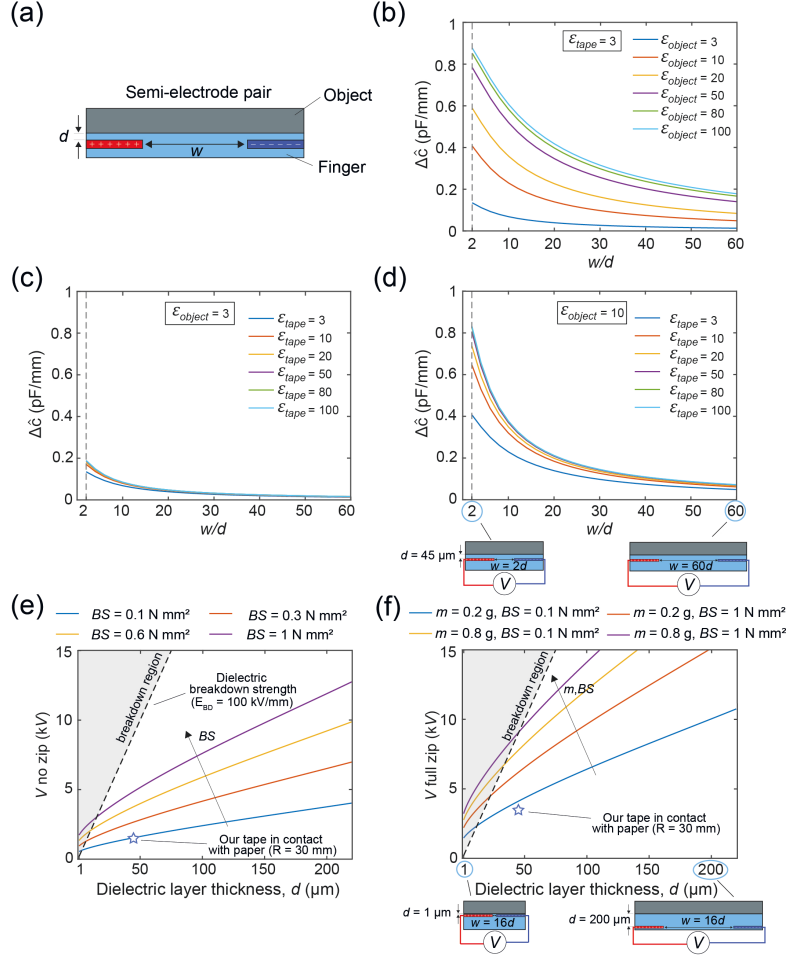


**Figure 5.14:** Influence of dielectric layers thickness and spacing between the electrodes on the zipping performance of an EA finger. a) Schematic representation of the semi-electrode pair used in COMSOL Multiphysics to estimate the capacitance variation per unit length  $\Delta\hat{C}$ , which influences the zipping voltage (see Eqs. 5.14, 5.15). b) Capacitance variation as a function of the ratio  $w/d$  for different values of  $\epsilon_{object}$ . Lower values of  $w/d$  lead to an increase in  $\Delta\hat{C}$ . c) Capacitance variation as a function of the ratio  $w/d$  for different values of  $\epsilon_{tape}$ .  $\epsilon_{tape}$  has little influence on  $\Delta\hat{C}$  when the dielectric permittivity of the object is small  $\epsilon_{object} = 3$ . d) Capacitance variation as a function of the ratio  $w/d$  for different values of  $\epsilon_{tape}$ , with  $\epsilon_{object} = 10$ . Increasing  $\epsilon_{tape}$  leads to higher  $\Delta\hat{C}$  only when  $\epsilon_{tape} \leq \epsilon_{object}$ . e) Design tool showing  $V$  no zip as a function of dielectric layer thickness and fingers bending stiffness, highlighting feasible and unfeasible (breakdown) zipping regions. f) Design tool for  $V$  full zip, showing feasible and unfeasible design regions with given dielectric layer thickness, mass and bending stiffness of the EA finger.

### 5.4.7 Stiffening the electroadhesive fingers with layer jamming

In this section, a preliminary exploration of the feasibility of introducing layer jamming structures as a way to achieve variable stiffness into electroadhesion soft grippers is presented. The analysis is conducted by combining the outcomes of the analytical models proposed in Chapter 4 (for layer jamming systems) and the ones presented in this Chapter (for zipping in electroadhesion soft gripper). The goal here is to simulate the integration of layer-jamming structures into the electroadhesive fingers used in the experiments to enable a  $90^\circ$  rotation of an object of 200 g with a deflection of less than 1 mm at the fingertip (Figure 5.15). We chose to simulate this scenario since it represents a typical task performed by grippers in industrial applications. We decided to use the electrostatic clutches developed by Hinchet and Shea [55] as a variable stiffness element.

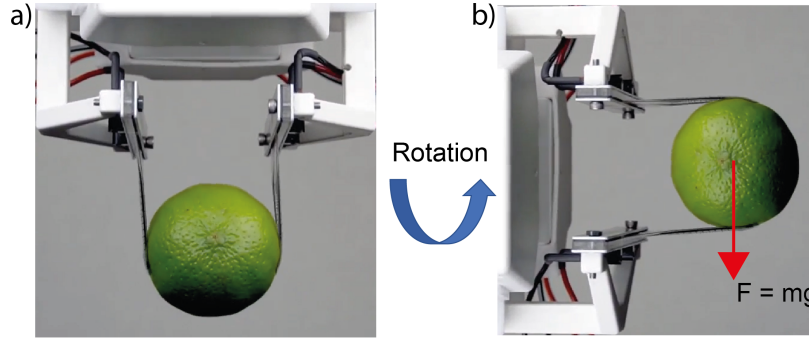


**Figure 5.15:** Visualization of the simulated scenario. Rotation of a lime (200 g) with a less than 1 mm deflection at the tip of the fingers. a) Snapshot taken from the Supplementary Video published in [26]. b) Same snapshot shown in a) but rotated of  $90^\circ$ .

## Chapter5. Electroadhesion zipping with soft grippers on curved objects

This choice was dictated by two reasons: 1) Compared to vacuum jamming, electrostatically-induced jamming shares the same advantages of electroadhesion soft grippers being ultra-low power, silent, and clean. 2) The electrostatic clutches presented in [55] can generate frictional stress up to  $21 \text{ N cm}^{-2}$  which are 2 times higher than the maximum pressure achievable with vacuum and 11 times higher than the electrostatic clutches reported in the literature. Figure 5.16c illustrates their working principle as well as materials and geometric dimensions. Although the model presented in Chapter 4 describes the behavior of layer-jamming structures made of paper sheets squeezed by vacuum pressure, it can be used without modification for the case in which layers are made of different materials and the pressure is generated by electrostatic forces.

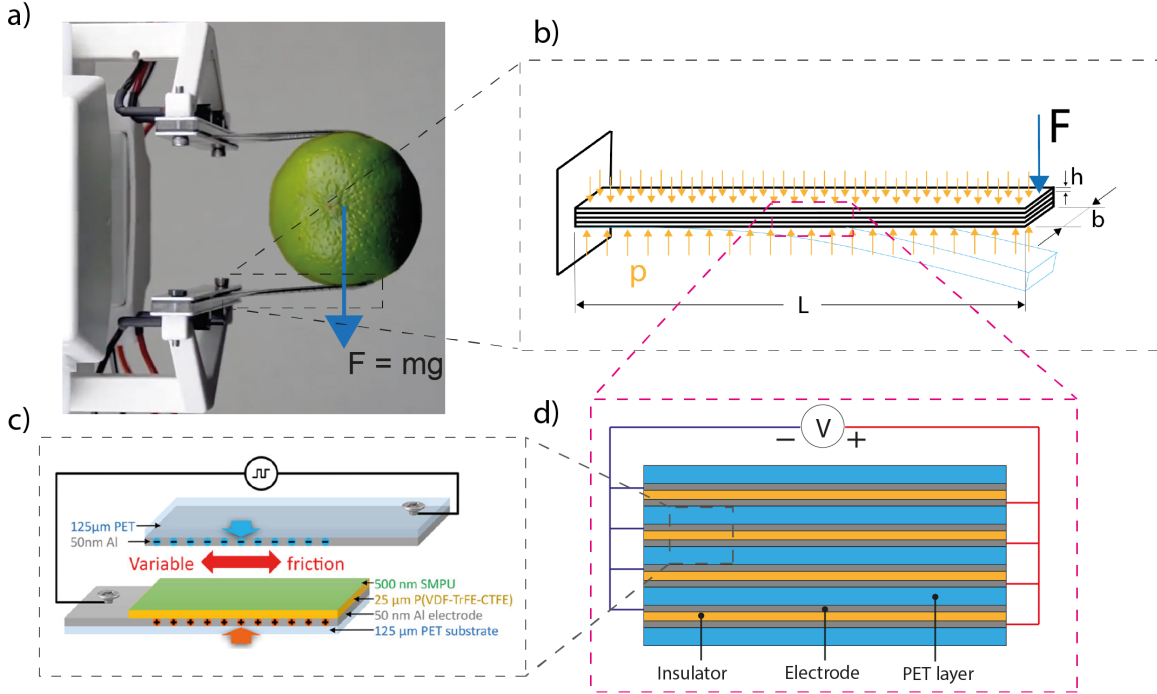


**Figure 5.16:** Description of the layer jamming structures used in the simulations. a) Visualization of the simulated scenario. b) Schematic of the cantilever jamming structure added to the electroadhesive fingers. c) Working principle and dimensions of the electrostatically induced variable stiffness element used in the simulations. (Reproduced from [55]). d) Illustration of the multiple stacks of variable stiffness elements and their electrical connections to a high-voltage power supply.

Therefore, in the simulations, we use equations 4.40-4.47 with material properties and thickness equal to the ones used for the electrostatic clutches developed in [55], with width and length equal to the electroadhesive fingers used in the experiments, that are: layer height  $h = 150 \text{ } [\mu\text{m}]$  (PET:  $125 \text{ } [\mu\text{m}]$  + P(VDF-TrFE-CTFE:  $25 \text{ } [\mu\text{m}]$ ), width  $b = 16 \text{ } [\text{mm}]$ , length  $L = 48 \text{ } [\text{mm}]$ , Young's modulus  $E = 3 \text{ } [\text{GPa}]$ , coefficient of friction  $\mu = 1$ , electrostatic pressure  $p = 210 \text{ } [\text{kPa}]$ . The outcomes of the analytical predictions are shown in Figure 5.17.

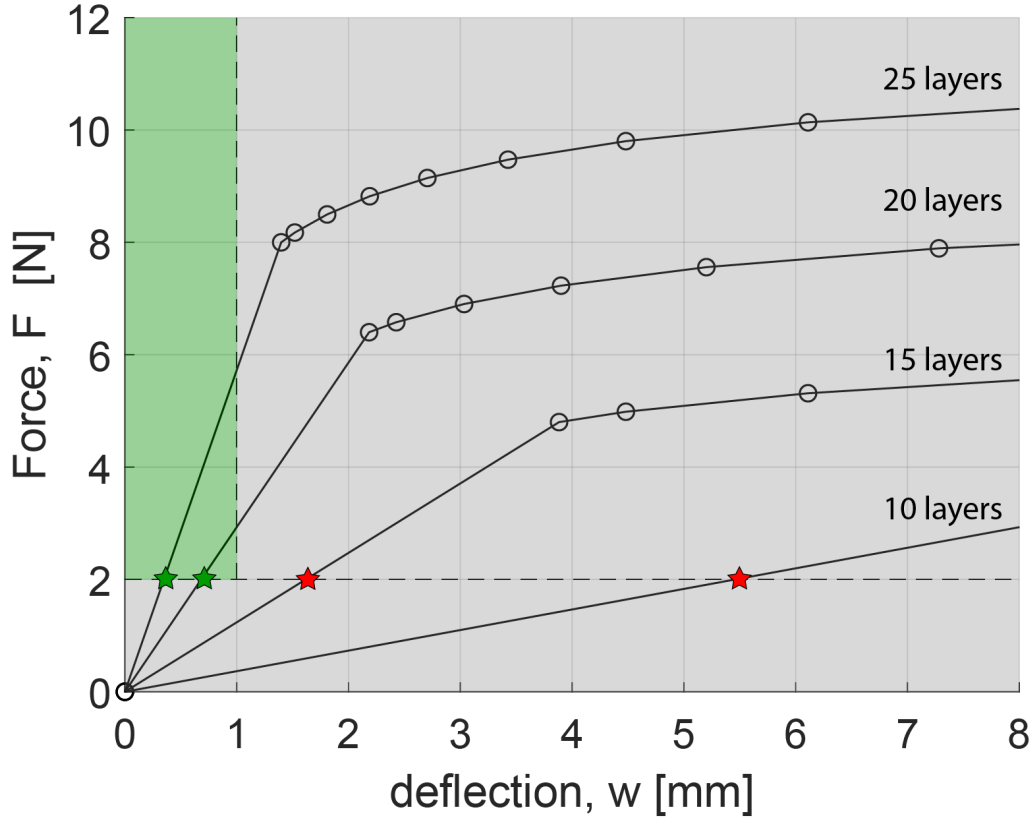


**Figure 5.17:** Analytical predictions of the force vs deflection curves experienced by cantilever jamming structures with material properties and thickness equal to the ones used for the electrostatic clutches developed in [55] and width and length equal to the electroadhesive fingers used in the zipping experiments presented in this chapter. Jamming structures composed of different numbers of layers were simulated, showing that only the structures with more than 15 layers (20 and 25 layers) can withstand a transversal force of 2 N (objects that weigh 200 g) with less than 1 mm deflection at the tip of the fingers. The green region indicates the range of forces and deflections that satisfy the design specifications (90° rotation of objects heavier than 200 g with less than 1 mm deflection at the fingertip) while the region in gray indicates the range of forces and deflections that do not satisfy the design specifications.

## Chapter 5. Electroadhesion zipping with soft grippers on curved objects

---

We simulated force vs deflection curves experienced by cantilever jamming structures with material properties and thickness equal to the ones used for the electrostatic clutches developed in [55] and width and length equal to the electroadhesive fingers used in the zipping experiments presented in this chapter. The goal of this analysis is to find the minimum number of layers needed to satisfy the design specifications (90° rotation of objects heavier than 200 g with less than 1 mm deflection at the fingertip). Analytical predictions indicate that structures composed of 15 and 10 layers subjected to a transversal force of 2 N, exhibit deflections of 1.7 mm and 5.5 mm, respectively. These deflections are higher than the design threshold of 1 mm. Structures with 20 layers, instead, experience deflections smaller than 1 mm and therefore will be considered for the second part of the analysis. Having found that a jamming structure with a minimum of 20 layers can satisfy the design specifications, we continue the analysis by studying the influence of the additional bending stiffness, introduced by the jamming structure, on the zipping performance of the electroadhesive fingers. The stiffness of the additional layers in the unjammed "soft" state should be low enough to still allow the fingers to spontaneously conform to the objects when high voltage is applied. To verify this fundamental requirement, we use the equations 5.14 and 5.15 presented in the previous sections, which describe the two voltage thresholds  $V_{nozip}$  and  $V_{fullzip}$  as a function of mechanical and electrical properties. The electrical properties remained unchanged since the geometry of the electroadhesive finger is the same. Only the mechanical properties, i.e. bending stiffness and mass need to be recomputed. The following equations report the recomputed values of the bending stiffness ( $BS_{20}$ ) and mass ( $m_{20}$ ) of the 20-layer jamming structures used in the analysis.

$$BS_{20} = \frac{Ebnh^3}{12} = 2700 \text{ Nmm}^2 \quad (5.27)$$

$$m_{20} = \rho bLn h = 3 \text{ g} \quad (5.28)$$

Substituting these values in equations 5.14 and 5.15 and computing for objects radii (R) between 30 and 60 mm we obtain the plot in Figure 5.18.

Analytical predictions show that adding a 20-layer jamming structure on the back of the electroadhesive fingers leads to a significant increase in the voltages needed to initiate (V no zip) and complete (V full zip) the zipping process, exceeding the breakdown threshold (100 kV/mm) of the dielectric (Sylicard 184) in between the interdigitated electrodes.

Therefore, although stiffening the electroadhesive fingers with a 20-layer jamming

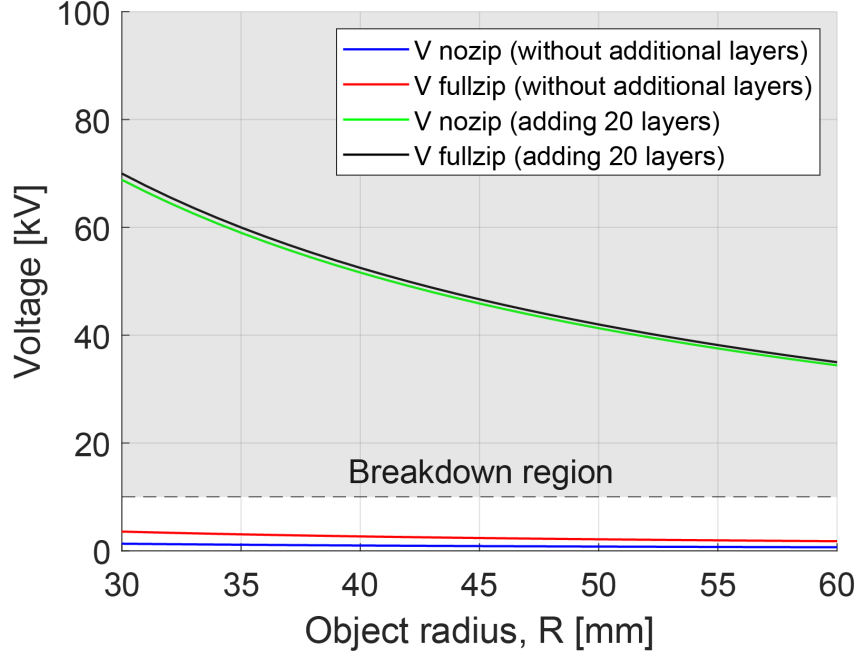


**Figure 5.18:** Plot of equations 5.14 and 5.15 showing the voltages to initiate (V no zip) and complete (V full zip) the zipping process as a function of the object’s radius, highlighting feasible and unfeasible (breakdown) design regions.

structure would allow the 90° rotation of an object of 200 g with a deflection of less than 1 mm at the fingertip, it would cause a significant increase in stiffness also in the soft (unjammed) state, that would lead to unfeasible higher voltages (higher than the breakdown threshold of the dielectric in between the interdigitated electrodes) required to conform to the lateral surface of the objects. The combination of the model outcomes suggests that electrostatically induced layer jamming could be an effective strategy to enable object rotation in electroadhesive soft grippers but highlights a strong constraint in the stiffness of the unjammed "soft" state. The minimization of the unjammed stiffness and the maximization of the stiffness ratio between the jammed and unjammed state are crucial in several soft robotic applications and represent a very active research field. Several methods have been already proposed to solve this problem. One promising approach is presented in [14] in which the concept of kirigami layer jamming is introduced for the first time. The authors have shown how intentional topological augmentation of layer jamming sheets through shell, void, and cut geometric primitives can significantly enhance the jammed to unjammed stiffness ratio by minimizing the second moment of area in the unjammed state. We believe that further research needs to be conducted trying to combine the Kirigami approach with other strategies proposed such as jamming sandwich structures [84] and stretch-

## **Chapter5. Electroadhesion zipping with soft grippers on curved objects**

able layer jamming [103] with the goal of minimizing the stiffness of the unjammed state and maximizing the ratio between jammed and unjammed state.



## 5.5 Conclusions

This chapter deals with EA soft grippers passively wrapping curved objects by means of EA-induced zipping (EAZ). We presented an analytical model (with two alternative approaches) to describe the zipping process and experiments to test the model outcomes. The model shows that EAZ on curved objects is the result of the balance between the electrical and mechanical features of the systems. Two voltage thresholds dictate the EAZ phenomenon: we found that no wrapping appears until the applied voltage reaches the first threshold and that full wrapping is only expected when a voltage greater than the second threshold is delivered by the voltage supplier. Between the two values, the wrapping angle increases with the applied voltage.

The model results are in good agreement with experiments, even if some observed phenomena need further investigation. The model does not account for the dynamics of the charges in the system or for the surface properties of the gripper-object interface, yet these effects seem to have a great influence in our experiments. Future investigations will focus on these issues.

Our model also provides design tools for the fabrication of improved passively wrapping EA soft grippers, highlighting the mutual relationship among electrical and mechanical parameters of the system and how it practically influences the wrapping behavior of the EA gripper.

We presented a preliminary exploration of the feasibility of introducing layer jamming structures as a way to achieve variable stiffness into electroadhesion soft grippers. The analysis is conducted by combining the outcomes of the analytical models proposed in Chapter 4 (for layer jamming systems) and the ones presented in this Chapter (for zipping in electroadhesion soft gripper). The combination of the model outcomes suggests that electrostatically induced layer jamming could be an effective strategy to enable object rotation in electroadhesive soft grippers but highlights a strong constraint in the stiffness of the unjammed (soft) state. Further research needs to be conducted trying to combine different approach including kirigami, stretchable and sandwich layer jamming structures, with the goal of minimizing the stiffness of the unjammed state and maximizing the ratio between jammed and unjammed state.

The demonstrated wrapping capabilities promise very high holding force according to previous works [27, 80]. However, extreme softness and compliance can still hinder manipulation capabilities of EA soft grippers, limiting their ability to rotate the grasped object or to move payloads fast. Future works will address this topic.

We believe that this work broadens the understanding of the capabilities of a passively conforming EA soft gripper, showing how wrapping moderately complex (curved) geometries can be obtained even without actuator-based conforming strategies. The outcomes shown in this work could also be adapted to various EAZ-based soft devices, such as HASELs [8], HAXELs [74], electro-ribbons and electro-origami [115] actuators, meaning that this paper can be used as a tool not only for the design of improved EA soft grippers, but also for soft actuators and soft machines that leverage Electroadhesion-induced Zipping.



# Chapter 6

## Conclusions

This thesis contributes to the field of soft robotics, broadening the understanding of the underlying mechanics of two promising soft robotics applications based on two different functional materials: i) variable stiffness devices based on layer jamming, and ii) electroadhesion robotic grippers based on electroactive polymers.

The first part investigates the intrinsic mechanics of layer-jamming structures, describing how the change in stiffness in these structures is related to the slip at the interfaces between the layers. A 2D analytical model for multi-layer jamming structures, both in 3-point bending and cantilever configuration, is presented in Chapter 4. To keep the complexity of the formulation at an acceptable level, Euler-Bernoulli beam theory has been used, and all the equilibria were computed in the undeformed configuration. The formulation is simple and computationally efficient compared to finite element models, where the computational cost increases with the number of layers and the solution takes larger time to be obtained.

Model outcomes were validated with experiments by performing three-point bending tests, which showed good agreement between the predicted and actual behavior, especially considering that no fitting coefficients were adopted. Experimental and numerical evidence confirmed all the most important predictions of the model. Specifically, the model shows that the nonlinear behavior, beyond the initial deformation phase, can be well described with a piecewise linear approximation between subsequent slips. The stiffness declines as the slip propagates inside the structure. In particular, the model predicts that slip starts at the innermost interface and then progressively propagates towards the outer interfaces. The model is also able to describe the very interesting and counter-intuitive experimentally observed phenomenon of curvature reversal. We discovered that the bending stiffness increases with the length of the overhangs until it converges to a maximum value, which is well approximated

by our theoretical predictions. The key advantage of the model is the ability to provide a rapid design tool for the fabrication of improved layer jamming structures, accurately predicting the influence of the main design parameters (number of layers, vacuum pressure and coefficient of friction) as well as the energy dissipated by friction during a load-unload cycle.

With the aim of integrating these systems into a useful real-world application, the second part of the thesis investigates the role of stiffness in zipping performance of electroadhesion-based soft grippers. We presented an analytical model to describe the zipping process and experiments to test the model outcomes. The model shows that zipping induced by electroadhesion is governed by the balance between electrical and mechanical features of the system. We found that two voltage thresholds dictate the zipping phenomenon: no wrapping appears until the applied voltage reaches the first threshold, and then full wrapping is expected when a voltage greater than the second threshold is applied. Between the two values, the wrapping angle increases with the applied voltage.

Model results are in good agreement with experiments, even if some discrepancies have been observed with different materials. The model does not account for the dynamics of the charges in the system or for the surface properties of the gripper-object interface, yet these effects seem to have a great influence in the experiments. The model also provides design tools for the fabrication of improved passively wrapping EA soft grippers, highlighting the mutual relationship among electrical and mechanical parameters of the system and how it practically influences the wrapping behavior of the EA gripper. Finally, we presented a preliminary exploration of the feasibility of introducing layer jamming structures as a way to achieve variable stiffness into electroadhesion soft grippers. The analysis is conducted by combining the outcomes of the analytical models proposed in Chapter 4 (for layer jamming systems) and the ones presented in Chapter 5 (for zipping in electroadhesion soft grippers). The combination of the model outcomes suggests that electrostatically induced layer jamming could be an effective strategy to enable object rotation in electroadhesive soft grippers, but highlights a strong constraint in the stiffness of the unjammed (soft) state.

### 6.1 Contributions

To the best of our knowledge, this work is the first to provide the following:

1. Analytical modeling of layer jamming structures with an arbitrary number of layers in 3-point bending and cantilever configurations.
2. A detailed description of slip propagation experienced by a multi-layer jamming structure subjected to a concentrated transversal load.
3. A detailed description of the relationship between slip propagations and stiffness decline in the nonlinear (partial-slip) phase after the first slip.
4. An analytical and numerical model for predicting the increase in bending stiffness of multi-layer jamming structures caused by the overhangs outside the supports in a 3-point bending test. (curvature reversal)
5. Analytical modeling of electroadhesion-induced zipping of soft electroadhesive grippers on curved objects.
6. Design tool for the fabrication of improved passively wrapping electroadhesion-based soft grippers

### 6.2 Future work

Concerning layer jamming structures, the following list presents interesting opportunities for future work:

1. **Analytical modeling of multi-layer jamming structures subjected to distributed loads:** In Chapter 4, a 2D analytical model was presented to describe the complex intrinsic mechanics of layer jamming structures with an arbitrary number of layers, both in 3-point bending and cantilever configurations, subjected to concentrated transversal loads. The model predicted that slip starts at the innermost interface and then progressively propagates towards the outer interfaces. These predictions were validated with experiments and visualized through finite element simulations. However, as shown in [86], analytical models become much more complex in the presence of distributed loads since the shear stress varies also along the interface between two adjacent layers, leading to a more complex slip propagation. Therefore, although the model

presented in this thesis could be helpful in many applications in which external forces can be approximated as concentrated loads, future work is needed to describe the intrinsic mechanics of multi-layer jamming structures when subjected to distributed loads. This would not only broaden the understanding of the complex behavior of these structures but also would provide a rapid design tool for more advanced variable stiffness applications in soft robotics.

2. **Analytical modeling of sandwich jamming structures:** The model presented in Chapter 4 considers only layer jamming structures made of layers with equal material properties. However, as shown in [84], the exceptional stiffness range of standard layer jamming structures could be combined with the high stiffness-to-mass ratios of classical sandwich composites by introducing stiffer layers as external layers and softer layers at the core. Extending the analytical model proposed in this thesis to the case of layer jamming structures with different material properties and thicknesses could be useful in predicting the behavior of sandwich jamming structures with the aim of further improving their performance.
3. **Improving jammed to unjammed stiffness ratios, trying to minimize the stiffness of the unjammed state:** As discussed in Chapter 5, several applications in soft robotics require a transition between a soft state, in which the stiffness should be as low as possible, and a rigid state, in which the stiffness should be high enough to meet the design requirements. Therefore, future works should focus on the minimization of the unjammed stiffness and the maximization of the stiffness ratio between the jammed and unjammed states. One promising approach is presented in [14] in which the concept of kirigami layer jamming is introduced for the first time. The introduction of voids and cuts can significantly reduce the stiffness of the unjammed state while preserving high stiffness ratios. This concept could be combined with sandwich jamming structures to minimize the stiffness of the unjammed state and maximize the ratio between jammed and unjammed states.

Concerning electroadhesion-based soft grippers, the following list presents interesting opportunities for future work:

1. **Exploration of different variable stiffness strategies to enable high accuracy and object rotation in electroadhesion-based soft gripper:** As described in Chapter 5, due to their extremely soft structures, electroadhesion-based soft grippers can self-adapt and successfully grasp a wide variety of objects when subjected to high voltage. However, the softness of the materials with which they are made makes it almost impossible to achieve high accuracy during object manipulation (due to vibrations caused by inertial forces) and to rotate even lightweight objects (due to high deflections of the fingers caused by bending moments). With the goal of solving these problems, in this thesis, we have explored the possibility of embedding variable stiffness structures, based on the layer jamming phenomenon, into the electroadhesive fingers. The combination of the model outcomes suggests that this could be an effective strategy but highlights a strong constraint in the stiffness of the unjammed "soft" state. Future work should focus on novel strategies, exploring different functional materials activated by different stimuli, with the aim of minimizing the stiffness of the "soft" state and maximizing the soft-to-stiff state ratios.
2. **Novel gripper designs to mitigate the peeling effect:** As described in Chapter 3, electroadhesion-based soft grippers experience grasping force changes of over three orders of magnitude depending on the grasping posture (peeling angle). This effect limits the versatility of the gripper, hindering the manipulation of objects that cannot be grasped from the sides (i.e., flat objects, bin picking). It would be extremely useful to explore novel designs capable of improving grasping performance from the top. Future work should focus on trying to match the performance of traditional grippers. Achieving this goal would pave the way for replacing high-power consumption grippers (like vacuum suction cups and pneumatic grippers) with an ultra-low power consumption alternative (electroadhesion soft grippers).
3. **Investigating the influence of charge accumulation on zipping performance:** The model presented in Chapter 5 describes how the zipping phenomenon is governed by the balance between electrical and mechanical features of the system. Model predictions are in good agreement with experiments, even if some discrepancies have been observed with different materials. The model does not account for the dynamics of the charges in the system or for the surface



properties of the gripper-object interface, yet these effects seem to have a great influence on the experiments. Following the illuminating approach proposed by Sîrbu et al. [109] future work should focus on integrating these effects in the model with the goal of understanding the zipping behavior and improving zipping performance on objects with different materials and surface properties.

# Bibliography

- [1] Dow corning, sylgard 184 silicone elastomer datasheet., (n.d.). <https://www.dow.com/documents/en-us/productdatasheet/11/11-31/11-3184-sylgard-184-elastomer.pdf>.
- [2] Electrostatic plotter <https://www.hpmuseum.net/exhibit.php?class=4cat=24>.
- [3] Grabit inc., electroadhesion robotic gripper: pick and place of different objects, <https://www.youtube.com/watch?v=riainjd6ukk>.
- [4] Grabit inc. website, <https://grabitinc.com/products/>.
- [5] Polyk technologies, p(vdf-trfe-ctfe) datasheet, high dielectric constant p(vdf-trfe-ctfe) terpolymer film. (n.d.). <https://piezopvdf.com/ctfe-terpolymer-film-low-ctfe-18-um/>.
- [6] Soft robotic in website, <https://www.softroboticsinc.com/>.
- [7] Ruben Acevedo, Luis Santos, RD Pedersen, N Goyal, NM Bruck, SK Gupta, and HA Bruck. Characterization and modeling of layer jamming for designing engineering materials with programmable elastic-plastic behavior. *Experimental Mechanics*, 60:1187–1203, 2020.
- [8] Eric Acome, Shane K Mitchell, TG Morrissey, MB Emmett, Claire Benjamin, Madeline King, Miles Radakovitz, and Christoph Keplinger. Hydraulically amplified self-healing electrostatic actuators with muscle-like performance. *Science*, 359(6371):61–65, 2018.
- [9] Buse Aktaş and Robert D Howe. Flexure mechanisms with variable stiffness and damping using layer jamming. In *2019 IEEE/RSJ International Conference on Intelligent Robots and Systems (IROS)*, pages 7616–7621. IEEE, 2019.
- [10] Buse Aktaş and Robert D Howe. Tunable anisotropic stiffness with square fiber jamming. In *2020 3rd IEEE International Conference on Soft Robotics (RoboSoft)*, pages 879–884. IEEE, 2020.

- [11] Buse Aktaş, Yashraj S Narang, Nikolaos Vasios, Katia Bertoldi, and Robert D Howe. A modeling framework for jamming structures. *Advanced Functional Materials*, 31(16):2007554, 2021.
- [12] Fabio Beco Albuquerque and Herbert Shea. Influence of humidity, temperature and prestretch on the dielectric breakdown strength of silicone elastomer membranes for deas. *Smart Materials and Structures*, 29(10):105024, 2020.
- [13] Vahid Alizadehyazdi, Michael Bonthron, and Matthew Spenko. An electrostatic/gecko-inspired adhesives soft robotic gripper. *IEEE Robotics and Automation Letters*, 5(3):4679–4686, 2020.
- [14] Robert Baines, Bilige Yang, Luis A Ramirez, and Rebecca Kramer-Bottiglio. Kirigami layer jamming. *Extreme Mechanics Letters*, 64:102084, 2023.
- [15] Mahdi Baniasadi, Alireza Foyouzat, and Mostafa Baghani. Multiple shape memory effect for smart helical springs with variable stiffness over time and temperature. *International Journal of Mechanical Sciences*, 182:105742, 2020.
- [16] Robert P Behringer and Bulbul Chakraborty. The physics of jamming for granular materials: a review. *Reports on Progress in Physics*, 82(1):012601, 2018.
- [17] Bahareh Behzadnezhad, Bruce D Collick, Nader Behdad, and Alan B McMillan. Dielectric properties of 3d-printed materials for anatomy specific 3d-printed mri coils. *Journal of magnetic resonance*, 289:113–121, 2018.
- [18] Bharat Bhushan. Biomimetics: lessons from nature—an overview. *Philosophical Transactions of the Royal Society A: Mathematical, Physical and Engineering Sciences*, 367(1893):1445–1486, 2009.
- [19] Rainer Bischoff, Johannes Kurth, Günter Schreiber, Ralf Koeppel, Alin Albu-Schäffer, Alexander Beyer, Oliver Eiberger, Sami Haddadin, Andreas Stemmer, Gerhard Grunwald, et al. The kuka-dlr lightweight robot arm-a new reference platform for robotics research and manufacturing. In *ISR 2010 (41st international symposium on robotics) and ROBOTIK 2010 (6th German conference on robotics)*, pages 1–8. VDE, 2010.
- [20] Loïc Blanc, Alain Delchambre, and Pierre Lambert. Flexible medical devices: Review of controllable stiffness solutions. In *Actuators*, volume 6, page 23. MDPI, 2017.
- [21] Loïc Blanc, Bertrand François, Alain Delchambre, and Pierre Lambert. Characterization and modeling of granular jamming: models for mechanical design. *Granular Matter*, 23:1–13, 2021.

- [22] Leah K Borden, Ankit Gargava, and Srinivasa R Raghavan. Reversible electroadhesion of hydrogels to animal tissues for suture-less repair of cuts or tears. *Nature Communications*, 12(1):4419, 2021.
- [23] Margherita Brancadoro, Mariangela Manti, Fabrizio Grani, Selene Tognarelli, Arianna Menciassi, and Matteo Cianchetti. Toward a variable stiffness surgical manipulator based on fiber jamming transition. *Frontiers in Robotics and AI*, 6:12, 2019.
- [24] Margherita Brancadoro, Mariangela Manti, Selene Tognarelli, and Matteo Cianchetti. Fiber jamming transition as a stiffening mechanism for soft robotics. *Soft robotics*, 7(6):663–674, 2020.
- [25] Eric Brown, Nicholas Rodenberg, John Amend, Annan Mozeika, Erik Steltz, Mitchell R Zakin, Hod Lipson, and Heinrich M Jaeger. Universal robotic gripper based on the jamming of granular material. *Proceedings of the National Academy of Sciences*, 107(44):18809–18814, 2010.
- [26] Vito Cacucciolo, Herbert Shea, and Giuseppe Carbone. Peeling in electroadhesion soft grippers. *Extreme Mechanics Letters*, 50:101529, 2022.
- [27] Vito Cacucciolo, Jun Shintake, and Herbert Shea. Delicate yet strong: Characterizing the electro-adhesion lifting force with a soft gripper. In *2019 2nd IEEE International Conference on Soft Robotics (RoboSoft)*, pages 108–113. IEEE, 2019.
- [28] Fabio Caruso, Giacomo Mantriota, Luciano Afferrante, and Giulio Reina. A theoretical model for multi-layer jamming systems. *Mechanism and Machine Theory*, 172:104788, 2022.
- [29] Fabio Caruso, Giacomo Mantriota, Vincenzo Moramarco, and Giulio Reina. Layer jamming: Modeling and experimental validation. *International Journal of Mechanical Sciences*, 251:108325, 2023.
- [30] Fabio Caruso, Giacomo Mantriota, and Giulio Reina. An analytical model for cantilever layer-jamming structures. In *The International Conference of IFToMM ITALY*, pages 193–200. Springer, 2022.
- [31] Rui Chen, Ruizhou Song, Zhuo Zhang, Long Bai, Fuqiang Liu, Pei Jiang, Dirk Sindersonberger, Gareth J Monkman, and Jianglong Guo. Bio-inspired shape-adaptive soft robotic grippers augmented with electroadhesion functionality. *Soft robotics*, 6(6):701–712, 2019.
- [32] Rui Chen, Zhuo Zhang, Jianglong Guo, Fuyou Liu, Jinsong Leng, and Jonathan Rossiter. Variable stiffness electroadhesion and compliant electroadhesive grippers. *Soft Robotics*, 9(6):1074–1082, 2022.

- [33] Inrak Choi, Nick Corson, Lizzie Peiros, Elliot W Hawkes, Sean Keller, and Sean Follmer. A soft, controllable, high force density linear brake utilizing layer jamming. *IEEE Robotics and Automation Letters*, 3(1):450–457, 2017.
- [34] Won Ho Choi, Sunghwan Kim, Dongun Lee, and Dongjun Shin. Soft, multi-dof, variable stiffness mechanism using layer jamming for wearable robots. *IEEE Robotics and Automation Letters*, 4(3):2539–2546, 2019.
- [35] Matteo Cianchetti, Cecilia Laschi, Arianna Menciassi, and Paolo Dario. Biomedical applications of soft robotics. *Nature Reviews Materials*, 3(6):143–153, 2018.
- [36] Matteo Cianchetti, Tommaso Ranzani, Giada Gerboni, Thrishantha Nanayakkara, Kaspar Althoefer, Prokar Dasgupta, and Arianna Menciassi. Soft robotics technologies to address shortcomings in today’s minimally invasive surgery: the stiff-flop approach. *Soft robotics*, 1(2):122–131, 2014.
- [37] Juan De Vicente, Daniel J Klingenberg, and Roque Hidalgo-Alvarez. Magnetorheological fluids: a review. *Soft matter*, 7(8):3701–3710, 2011.
- [38] Mohammadreza Lalegani Dezaki and Mahdi Bodaghi. Shape memory meta-laminar jamming actuators by 4d printing. *Soft Matter*, 2023.
- [39] Krishna Manaswi Digumarti, Vito Cacucciolo, and Herbert Shea. Dexterous textile manipulation using electroadhesive fingers. In *2021 IEEE/RSJ International Conference on Intelligent Robots and Systems (IROS)*, pages 6104–6109. IEEE, 2021.
- [40] Jacques Dumaïs and Yoël Forterre. “vegetable dynamicks”: the role of water in plant movements. *Annual Review of Fluid Mechanics*, 44:453–478, 2012.
- [41] Bin Fang, Fuchun Sun, Linyuan Wu, Fukang Liu, Xiangxiang Wang, Haiming Huang, Wenbing Huang, Huaping Liu, and Li Wen. Multimode grasping soft gripper achieved by layer jamming structure and tendon-driven mechanism. *Soft Robotics*, 9(2):233–249, 2022.
- [42] Seth G Fitzgerald, Gary W Delaney, and David Howard. A review of jamming actuation in soft robotics. In *Actuators*, volume 9, page 104. MDPI, 2020.
- [43] Peter Fratzl and Friedrich G Barth. Biomaterial systems for mechanosensing and actuation. *Nature*, 462(7272):442–448, 2009.
- [44] Peter Fratzl, Rivka Elbaum, and Ingo Burgert. Cellulose fibrils direct plant organ movements. *Faraday discussions*, 139:275–282, 2008.

- [45] Peter Fratzl and Richard Weinkamer. Nature’s hierarchical materials. *Progress in materials Science*, 52(8):1263–1334, 2007.
- [46] Lucas Gerez, Geng Gao, Anany Dwivedi, and Minas Liarokapis. A hybrid, wearable exoskeleton glove equipped with variable stiffness joints, abduction capabilities, and a telescopic thumb. *Ieee Access*, 8:173345–173358, 2020.
- [47] Lucas Gerez, Geng Gao, and Minas Liarokapis. Laminar jamming flexure joints for the development of variable stiffness robot grippers and hands. In *2020 IEEE/RSJ International Conference on Intelligent Robots and Systems (IROS)*, pages 8709–8715. IEEE, 2020.
- [48] Guoying Gu, Jiang Zou, Ruike Zhao, Xuanhe Zhao, and Xiangyang Zhu. Soft wall-climbing robots. *Science Robotics*, 3(25):eaat2874, 2018.
- [49] Jianglong Guo, Khaled Elgeneidy, Chaoqun Xiang, Niels Lohse, Laura Justham, and Jonathan Rossiter. Soft pneumatic grippers embedded with stretchable electroadhesion. *Smart Materials and Structures*, 27(5):055006, 2018.
- [50] Mehdi Hajianmaleki and Mohamad S Qatu. Vibrations of straight and curved composite beams: A review. *Composite Structures*, 100:218–232, 2013.
- [51] Ehsan Hajiesmaili and David R Clarke. Dielectric elastomer actuators. *Journal of Applied Physics*, 129(15), 2021.
- [52] Simon Hauser, Matthew Robertson, Auke Ijspeert, and Jamie Paik. Jammjoint: A variable stiffness device based on granular jamming for wearable joint support. *IEEE Robotics and Automation Letters*, 2(2):849–855, 2017.
- [53] Elliot W Hawkes, Carmel Majidi, and Michael T Tolley. Hard questions for soft robotics. *Science robotics*, 6(53):eabg6049, 2021.
- [54] Ronan Hinchet and Herbert Shea. High force density textile electrostatic clutch. *Advanced Materials Technologies*, 5(4):1900895, 2020.
- [55] Ronan J Hinchet and Herbert Shea. Glove-and sleeve-format variable-friction electrostatic clutches for kinesthetic haptics. *Advanced Intelligent Systems*, 4(12):2200174, 2022.
- [56] Wenqi Hu, Guo Zhan Lum, Massimo Mastrangeli, and Metin Sitti. Small-scale soft-bodied robot with multimodal locomotion. *Nature*, 554(7690):81–85, 2018.
- [57] Geonwoo Hwang, Jihwan Park, David Santiago Diaz Cortes, Kyujin Hyeon, and Ki-Uk Kyung. Electroadhesion-based high-payload soft gripper with mechanically strengthened structure. *IEEE Transactions on Industrial Electronics*, 69(1):642–651, 2021.

- [58] Michele Ibrahimi, Linda Paternò, Leonardo Ricotti, and Arianna Menciassi. A layer jamming actuator for tunable stiffness and shape-changing devices. *Soft Robotics*, 8(1):85–96, 2021.
- [59] Saurabh Jadhav, Mohamad Ramzi Abdul Majit, Benjamin Shih, Jürgen P Schulze, and Michael T Tolley. Variable stiffness devices using fiber jamming for application in soft robotics and wearable haptics. *Soft Robotics*, 9(1):173–186, 2022.
- [60] Heinrich M Jaeger. Celebrating soft matter’s 10th anniversary: Toward jamming by design. *Soft matter*, 11(1):12–27, 2015.
- [61] A JOHANSSON. Paper friction-influence of measurement conditions. *Tappi J.*, 81:175, 1998.
- [62] Alfred Johnsen and Knud Rahbek. A physical phenomenon and its applications to telegraphy, telephony, etc. *Journal of the Institution of Electrical Engineers*, 61(320):713–725, 1923.
- [63] Ryo Kanno, Fabio Caruso, Kazuma Takai, Yegor Piskarev, Vito Cacucciolo, and Jun Shintake. Biodegradable electrohydraulic soft actuators. *Advanced Intelligent Systems*, 5(9):2200239, 2023.
- [64] Nicholas Kellaris, Vidyacharan Gopaluni Venkata, Philipp Rothmund, and Christoph Keplinger. An analytical model for the design of peano-hassel actuators with drastically improved performance. *Extreme Mechanics Letters*, 29:100449, 2019.
- [65] William M Kier and Kathleen K Smith. Tongues, tentacles and trunks: the biomechanics of movement in muscular-hydrostats. *Zoological journal of the Linnean Society*, 83(4):307–324, 1985.
- [66] Ozgun Kilic Afsar, Ali Shtarbanov, Hila Mor, Ken Nakagaki, Jack Forman, Karen Modrei, Seung Hee Jeong, Klas Hjort, Kristina Höök, and Hiroshi Ishii. Omnifiber: Integrated fluidic fiber actuators for weaving movement based interactions into the ‘fabric of everyday life’. In *The 34th Annual ACM Symposium on User Interface Software and Technology*, pages 1010–1026, 2021.
- [67] Yong-Jae Kim, Shanbao Cheng, Sangbae Kim, and Karl Iagnemma. Design of a tubular snake-like manipulator with stiffening capability by layer jamming. In *2012 IEEE/RSJ international conference on intelligent robots and systems*, pages 4251–4256. IEEE, 2012.
- [68] Yong-Jae Kim, Shanbao Cheng, Sangbae Kim, and Karl Iagnemma. A novel layer jamming mechanism with tunable stiffness capability for minimally invasive surgery. *IEEE Transactions on Robotics*, 29(4):1031–1042, 2013.

- [69] Guggi Kofod, Peter Sommer-Larsen, Roy Kornbluh, and Ron Pelrine. Actuation response of polyacrylate dielectric elastomers. *Journal of intelligent material systems and structures*, 14(12):787–793, 2003.
- [70] Anastasia Koivikko, Dirk-Michael Drotlef, Metin Sitti, and Veikko Sariola. Magnetically switchable soft suction grippers. *Extreme Mechanics Letters*, 44:101263, 2021.
- [71] Junghan Kwon, Inrak Choi, Myungsun Park, Jeongin Moon, Bomin Jeong, Prabhat Pathak, Jooeun Ahn, and Yong-Lae Park. Selectively stiffening garments enabled by cellular composites. *Advanced Materials Technologies*, page 2101543, 2022.
- [72] Cecilia Laschi, Barbara Mazzolai, and Matteo Cianchetti. Soft robotics: Technologies and systems pushing the boundaries of robot abilities. *Science robotics*, 1(1):eaah3690, 2016.
- [73] Chiwon Lee, Myungjoon Kim, Yoon Jae Kim, Nhayoung Hong, Seungwan Ryu, H Jin Kim, and Sungwan Kim. Soft robot review. *International Journal of Control, Automation and Systems*, 15:3–15, 2017.
- [74] Edouard Leroy, Ronan Hinchet, and Herbert Shea. Multimode hydraulically amplified electrostatic actuators for wearable haptics. *Advanced Materials*, 32(36):2002564, 2020.
- [75] David J Levine, Gokulanand M Iyer, R Daelan Roosa, Kevin T Turner, and James H Pikul. A mechanics-based approach to realize high-force capacity electroadhesives for robots. *Science Robotics*, 7(72):eabo2179, 2022.
- [76] Liuchi Li, Eloïse Marteau, and José E Andrade. Capturing the inter-particle force distribution in granular material using ls-dem. *Granular Matter*, 21:1–16, 2019.
- [77] Yangqiao Lin, Geng Yang, Yuwen Liang, Chao Zhang, Wei Wang, Dahong Qian, Huayong Yang, and Jun Zou. Controllable stiffness origami “skeletons” for lightweight and multifunctional artificial muscles. *Advanced Functional Materials*, 30(31):2000349, 2020.
- [78] Carmel Majidi. Soft-matter engineering for soft robotics. *Advanced Materials Technologies*, 4(2):1800477, 2019.
- [79] Mariangela Manti, Vito Cacucciolo, and Matteo Cianchetti. Stiffening in soft robotics: A review of the state of the art. *IEEE Robotics & Automation Magazine*, 23(3):93–106, 2016.



- [80] Massimiliano Mastrangelo and Vito Cacucciolo. High-force soft grippers with electroadhesion on curved objects. In *2022 IEEE 5th International Conference on Soft Robotics (RoboSoft)*, pages 384–389. IEEE, 2022.
- [81] Massimiliano Mastrangelo, Fabio Caruso, Giuseppe Carbone, and Vito Cacucciolo. Electroadhesion zipping with soft grippers on curved objects. *Extreme Mechanics Letters*, 61:101999, 2023.
- [82] Gareth J Monkman, Paul M Taylor, and GJ Farnworth. Principles of electroadhesion in clothing robotics. *International Journal of Clothing Science and Technology*, 1(3):14–20, 1989.
- [83] Giacomo Moretti, Mattia Duranti, Michele Righi, Rocco Vertechy, and Marco Fontana. Analysis of dielectric fluid transducers. In *Electroactive Polymer Actuators and Devices (EAPAD) XX*, volume 10594, pages 142–154. SPIE, 2018.
- [84] Yashraj S Narang, Buse Aktaş, Sarah Ornellas, Joost J Vlassak, and Robert D Howe. Lightweight highly tunable jamming-based composites. *Soft robotics*, 7(6):724–735, 2020.
- [85] Yashraj S Narang, Alperen Degirmenci, Joost J Vlassak, and Robert D Howe. Transforming the dynamic response of robotic structures and systems through laminar jamming. *IEEE Robotics and Automation Letters*, 3(2):688–695, 2017.
- [86] Yashraj S Narang, Joost J Vlassak, and Robert D Howe. Mechanically versatile soft machines through laminar jamming. *Advanced Functional Materials*, 28(17):1707136, 2018.
- [87] Jifei Ou, Lining Yao, Daniel Tauber, Jürgen Steimle, Ryuma Niiyama, and Hiroshi Ishii. jamsheets: thin interfaces with tunable stiffness enabled by layer jamming. In *Proceedings of the 8th International Conference on Tangible, Embedded and Embodied Interaction*, pages 65–72, 2014.
- [88] Sungjune Park, Kunal Mondal, Robert M Treadway III, Vikash Kumar, Siyuan Ma, James D Holbery, and Michael D Dickey. Silicones for stretchable and durable soft devices: Beyond sylgard-184. *ACS applied materials & interfaces*, 10(13):11261–11268, 2018.
- [89] Bo NJ Persson. General theory of electroadhesion. *Journal of Physics: Condensed Matter*, 33(43):435001, 2021.
- [90] Joshua Pinskiar, James Brett, Lauren Hanson, Katrina Lo Surdo, and David Howard. Jammkle: Fibre jamming 3d printed multi-material tendons and their application in a robotic ankle. In *2022 IEEE/RSJ International Conference on Intelligent Robots and Systems (IROS)*, pages 8507–8514. IEEE, 2022.

- [91] Panagiotis Polygerinos, Nikolaus Correll, Stephen A Morin, Bobak Mosadegh, Cagdas D Onal, Kirstin Petersen, Matteo Cianchetti, Michael T Tolley, and Robert F Shepherd. Soft robotics: Review of fluid-driven intrinsically soft devices; manufacturing, sensing, control, and applications in human-robot interaction. *Advanced Engineering Materials*, 19(12):1700016, 2017.
- [92] Panagiotis Polygerinos, Zheng Wang, Kevin C Galloway, Robert J Wood, and Conor J Walsh. Soft robotic glove for combined assistance and at-home rehabilitation. *Robotics and Autonomous Systems*, 73:135–143, 2015.
- [93] Gill A Pratt and Matthew M Williamson. Series elastic actuators. In *Proceedings 1995 IEEE/RSJ International Conference on Intelligent Robots and Systems. Human Robot Interaction and Cooperative Robots*, volume 1, pages 399–406. IEEE, 1995.
- [94] Vivek Ramachandran, Jun Shintake, and Dario Floreano. All-fabric wearable electroadhesive clutch. *Advanced Materials Technologies*, 4(2):1800313, 2019.
- [95] Steven I Rich, Robert J Wood, and Carmel Majidi. Untethered soft robotics. *Nature Electronics*, 1(2):102–112, 2018.
- [96] Philipp Rothemund, Nicholas Kellaris, Shane K Mitchell, Eric Acome, and Christoph Keplinger. Hasel artificial muscles for a new generation of life-like robots—recent progress and future opportunities. *Advanced materials*, 33(19):2003375, 2021.
- [97] Mark Runciman, Ara Darzi, and George P Mylonas. Soft robotics in minimally invasive surgery. *Soft robotics*, 6(4):423–443, 2019.
- [98] Daniela Rus and Michael T Tolley. Design, fabrication and control of soft robots. *Nature*, 521(7553):467–475, 2015.
- [99] Rosalin Sahoo and BN Singh. A new shear deformation theory for the static analysis of laminated composite and sandwich plates. *International Journal of Mechanical Sciences*, 75:324–336, 2013.
- [100] Steeven Villa Salazar, Claudio Pacchierotti, Xavier de Tinguay, Anderson Maciel, and Maud Marchal. Altering the stiffness, friction, and shape perception of tangible objects in virtual reality using wearable haptics. *IEEE transactions on haptics*, 13(1):167–174, 2020.
- [101] Atteshamuddin S Sayyad and Yuwaraj M Ghugal. Bending, buckling and free vibration of laminated composite and sandwich beams: A critical review of literature. *Composite Structures*, 171:486–504, 2017.

- [102] Ethan W Schaler, Donald Ruffatto, Paul Glick, Victor White, and Aaron Parness. An electrostatic gripper for flexible objects. In *2017 IEEE/RSJ International Conference on Intelligent Robots and Systems (IROS)*, pages 1172–1179. IEEE, 2017.
- [103] Dylan S Shah, Ellen J Yang, Michelle C Yuen, Evelyn C Huang, and Rebecca Kramer-Bottiglio. Jamming skins that control system rigidity from the surface. *Advanced Functional Materials*, 31(1):2006915, 2021.
- [104] Jun Shintake, Vito Cacucciolo, Dario Floreano, and Herbert Shea. Soft robotic grippers. *Advanced materials*, 30(29):1707035, 2018.
- [105] Jun Shintake, Samuel Rosset, Bryan Edward Schubert, Dario Floreano, and Herbert Shea. Versatile soft grippers with intrinsic electroadhesion based on multifunctional polymer actuators. *Advanced materials*, 28(2):231–238, 2016.
- [106] Jun Shintake, Bryan Schubert, Samuel Rosset, Herbert Shea, and Dario Floreano. Variable stiffness actuator for soft robotics using dielectric elastomer and low-melting-point alloy. In *2015 IEEE/RSJ International Conference on Intelligent Robots and Systems (IROS)*, pages 1097–1102. IEEE, 2015.
- [107] Sami Simula, Timo Varpula, Satu Ikäläinen, Heikki Seppä, Aleksandr Pauku, and Kaarlo Niskanen. Measurement of the dielectric properties of paper. In *NIP & Digital Fabrication Conference*, volume 14, pages 157–160. Society of Imaging Science and Technology, 1998.
- [108] Ion-Dan Sîrbu, Marco Bolignari, Salvatore D’Avella, Francesco Damiani, Lorenzo Agostini, Paolo Tripicchio, Rocco Vertechy, Lucio Pancheri, and Marco Fontana. Adhesion state estimation for electrostatic gripper based on online capacitance measure. In *Actuators*, volume 11, page 283. MDPI, 2022.
- [109] Ion-Dan Sîrbu, David Preninger, Doris Danninger, Lukas Penkner, Reinhard Schwödiauer, Giacomo Moretti, Nikita Arnold, Marco Fontana, and Martin Kaltenbrunner. Electrostatic actuators with constant force at low power loss using matched dielectrics. *Nature Electronics*, 6(11):888–899, 2023.
- [110] Michael Smith, Vito Cacucciolo, and Herbert Shea. Fiber pumps for wearable fluidic systems. *Science*, 379(6639):1327–1332, 2023.
- [111] Andrew A Stanley, James C Gwilliam, and Allison M Okamura. Haptic jamming: A deformable geometry, variable stiffness tactile display using pneumatics and particle jamming. In *2013 World Haptics Conference (WHC)*, pages 25–30. IEEE, 2013.

- [112] Erik Steltz, Annan Mozeika, Nick Rodenberg, Eric Brown, and Heinrich M Jaeger. Jsel: Jamming skin enabled locomotion. In *2009 IEEE/RSJ International Conference on Intelligent Robots and Systems*, pages 5672–5677. IEEE, 2009.
- [113] German Sumbre, Yoram Gutfreund, Graziano Fiorito, Tamar Flash, and Binyamin Hochner. Control of octopus arm extension by a peripheral motor program. *Science*, 293(5536):1845–1848, 2001.
- [114] Zhigang Suo. Theory of dielectric elastomers. *Acta Mechanica Solida Sinica*, 23(6):549–578, 2010.
- [115] Majid Taghavi, Tim Helps, and Jonathan Rossiter. Electro-ribbon actuators and electro-origami robots. *Science Robotics*, 3(25):eaau9795, 2018.
- [116] Alice Tonazzini, Stefano Mintchev, Bryan Schubert, Barbara Mazzolai, Jun Shintake, and Dario Floreano. Variable stiffness fiber with self-healing capability. *Advanced Materials*, 28(46):10142–10148, 2016.
- [117] Nikolaos G Tsagarakis, Matteo Laffranchi, Bram Vanderborght, and Darwin G Caldwell. A compact soft actuator unit for small scale human friendly robots. In *2009 IEEE international conference on robotics and automation*, pages 4356–4362. IEEE, 2009.
- [118] Bram Vanderborght, Alin Albu-Schäffer, Antonio Bicchi, Etienne Burdet, Darwin G Caldwell, Raffaella Carloni, Manuel Catalano, Oliver Eiberger, Werner Friedl, Ganesh Ganesh, et al. Variable impedance actuators: A review. *Robotics and autonomous systems*, 61(12):1601–1614, 2013.
- [119] Nikolaos Vasios, Yashraj Narang, Buse Aktaş, Robert Howe, and Katia Bertoldi. Numerical analysis of periodic laminar and fibrous media undergoing a jamming transition. *European Journal of Mechanics-A/Solids*, 75:322–329, 2019.
- [120] Nicola Vitiello, Tommaso Lenzi, Stefano Roccella, Stefano Marco Maria De Rossi, Emanuele Cattin, Francesco Giovacchini, Fabrizio Vecchi, and Maria Chiara Carrozza. Neuroexos: A powered elbow exoskeleton for physical rehabilitation. *IEEE transactions on robotics*, 29(1):220–235, 2012.
- [121] AT Wanasinghe, WVI Awantha, AGP Kavindya, AL Kulasekera, DS Chathuranga, and B Senanayake. A layer jamming soft glove for hand tremor suppression. *IEEE Transactions on Neural Systems and Rehabilitation Engineering*, 29:2684–2694, 2021.

- [122] Hongbo Wang, Massimo Totaro, and Lucia Beccai. Toward perceptive soft robots: Progress and challenges. *Advanced Science*, 5(9):1800541, 2018.
- [123] Liyu Wang, Yang Yang, Yonghua Chen, Carmel Majidi, Fumiya Iida, Erin Askounis, and Qibing Pei. Controllable and reversible tuning of material rigidity for robot applications. *Materials Today*, 21(5):563–576, 2018.
- [124] Tao Wang, Jinhua Zhang, Yue Li, Jun Hong, and Michael Yu Wang. Electrostatic layer jamming variable stiffness for soft robotics. *IEEE/ASME Transactions on Mechatronics*, 24(2):424–433, 2019.
- [125] Wei Wang and Sung-Hoon Ahn. Shape memory alloy-based soft gripper with variable stiffness for compliant and effective grasping. *Soft robotics*, 4(4):379–389, 2017.
- [126] Xiangxiang Wang, Linyuan Wu, Bin Fang, Xiangrong Xu, Haiming Huang, and Fuchun Sun. Layer jamming-based soft robotic hand with variable stiffness for compliant and effective grasping. *Cognitive Computation and Systems*, 2(2):44–49, 2020.
- [127] Yifan Wang, Liuchi Li, Douglas Hofmann, José E Andrade, and Chiara Daraio. Structured fabrics with tunable mechanical properties. *Nature*, 596(7871):238–243, 2021.
- [128] Ying Wei, Yonghua Chen, Tao Ren, Qiao Chen, Changxin Yan, Yang Yang, and Yingtian Li. A novel, variable stiffness robotic gripper based on integrated soft actuating and particle jamming. *Soft Robotics*, 3(3):134–143, 2016.
- [129] George M Whitesides. Soft robotics. *Angewandte Chemie International Edition*, 57(16):4258–4273, 2018.
- [130] Bilige Yang, Robert Baines, Dylan Shah, Sreekalyan Patiballa, Eugene Thomas, Madhusudhan Venkadesan, and Rebecca Kramer-Bottiglio. Reprogrammable soft actuation and shape-shifting via tensile jamming. *Science Advances*, 7(40):eabh2073, 2021.
- [131] Yang Yang, Yingtian Li, and Yonghua Chen. Principles and methods for stiffness modulation in soft robot design and development. *Bio-Design and Manufacturing*, 1(1):14–25, 2018.
- [132] Yang Yang, Yazhan Zhang, Zicheng Kan, Jieli Zeng, and Michael Yu Wang. Hybrid jamming for bioinspired soft robotic fingers. *Soft robotics*, 7(3):292–308, 2020.

- [133] Jessica Yin, Ronan Hinchet, Herbert Shea, and Carmel Majidi. Wearable soft technologies for haptic sensing and feedback. *Advanced Functional Materials*, 31(39):2007428, 2021.
- [134] Hiroshi Yoshihara and Masahiro Yoshinobu. Effects of specimen configuration and measurement method of strain on the characterization of tensile properties of paper. *Journal of wood science*, 60(4):287–293, 2014.
- [135] Guoliang Zhong, Yangdong Hou, and Weiqiang Dou. A soft pneumatic dexterous gripper with convertible grasping modes. *International Journal of Mechanical Sciences*, 153:445–456, 2019.